The Life and Death of Heterogeneity in Magmas: Implications for Failure Forecasting

Jérémie Vasseur

SIGILL·UNIVERSITAT·LUDOVIC·MAXIM·

München 2015

The Life and Death of Heterogeneity in Magmas: Implications for Failure Forecasting

Jérémie Vasseur

Dissertation
an der Fakultät für Geowissenschaften
der Ludwig–Maximilians–Universität
München

vorgelegt von
Jérémie Vasseur
aus Lagny-sur-Marne (Frankreich)

München, den 3. März 2015

Erstgutachter: Prof. Dr. Donald B. Dingwell
Zweitgutachter: Prof. Dr. Yan Lavallée
Tag der mündlichen Prüfung: 23. September 2015

À mes parents, pour m'avoir toujours poussé.
À ma femme, mon fils et ma fille, pour m'avoir gardé hydraté.

« Tu vois loin comme quand on ne sait rien et que l'on sent tout
Et dans la petite cuillère faire glisser l'ordinaire que l'on catapulte au loin
Tu vois loin »
– Eiffel

SUMMARY

Explosive volcanism is one of the most catastrophic material failure phenomena. During magma ascent, fragmentation produces particulate magma, which, if deposited above the glass transition of the interstitial melt, will sinter viscously. In-conduit tuffisites, conduit wall breccias and ash deposited from exceptionally hot pyroclastic flows are scenarios in which sintering by viscous flow is possible. Therefore, understanding the kinetics of sintering and the characteristic timescales over which magma densifies are critical to understanding the degassing timeframe in conduits and deposits. Viscous sintering is accompanied by a recovery of material strength towards that of a pore-free, dense magma. Understanding damage mechanisms and seismic behaviour prior to failure of sintered volcanic products are also crucial for the application of micromechanical models and material failure forecasting laws. Powdered standard glass and industrial glass beads have been used to explore sintering mechanisms at ambient pressure conditions and temporal evolution of connected and isolated pore-structure. I observe that sintering under low axial stress is essentially particle size, surface tension and melt viscosity controlled. I found that the timescales over which the bulk density approaches that of a pore-free melt at a given temperature is dependent on the particle-contact surface area, which can be estimated from the particle shape, the packing type and the initial total porosity. Granulometric constraint on the starting material indicates that the fraction of finer particles controls the rate of sintering as they cluster in pore spaces between larger particles and have a higher driving force for sintering due to their higher surface energy to volume ratio. Consequently, the resultant sample suite has a range of microstructures because the viscous sintering process promotes a fining of pores and a coarsening of particles. In a volcano, newly formed sintering material will then further contribute to magma-plugging of the conduit and its mechanical properties will affect magma rupture and its associated precursory signals. This consideration permitted me to explore the effect of sintering on the stress required for dynamic macroscopic failure of synthesised samples and assess the ability of precursory microseismic signals to be used as a failure forecast proxy at conditions relevant to shallow volcanic conduits. To this end, the samples were subjected to mechanical tests under a constant rate of deformation and at a temperature in the region of the material glass transition. A dual acoustic emission rig was employed to track the occurrence of brittle fracturing. The monitored acoustic dataset was then exploited to systematically assess the accuracy of the failure forecasting method as a function of heterogeneity (cast as porosity) since it acts as nucleating site for fracture propagation. The pore-emanating crack model describes well the peak stress at failure in the elastic regime for these materials. I show that the failure forecast method predicts failure within 0–15% error at porosities >0.2. However, when porosities are <0.2, the forecast error associated with predicting the failure time increases to >100%. I interpret these results as a function of the low efficiency with which strain energy can be released in the scenario where there are few or no heterogeneities from which cracks can propagate. These observations shed light on questions surrounding the variable efficacy of the failure forecast method applied to active volcanoes. In particular, they provide a systematic demonstration of the fact that a good understanding of material properties is required. Thus I wish to emphasise the need for a better coupling of empirical failure forecasting models with mechanical parameters, such as failure criteria for heterogeneous materials, and point to the implications of this for a broad range of material-based disciplines.

ZUSAMMENFASSUNG

Explosiver Vulkanismus ist eines der drastischsten Phänomene, die ursächlich durch Materialversagen ausgelöst werden. Während seines Aufstiegs in der Kruste fragmentiert Magma zu partikelgrossen Magmafetzen, die, sofern überhalb des Glassübergangs abgelagert, viskos sintern können. Sintern durch viskosen Fluss wird bei Ablagerung von Intra-Schlot Tuffisiten, Schlotwand Brekzien und Asche aus extrem heissen pyroklastischen Ströme erwartet. Die Eingrenzung der Kinetik des Sinterns, sowie der charakteristischen Zeitskalen der Verdichtung von Magma, sind daher essentiell um den Zeitrahmen des Entgasens von Schloten und Ablagerungen besser zu verstehen. Viskoses Sintern wird begleitet von einer Erhöhung der Material Festigkeit zu der eines poren-freien, dichten Magmas. Weiterhin ist es wichtig, Beschädigungsmechanismen und das seismische Verhalten der vulkanischen Produkte kurz vor dem Materialversagen zu verstehen, um die Anwendung von mikromechanischen Modellen und die Vorhersage von Materialversagen zu ermöglichen. Glasstandard in pulverisierter Form und industrielle Glaskugeln wurden herangezogen um Sintermechanismen bei Atmosphärendruck und die zeitliche Entwicklung verbundener und isolierter Porenstrukturen zu erforschen. Ich beobachtete, dass Sintern bei niedriger axialer Belastung hauptsächlich durch Partikelgrösse, Oberflächenspannung und Schmelzviskosität kontrolliert wird. Weiterhin ist die Zeitskala, über die die Gesamtdichte bei einer definierten Temperatur die einer porenfreien Schmelze erreicht, abhängig von der Partikel-Kontakt Oberfläche, die über Partikelform, die Partikelpackung und die initiale Gesamtporosität abgeschätzt werden kann. Korngrössenanalysen der Anfangsmaterialien deuten an, dass die Feinfraktion die Rate des Sinterns kontrolliert, da der Feinanteil in den Zwickeln der grösseren Partikel Anhäufungen bilden kann und ausserdem ein höheres Sinterpotential durch sein grösseres Oberflächen-Volumen Verhältnis aufweist. Dementsprechend weisen die hergestellten Proben eine Reihe von Mikrostrukturen auf, die durch Porenverkleinerung und Kornvergröberung während des viskosen Sinterns hervorgerufen wurden. Dadurch wird neu-gebildetes, sinterndes Material innerhalb eines Vulkans das Verstopfen des Schlotes fördern, und die mechanischen Eigenschaften dieses Materials beeinflussen die Fragmentation des eigentlichen Magmas und der assoziierten Vorwarnsignale. Aufgrund dieser Betrachtung betrachte ich den Effekt des Sinterns auf die für dynamisches makroskopisches Versagen unserer synthetisierten Proben nötige Belastung näher. Dies geschah, um das Potential der mikroseismischen Signale bei Bedingungen innerhalb eines Vulkanschlots als Vorhersagekriterium für Materialversagen abzuschätzen. Dazu wurden die Proben bei konstanter Deformationsrate und Temperaturen in der Nähe des Glasübergangs mechanischen Tests unterzogen. Das Auftreten von Sprödbruchverhalten wurde mithilfe eines dualen Schallemissionsgerätes aufgezeichnet. Der resultierende akustische Datensatz wurde dann herangezogen, um die Genauigkeit der Vorhersagemethode für das Versagen als Funktion der Probenheterogeneität (also Porosität) einzugrenzen, da Porosität innerhalb eines Materials die Entstehung von Bruchstellen fördert. In diesem Zusammenhang beschreibt das Modell der „Pore-emanating cracks" für diese Materialien die Maximalbelastung bei Versagen im elastischen Regime. Ich zeige, dass Versagen bei Porositäten >0,2 innerhalb eines Fehler von 0–15% vorhergesagt werden kann. Sobald die Porositäten unter einen Wert von 0,2 fallen steigt der Fehler, der mit der Vorhersage der Versagenszeit assoziiert ist, auf über 100% an. Dieses Ergebnis interpretiere ich als eine Funktion der niedrigen Effizienz, mit der Verformungsenergie freigesetzt werden kann, wenn wenige oder keine Heterogeneitäten (Porosität) als Schwachstellen im Material vorhanden sind. Dies könnte zu der Frage beitragen, warum Versagensvorhersage an aktiven Vulkanen bisher zu unterschiedlich guten Ergebnissen geführt hat. Insbesondere zeigen meine Beobachtungen systematisch, dass ein tiefes Verständnis der Materialeigenschaften unerlässlich ist. Ich möchte daher betonen, dass die empirischen Vorhersagemodelle besser mit mechanischen Parametern, wie Versagenskriterien für heterogene Materialien, gekoppelt werden sollten, mit Auswirkungen für einen grossen Bereich der material-wissenschaftlichen Disziplinen.

Résumé

Le volcanisme explosif est l'un des phénomènes de fracturation matérielle les plus catastrophiques qui soient. Durant son ascension dans le conduit volcanique, le magma se fragmente en particules qui, une fois déposées à une température excédant celle de la transition vitreuse du liquide interstitiel, vont se souder de façon visqueuse. Les tuffisites formées dans le conduit ainsi que les cataclasites formées le long de ses parois, mais aussi les cendres déposées à partir de coulées pyroclastiques exceptionnellement chaudes, sont autant d'exemples pour lesquels du frittage par écoulement visqueux est possible. Comprendre la cinétique du frittage ainsi que les échelles de temps caractéristiques liées à la densification du magma est par conséquent crucial, afin de pouvoir identifier les périodes de dégazage dans les conduits et les dépôts volcaniques. Le frittage visqueux est accompagné d'un recouvrement de la résistance mécanique du matériel vers celle d'un magma dense et exempt de pores. Il est également crucial de comprendre les mécanismes liés au dommage ainsi que le comportement sismique avant la rupture des produits volcaniques frittés pour l'application de modèles micromécaniques et de lois de prédiction de la cassure matérielle. Un verre standard réduit en poudre et des billes de verre industrielles ont été utilisé, afin d'étudier les mécanismes de frittage à pression ambiante ainsi que l'évolution temporelle de la structure des pores connectés et isolés. J'observe que le frittage, sous faible contrainte axiale, est essentiellement contrôlé par la taille des particules, la tension de surface et la viscosité du verre. Je constate que, à une température donnée, les échelles de temps, pour lesquelles la densité du magma se rapproche de celle du verre pur, dépendent de la surface de contact entre les particules, qui peut être estimée à partir de la forme des particules, du type d'empilement et de la porosité initiale. Les contraintes granulométriques sur le matériel de départ indiquent que c'est la fraction des fines particules qui contrôle le taux de frittage : ces particules se regroupent dans les espaces créés entre les plus grandes particules et ont une force d'entraînement par frittage plus élevée en raison du rapport entre l'énergie de surface et le volume plus important. En conséquence, la série d'échantillons obtenus par frittage visqueux possède une gamme de microstructures, puisque ce processus favorise la réduction du volume des pores par l'amalgamation des particules. Au sein d'un volcan, la présence de magma nouvellement fritté pourra alors contribuer davantage au colmatage du conduit et ses propriétés mécaniques auront une incidence sur la fragmentation magmatique ainsi que sur les signaux précurseurs associés. Cette considération m'a permis, d'une part, d'étudier l'effet du frittage sur la contrainte mécanique nécessaire pour engendrer la rupture macroscopique des échantillons synthétisés et, d'autre part, à évaluer la capacité des signaux microsismiques précurseurs à être utilisés pour prédire la cassure, à des conditions de pression et de température pertinentes pour les conduits volcaniques peu profonds. À cette fin, les échantillons ont été soumis à des essais mécaniques pour lesquels une vitesse constante de déformation ainsi qu'une température correspondant à la zone de transition vitreuse du matériel ont été appliqué. Deux capteurs d'émission acoustique ont été utilisé pour surveiller la fracturation matérielle. Les données acoustiques ont ensuite été exploité, afin d'évaluer de façon systématique la précision de la méthode de prédiction de la cassure en fonction de l'hétérogénéité (la porosité est utilisée comme quantification du degré d'hétérogénéité matérielle), car elle correspond à la zone de nucléation des fractures. Dans le régime élastique, le modèle de fissuration depuis les pores décrit correctement le pic de stress mécanique au moment de la rupture. Je montre que la méthode de prédiction de la cassure indique une erreur absolue comprise entre 0 et 15 % pour les porosités supérieures à 0,2. Cependant, lorsque les porosités sont inférieures à 0,2, l'erreur augmente jusque plus de 100 %. J'interpréte ces résultats en termes de faible efficacité avec laquelle l'énergie mécanique accumulée peut être libérée dans le cas où il y a peu ou pas d'hétérogénéités à partir desquelles les fissures peuvent se propager. Ces observations mettent en lumière les questions sur l'efficacité de la méthode de prédiction de la cassure lorsqu'appliquée aux volcans actifs. Plus particulièrement, elles démontrent de façon systématique qu'une bonne compréhension des propriétés physiques et mécaniques du matériel est fondamentale. Ainsi, je tiens à souligner la nécessité d'un meilleur couplage des modèles empiriques de prédiction de la cassure avec des paramètres mécaniques, tel que des critères de rupture des matériaux hétérogènes, et pointer en direction des implications pour un large éventail de disciplines axées sur la science des matériaux.

Contents

Listing of figures

Listing of symbols

α	Constant in Equation 2.26 [$\mathrm{Pa}^{-1}\,\mathrm{m}^{-1/2}$].
$\bar{s}$	Hilbert transform of a seismic signal [V].
β	Constant in Equation 2.27 [$\mathrm{m}^{2}\,\mathrm{J}^{-1}$].
$\ddot{\omega}$	Acceleration of a geophysical signal [s^{-2}].
δ	Failure forecast error [-].
δ_{ij}	Kronecker symbol [-].
$\dot{\varepsilon}_{ii}$	First invariant of the strain rate tensor [s^{-1}].
$\dot{\varepsilon}_{ij}$	Strain rate tensor [s^{-1}].
$\dot{\varepsilon}_{ij}'$	Deviatoric strain rate tensor [s^{-1}].
$\dot{\varepsilon}_{r}$	Radial strain rate [s^{-1}].
$\dot{\varepsilon}_{z}$	Axial strain rate [s^{-1}].
$\dot{\omega}$	Rate of a geophysical signal [s^{-1}].
η	Shear viscosity [Pa s].
η_{0}	Melt shear viscosity [Pa s].
η_{r}	Relative shear viscosity [-].
Γ	Melt-vapour interfacial tension [$\mathrm{N}\,\mathrm{m}^{-1}$].
γ	Surface energy density [$\mathrm{J}\,\mathrm{m}^{-2}$].
$\varkappa$	Bulk viscosity [Pa s].
$\varkappa_{0}$	Melt bulk viscosity [Pa s].
$\varkappa_{r}$	Relative bulk viscosity [-].
λ_{d}	Densification timescale [s].
λ_{MS}	Sintering timescale after Mackenzie & Shuttleworth [1949] [s].
λ_{r}	Structural relaxation timescale [s].
λ_{s}	Sintering timescale [s].
μ	Newtonian melt shear viscosity [Pa s].
ν	Empirical constant in Equation 4.17 [-].
Ω	Cumulative number of seismic events [-].
φ	Porosity [-].
$\varphi_{C,i}$	Initial connected porosity [-].
φ_{C}	Connected porosity [-].
φ_{r}	Relative porosity [-].
$\varphi_{T,f}$	Final total porosity [-].
$\varphi_{T,i}$	Initial total porosity [-].
φ_{T}	Total porosity [-].
ϱ_{0}	Melt density [$\mathrm{kg}\,\mathrm{m}^{-3}$].
ϱ_{bulk}	Bulk density [$\mathrm{kg}\,\mathrm{m}^{-3}$].
$\varrho_{r,f}$	Final relative density [-].

$\varrho_{r,i}$	Initial relative density [-].
ϱ_r	Relative density [-].
σ	Stress [Pa].
σ_c	Critical failure stress [Pa].
σ_{ij}	Stress tensor [Pa].
σ_P	Compressive strength [Pa].
σ_r	Radial stress [Pa].
σ_z	Axial stress [Pa].
τ_d	Sintering specific time [-].
A	FFM scaling parameter [s^{m-2}].
A_{black}	Pore area in Figure 3.5 [m^2].
A_{dB}	Amplitude of a seismic signal [dB].
A_{total}	Total area in Figure 3.5 [m^2].
A_{white}	Solid matrix area in Figure 3.5 [m^2].
b_E	Empirical constant in Equation 3.17 [-].
b_M	Empirical constant in Equation 3.16 [Pa].
C	Constant in Equation 2.28 [$\mathrm{m\,s^{-1}}$].
c	Constant rate parameter [s^{-1}].
D	Damage parameter [-].
E	Young's modulus [Pa].
E_0	Melt Young's modulus [Pa].
E_a	Arrhenius activation energy [$\mathrm{J\,mol^{-1}}$].
E_s	Envelope of a seismic signal [V].
G	Strain energy release rate [$\mathrm{J\,m^{-2}}$].
G_∞	Infinite-frequency shear modulus [Pa].
G_I	Strain energy release rate under mode I loading [$\mathrm{J\,m^{-2}}$].
H	Heterogeneity or disorder index [-].
K	Stress intensity factor [$\mathrm{Pa\,m^{1/2}}$].
k_{Exp}	Exponential scaling parameter [s^{-1}].
K_{Ic}	Critical stress intensity factor under mode I loading [$\mathrm{Pa\,m^{1/2}}$].
K_I	Stress intensity factor under mode I loading [$\mathrm{Pa\,m^{1/2}}$].
K_i	Initial stress intensity factor [$\mathrm{Pa\,m^{1/2}}$].
k_{PL}	Power law scaling parameter [s^{p-1}].
L	Likelihood [-].
$l_{c,cr}$	Critical crack length [m].
$l_{c,i}$	Initial subcritical crack length [m].
l_c	Subcritical crack length [m].
M	P-wave modulus [Pa].
m	FFM rate parameter [-].
M_0	Melt P-wave modulus [Pa].
n	Subcritical crack growth index [-].
p	Power law rate parameter [-].
p_{Lo}	Local Laplace pressure [Pa].
p_{Lr}	Relative Laplace pressure [-].
p_L	Laplace pressure [Pa].
p_p	Pore pressure [Pa].
Q	Order parameter [-].
q	Exponential rate parameter [s^{-1}].
R	Universal gas constant [$\mathrm{J\,K^{-1}mol^{-1}}$].
r	Radius of a sphere [m].

$r_{b,i}$	Initial radius of a bubble [m].
$r_{p,i}$	Initial radius of a particle [m].
r_{pores}	Average pore radius in Equation 3.14 [m].
s	Seismic signal [V].
T	Temperature [K].
t	Time [s].
$t_{c,e}$	Experimental critical time [s].
$t_{c,p}$	Predicted critical time [s].
t_c	Critical time [s].
U	Total energy [J].
U_m	Mechanical energy [J].
U_s	Surface energy [J].
$v_{c,i}$	Initial subcritical crack growth velocity [m s^{-1}].
v_c	Subcritical crack growth velocity [m s^{-1}].
V_{matrix}	Solid matrix volume [m^3].
V_{pores}	Pore volume [m^3].
v_P	P-wave velocity [m s^{-1}].
V_{total}	Total volume [m^3].

Acknowledgments

This work has come to an end and it's now my pleasure to heartily thank all those who embarked on this journey with me. The pathway was not always straight, nor was the course of my thoughts and ideas, but you were all of a great support and help. I wish to first acknowledge the Deutsche Forschungsgemeinschaft for funding such a nice research project, as well as my supervisors, Donald B. Dingwell and Yan Lavallée.

Don, you gave me a fantastic opportunity to drown in the heart of what is nowadays considered and accepted as being experimental volcanology by leaving the keys to one of the best facilities worldwide. I really enjoyed the time spent in the labs measuring stuff, running furnaces, and squashing and shattering glasses; a lot of self-satisfaction came out of it and a lot of fun too! Many many thanks for that! I also would like to thank you for the trust and confidence you put on me and on my abilities to carry out this work independently and resourcefully. As students, thank you for supporting any idea we may have, even the craziest ones, for giving us the chance to attend almost any scientific meeting whatsoever and for teaching us with great humility and respect.

Banana Yan, you were my first encounter and you successfully dragged me here. You most certainly laid down the road of a wonderful study (I mean it!) and made sure to keeping me on the track. I know that the initial focus of the study was Colima volcano, Mexico, but at the end the results are there and are, in fact, possibly applicable to any volcano. That's a much better story, isn't it? Thank you so much for everything, for your never-ending enthusiasm, for your craziness; yet never without the seriousness it requires! S'il te plait ne change rien, reste fidèle à toi-même et ne perds surtout pas ton joual ! Quand est-ce qu'on s'en va-t-on s'crisser une poutine par chez toi ?

Fabi Baby Wadsworth, what a brain! Mate, thanks for sharing so much of your brain cells, for always being on my back, for your indefectible support and energy, for your patience with my ups and downs, for the countless hard nights of work, for constantly feeding me with great ideas and thoughts to work on, for basically everything that is making you being yourself! Hopefully we're gonna continue successfully coping with each other, thanks to combination of synergies. When do we play toddler-size chess?

Kai-Uwe Hess, thank you for being around, for endless discussions with a glass of wine or beer, for sharing so much of your incredible knowledge about the properties and the structure of silicate melts, for efficient manuscript proof-reading and so on and so forth. You will always remain a great resource!

Betty Scheu, vielen Dank für die schöne Unterstützung, wenn Yan das Department abgeschieden hat. Thanks for taking care of me, for taking care of the press lab refurbishment and for helping me to cope with the workshop! I wish that all the efforts we put in this new and fresh second-hand lab are gonna be fruitful. Can't wait! And, most importantly, thank you for kicking my ass in necessary times!

Ulli Küppers, un trou bavarois, thanks for all the good laughs but also for the exciting science we might have shared here and there. And thanks for dragging me out for a pizza from time to time!

To my new neighbours, Basti Wiesmaier and Corrado Cimarelli, thanks for your kind support throughout. Basti, you introduced me to the good things in life: road and mountain biking. Thanks for that! And also thanks for helping me find my way through bureaucracy and for a last minute request on my thesis. Corrado, ora avete un meraviglioso piccolo copia di te stesso, tutto il meglio! Thanks for your constant happiness and these flickers in your eyes when talking about any kind of subject!

Thanks to my co-authors for very appreciated contributions, in particular Andy Bell and Ian Main; keep playing statistics! I use these lines to also thank the reviewers of my first paper, who made it legit and had invaluable comments; thank you John Castro and Mike Heap! John, see you in Mainz one day? Mike, see you later this week in Strasbourg!

Thanks to Simon Kremers and Joachim Wassermann, who both gave me the opportunity to do some volcano-seismology at the very beginning of my stay. Thanks for introducing me to Python and its amazing world; I now just can't work without it!

Thanks to Andre Schöttler, my favorite Computermeister, for hosting my early months in the department, and for his availability and efficiency. Du weißt was du tust und Du tust es immer gut!

To Jenny Schauroth, thanks for distracting me from time to time, for your perpetual good mood and humour whatever the circumstances, and for an outstanding avocado cake!

To my fellow compatriots, Guilhem Douillet and Oryaëlle Chevrel, thanks for being here, for your frenchiness, for numerous talks we had (either political of about life in general), for taking me to refresh myself in the Eisbach during hot summer days, and well done to both of you for your achievements on your respective PhD studies!

To the administrative staff: I raise my glass. Through my mother's job, I know the work it represents and the mess of it. I would like to especially thank Margot, Sandra, Carina, Rike, Marina, Renate, Lydia, Rosa and Isabel. I would also like to thank the technical staff for helping me here and there, and in particular Markus, Wolfgang, Max and Detlef.

A big thank you to all of you around: colleagues and friends; in no particular order (hoping

I forgot anyone): Jackie, Rosie, Roos, John, Klaus, Cristian, Laura, Daniele, Valeria, Danilo, Teresa, Sascha, Christoph, Miguel, Linda, Alex, Paul, David, Kate, Maren, Donjá, Alejandra, Nikita and Wenjia.

Un énorme merci à ma famille et, en particulier, à mes parents et à mon frèrot. Merci de m'avoir appris l'essentiel, de m'avoir toujours soutenu dans mes choix et d'avoir fait en sorte que je puisse aller jusqu'au bout. Merci à mes amis de longue date en France ou ailleurs, pour être passés faire un coucou (ou pas) ici et là : Kalek, Conchi et D.D.

And last but not least or as we say in French the best at the end: a very special thank you to my wife and my children. Barbara, merci pour tous tes efforts, pour avoir accepté de me suivre presque les yeux fermés, pour avoir supporté mes hauts et mes bas, mais aussi pour m'avoir soutenu en toutes circonstances et m'avoir poussé lorsque c'était nécessaire. Mes enfants, Killian et Albane, peut-être un jour lirez-vous ces lignes et vous rendrez-vous compte que le plus important dans la vie c'est de se faire plaisir, tout en restant simple et humble.

Preamble

Most of the contents of this doctoral dissertation have been presented in scientific journals in a slightly modified form; namely

Lavallée, Y., Mitchell, T. M., Heap, M. J., Vasseur, J., Hess, K.-U., Hirose, T., & Dingwell, D. B. (2012). Experimental generation of volcanic pseudotachylytes: Constraining rheology. *Journal of Structural Geology*, 38, 222–233, doi:10.1016/j.jsg.2012.02.001.

Vasseur, J., Wadsworth, F. B., Lavallée, Y., Hess, K.-U., & Dingwell D. B. (2013). Volcanic sintering: Timescales of viscous densification and strength recovery. *Geophysical Research Letters*, 40(21), 5658–5664, doi:10.1002/2013GL058105.

Lavallée, Y., Wadsworth, F. B., Vasseur, J., Russell, J. K., Andrews, G. D. M., Hess, K.-U., von Aulock, F. W., Kendrick, J. E., Tuffen, H., Biggin, A. J., & Dingwell, D. B. (2015). Eruption and emplacement timescales of ignimbrite super-eruptions from thermo-kinetics of glass shards. *Frontiers in Earth Science*, 3(2), doi:10.3389/feart.2015.00002.

Vasseur, J., Wadsworth, F. B., Lavallée, Y., Bell, A. F., Main, I. G., & Dingwell, D. B. (2015). Heterogeneity: The key to failure forecasting. *Scientific Reports*, 5, 13259, doi:10.1038/srep13259.

Vasseur, J., Wadsworth, F. B., Lavallée, Y., & Dingwell, D. B. (2016). Dynamic elastic moduli during isotropic densification of initially granular media. *Geophysical Journal International*, 204, 1721–1728, doi:10.1093/gji/ggv550.

Je suis de ceux qui pensent que la science est d'une grande beauté. Un scientifique dans son laboratoire est non seulement un technicien : il est aussi un enfant placé devant des phénomènes naturels qui l'impressionnent comme des contes de fées. Nous ne devrions pas laisser croire que tout progrès scientifique peut être réduit à des mécanismes, des machines, des rouages, quand bien même de tels mécanismes ont eux aussi leur beauté.

Marie Curie

1

Introduction

UNDERSTANDING VOLCANIC PROCESSES IS OF PARAMOUNT IMPORTANCE for scientists dealing with hazard assessment and risk mitigation. For just over a century modern volcanology has often solely been based on field observations without leading much quantitative usable information. Volcanologists were mostly adapting and combining the tools and methodologies used in classical geology. Since volcanic environments are highly dynamic systems involving a wide range of physico-chemical conditions, it became clear over the years that volcanology is not a science on its own but rather multiple sciences combined at once. In fact, volcanology is the phenomenological study of volcanic eruptions and magmatic processes, and in recent years its progress has heavily tied in with the integration of adjacent disciplines of fundamental sciences (*e.g.*, material science).

For the past three decades or so, the development of modern technologies (mainly due to the increase in computer capacities) has allowed volcanologists to systematically, quantitatively and rigorously monitor volcanic activity, probe volcanic materials and reproduce volcanic phenomena in the laboratory as well as numerically. However, the broad spectrum of physico-chemical events occurring at, around and underneath volcanoes still makes it challenging to understand the big picture. One has to focus on certain aspects of volcanic activity, if one is to constrain the underlying mechanisms involved in terms of fundamental physico-chemical processes. With the advent of physical and experimental volcanology the approaches employed to tackle these problems have greatly improved our knowledge of a range of magmatic and volcanic phenomena.

Experimentation is in general at the heart of the scientific procedure. When feasible, experiments are designed to (a) explore processes in a controlled environment, (b) constrain the key parameters and (c) validate either conjectures or models (both theoretical and computational). For magmatic processes and volcanic eruptions, where direct observation is somewhat arduous and sometimes practically quasi-impossible, we can see that mimicking the same mechanisms under certain assumptions and simplifications yields central results and interpretations to feed back into field observations. The principal sources of field data derive from geophysical and geochemical monitoring, and from description of volcanic deposits. Interpretation of processes are thus often inferred from remarkable features of those signals and/or of those deposits, which inherently remain to be tested against empirical or theoretical laws. Experiments are key to describe material behaviour and physico-chemical processes, but they have their limitations; one of which being the scaling issue that is common to almost all fields of experimental geosciences. One has to distinguish between categories of experiments, if one is to characterise small-scale processes or large-scale dynamics [Mader et al., 2004]. Natural materials are generally preferred for the study of the former because scaling may not, in some cases, be an issue (*i.e.*, the time and lengthscales investigated often scale directly with those of the natural system), whilst analogue materials are usually favoured to investigate the latter.

Natural volcanic materials are highly complex structures: they are generally multiphase systems (mainly melt, bubbles and crystals), which contain varied amounts of dissolved chemical elements under pressure-temperature conditions acting at volcanoes. Consequently, their physico-chemical properties spans the widest spectrum amongst geomaterials and their complexities hinder systematic reproducibility when experimenting. Synthetic materials may help circumvent these issues, as they have the advantages of being a simplified version of the natural ones and of having well-constrained properties. Under specific circumstances natural materials can be reduced to two-phase by the use of synthetics. Let me take the example of volcanic ash. During volcanic fragmentation quantities of ash are ejected and most of this ash has been shown to be overprinted by the glassy component. It is therefore clear that the use of chemically stable, synthetic glasses, such as borosilicate or soda-lime silicate glasses, is very much relevant to explore the behaviour of their natural counterparts [*e.g.*, Hess et al., 2007;

Robert et al., 2008b; Whittington et al., 2009; Cordonnier et al., 2012b]. Here I make use of these synthetic glasses to create two-phase systems (melt and bubbles) for which the role of structural heterogeneity is easily picked apart. This well-constrained simplification of the natural system also allows to pin down the dominant first-order effects at the expense of the complexities.

The careful choice of experimental materials is important and so is the choice of the experimental setup. An experiment needs to be design in a way to describe a process simply, without ever oversimplifying it. Well-controlled experiments are commonly not designed to replicate and capture the entire complexity of volcanic conduits conditions, which would prove very challenging and somewhat not necessary to characterise the system's behaviour. Here I perform experiments under a uniaxial compression state (at temperatures relevant to magmas) for which the associated stress field is quite similar to shallow magmatic systems where a negligible amount of confining pressure is applied and the vertical stress exerted by the underlying magma dominates. The suitability of this type of deformation experiments in the study of volcanic processes has been extensively demonstrated [*e.g.*, Lejeune & Richet, 1995; Quane & Russell, 2005, 2006; Lavallée et al., 2007; Hess et al., 2008; Lavallée et al., 2008; Robert et al., 2008b,a; Quane et al., 2009; Benson et al., 2012; Lavallée et al., 2012; Kendrick et al., 2013; Lavallée et al., 2013; Heap et al., 2014].

In the final ascent trough the Earth's upper crust, magmas dominantly deform in a viscous manner; yet they may experience abrupt transition to a brittle regime of deformation, as they experience strong non-linear deviations in flow behaviour. In silicic systems, where the magmas involved are so viscous, this transition implies that these magmas regularly switch between flow and failure. This cycling between liquid-like and solid-like responses imparts very special properties and represents a prodigious seismogenic source. Structural and textural studies of eroded, exposed volcano interiors and volcanic products have revealed a plethora of lines of evidence for cyclic ductile-brittle events that involve repeated fracturing and seismicity [Tuffen et al., 2003; Tuffen & Dingwell, 2005]. Using analogous acoustic signals, experiments tend to constrain the source mechanisms on the microscale [Benson et al., 2007; Burlini et al., 2007; Benson et al., 2008; Lavallée et al., 2008; Tuffen et al., 2008; Benson et al., 2010, 2012; Lavallée et al., 2012; Arciniega-Ceballos et al., 2014; Benson et al., 2014; Kendrick et al., 2014] and this approach promises to improve our understanding of volcano-seismology. Volcano-seismic signals are the largest and arguably the most reliable precursory type of activity to volcanic eruptions. Laboratory-sized microseismic signals produced during rock or magma deformation are equally reliable as a tool to describe and analyse accelerating trends prior to sample-sized failure.

All the considerations listed above yield a fundamental outstanding question: what material properties determine the seismic signals associated with failure and how do they modify the efficacy of failure forecasting models? The present thesis aims at addressing this question by means of static and dynamic experiments. Specifically the study investigates the role payed by structural heterogeneities in magmas on the style and mechanisms of deformation during ascent in the shallow volcanic conduit and on the subsequent ability to predict magma failure (*i.e.*, magma fragmentation) based on accelerating rates of precursory seismicity. To this end, two major routes have been identified: (1) high-temperature static experiments using crushed synthetic glasses (crystal-free, amorphous systems) to explore the way structural heterogeneities such as pores evolve in shallow magmas and porous lavas, while statically measuring the resultant microstructural and elastic properties; and (2) high-temperature, high-

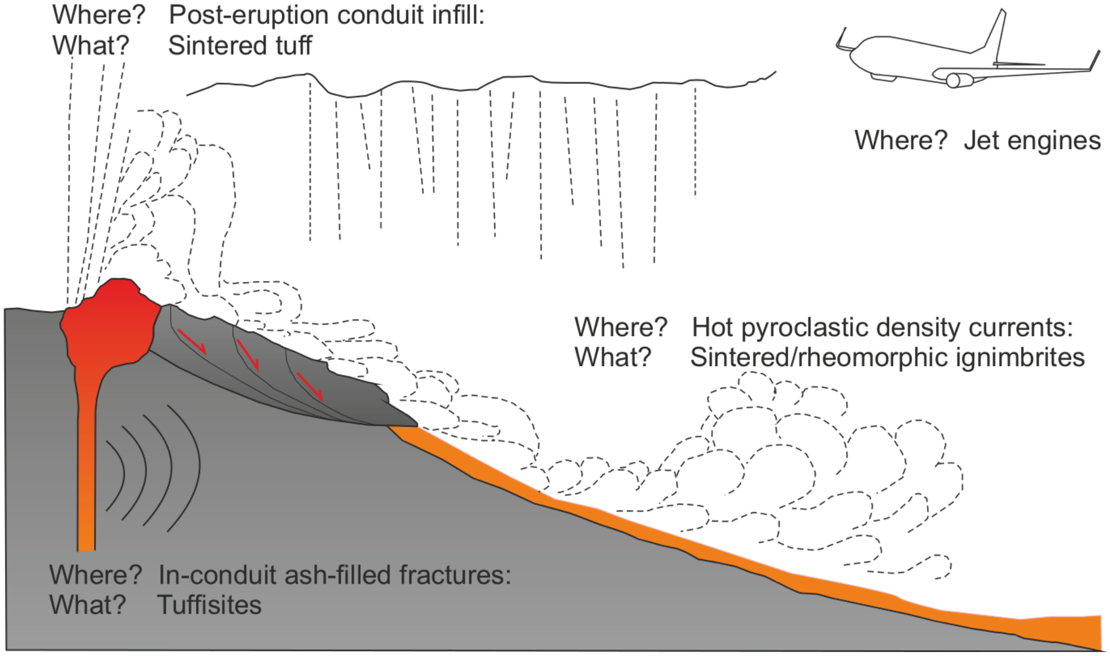

Figure 1.1: Densification and healing of volcanic ash is evident at many places in a volcanic environment.

load dynamic experiments on reconstituted synthetic magmas to probe their micromechanical behaviour, while dynamically measuring the elastic properties, as well as to simultaneously record their microseismic behaviour in order to apply failure forecasting laws.

In a volcanic environment, densification and healing of granular volcanic materials may occur in various places (Figure 1.1). Welding or sintering of particles due to pressure-temperature conditions encountered is invoked as the principal physical mechanism responsible for ash agglutination and annealing. Common scenarios in nature include (a) syn-eruptive in-conduit welding of ash-filled fractures, which are thought to be the source for tuffisite formation; (b) post-eruptive conduit infill leading to the formation of sintered tuffs; (c) post-eruptive welding of ash upon deposition of hot pyroclastic density currents, which form rheomorphic ignimbrites; and even (d) sintering of ash in jet engines, which is a major threat to civil aviation. Because the dominant constituent of volcanic ash is often glass, all these scenarios happen under the action of viscous forces, thereby making the study of these processes a typical rheological problem. The phenomenon of viscous sintering of a granular medium can be relatively easily reproduced in a laboratory environment with the use of adequate tools and has been extensively studied in the glass and ceramic industry. However, there are multiple ways to perform these kinds of experiments; following the technical designations used in industry: (a) free sintering, (b) isostatic pressing, (c) free forging and (d) constrained forging. All these terms relate to the stress field applied to the sintering sample at high temperature. In the aim to accurately decipher the key parameters and dominant timescales at stakes during viscous sintering of synthetic volcanic ash under near-static conditions, I opted for (a) in which case the surrounding stress field is inexistent.

Not only does viscous sintering provides me with mechanisms to study but also suites of variably sintered samples with different microstructural shape of their porous network. Such specimens may then be exploit for further experiments, as they now have well-constrained intrinsic material properties. In these porous glasses, if I assume that intensive properties such as the glass density are pretty constant across the matrix, description of an extensive property such as the amount of voids should directly reflect their degree of structural heterogeneity. Based on this assumption, well-controlled deformation experiments have been performed in order to investigate the effect of variable heterogeneity on the mechanical response and especially on macroscopic failure predictability. Explosive volcanic eruptions may similarly be considered as the result of a conduit-sized magma failure whereby the mechanical energy accumulated during ascent is suddenly released. However, as these natural environments are more complex dynamic systems than any experimental setup, they are controlled by the interaction of multiple processes that usually exhibit either non-linear or stochastic behaviour. The high level of uncertainty in the parameters governing these processes makes predicting the behaviour of volcanic systems highly problematic, whereas laboratory-based predictions are relatively simple and to some extent easy to resolve.

The present dissertation is structured around the two axes I have just described. Chapter 2 gives an extended, more in-depth introduction into the necessary building blocks from which the experiments have been mapped out. Chapter 3 introduces the outcomes of the first experimental campaign and discuss their implications for magmatic systems ("The Life and Death of Heterogeneity in Magmas..."). Chapter 4 deals with the second experimental campaign and shows how the results of the former influences the predictability of magma failure as well as discuss how it relates to volcanic eruptions ("...Implications for Failure Forecasting"). Chapter 5 finally presents the overall conclusions, summarises the whole study and discuss possible outlooks.

Today's scientists have substituted mathematics for experiments, and they wander off through equation after equation, and eventually build a structure which has no relation to reality.

Nikola Tesla

2

Theoretical background

This chapter essentially lays down and deals with the necessary general ideas (either purely theoretical, empirical or semi-empirical) serving as physical bases for the phenomena studied in the following chapters.

2.1 Continuum theory of sintering

Sintering is the process by which a granular medium is allowed to compact and particles to coalesce, ultimately resulting in a dense, pore-free material. The sintering process is classically divided into three stages [Swinkels & Ashby, 1981; Swinkels et al., 1983; Cocks, 1994] (Fig. 2.1): (1) a first stage in which the particles are brought into contact and necks grow at their surface contacts; in this phase the material may be modeled as an aggregate of individual particles with small surface contacts; for crystalline materials this phase involves the diffusion of vacancies in the crystal lattice, whereas non-crystalline materials sinter by viscous flow; (2) an intermediate stage in which the material can be idealised as an agglutinated frame with an interconnected porous network; this framework is inherently unstable with respect to surface tension in the absence of pore pressure and collapses causing the majority of volumetric strain via porosity reduction; and (3) a final stage in which, usually for relative densities greater than 0.9 [Coleman & Beere, 1975] (*i.e.*, for porosity less than 0.1), the closure of the porous network yields isolated, quasi-spherical pores (*i.e.*, gas bubbles) suspended in the liquid phase; these pores act to reduce the density from that of the pore-free material. It is important to note, however, that during the intermediate stage the pores can be considered quasi-spherical [Ashby, 1974].

The theory of sintering is based upon continuum mechanics, which has been successfully applied to the description of the compaction of porous bodies (this description being built on the theories of plastic deformation of porous bodies). Frenkel [1945] was the first to implement the rheological approach for sintering. The relationship determining sintering kinetics was derived on the basis of the analysis of two model problems: (1) joint sintering of two equal

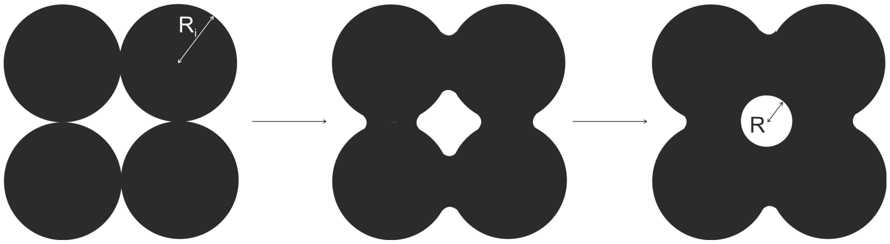

Figure 2.1: Schematic cartoon of the simplified spherical case of the sintering process. Sintering is a 3-stage process where (1) super-cooled silicate melt droplets form necks at grain-grain contacts, (2) the necks widen and encroach on the interconnected pore network, and (3) the porous network is closed leaving suspended isolated pores that relax to spherical.

spherical particles and (2) shrinkage of a spherical pore in an infinite viscous medium. These ideas were amplified and further developed by Mackenzie & Shuttleworth [1949]. They elaborated a method of macroscopic description of sintering as a uniform overall compression of a porous medium characterised by two viscosities.

2.1.1 A CONSTITUTIVE LAW

The continuum theory of sintering describes the macroscopic behaviour of a viscous, porous body during sintering. A porous medium is considered as a two-phase material constituted of (1) a substance phase[1] and (2) a void phase[2]. The skeleton, in turn, can be a heterophase material (*e.g.*, crystals embodied in a liquid), but for the theory developed hereafter I will stick to a single-phase viscous melt. The skeleton is assumed to be composed of individual particles. I will consider the case of a linear viscous incompressible skeleton containing isotropically distributed pores (intermediate and final stages of sintering). The overall mechanical behaviour of this porous body is therefore strongly influenced by the presence of pores [Wakai

---

[1] From now on referred as the "body skeleton" or the "melt".

[2] From now on referred as the "pores".

et al., 2007] and isotropic. One phenomenological rheological model is proposed by Olevsky [1998], which relates the stress tensor's components σ_{ij} (*i.e.*, externally applied load) to the deviator of the strain rate tensor's components $\dot{\varepsilon}_{ij}'$. A modified version of the law reads as follows

$$\sigma_{ij} = 2\eta_{\circ} \left(\eta_r \dot{\varepsilon}_{ij}' + \varkappa_r \dot{\varepsilon}_{ii} \delta_{ij} \right) + p_L \delta_{ij} - p_p \delta_{ij} \tag{2.1}$$

for which $\eta_{\circ}$ is the shear viscosity of the melt, η_r and $\varkappa_r$ are the relative shear and bulk viscosity respectively, $\dot{\varepsilon}_{ii}$ is the first invariant of the strain rate tensor $\dot{\varepsilon}_{ij}$, p_L is the Laplace pressure, p_p is the gas pressure in the pores, and δ_{ij} is the Kronecker symbol (*i.e.*, $\delta_{ij} = 1$ if $i = j$ and $\delta_{ij} = 0$ otherwise). The relative shear and bulk viscosities are defined as

$$\eta_r = \frac{\eta}{\eta_{\circ}}; \qquad \varkappa_r = \frac{\varkappa}{\varkappa_{\circ}} \tag{2.2}$$

where η and $\varkappa$ are the shear and bulk viscosities of the porous material respectively, and $\eta_{\circ}$ and $\varkappa_{\circ}$ those of the melt.

The first term of the right-hand part of Eq. 2.1 represents the material resistance, the second term corresponds to the influence of capillary stresses and the last term to the influence of internal pore stresses ($p_p = 0$ during the first and intermediate stages, since the pores are all interconnected). In essence, Eq. 2.1 measures the macroscopic deformation process by local shrinking (whenever it entails a volume reduction) and by local change in shape caused by viscous flow of the porous body. Introducing the following expression for the deviatoric strain rate tensor

$$\dot{\varepsilon}_{ij}' = \dot{\varepsilon}_{ij} - \frac{1}{3} \dot{\varepsilon}_{ij} \delta ij \tag{2.3}$$

Eq. 2.1 can be transformed into

$$\sigma_{ij} = 2\eta_0 \left(\eta_r \dot{\varepsilon_{ij}} + \left(\varkappa_r - \frac{1}{3}\eta_r \right) \dot{\varepsilon_{ii}} \delta_{ij} \right) + p_L \delta_{ij} - p_p \delta_{ij} \tag{2.4}$$

Now, if I consider an axisymmetric cylindrical specimen subjected to an external load, the average stress distribution and the strain rate tensor can be written as

$$\sigma_{ij} = \begin{bmatrix} \sigma_r & 0 & 0 \\ 0 & \sigma_r & 0 \\ 0 & 0 & \sigma_z \end{bmatrix}; \qquad \dot{\varepsilon_{ij}} = \begin{bmatrix} \dot{\varepsilon}_r & 0 & 0 \\ 0 & \dot{\varepsilon}_r & 0 \\ 0 & 0 & \dot{\varepsilon}_z \end{bmatrix} \tag{2.5}$$

where z denotes the axial direction and r the radial direction. Henceforth, the first invariant of the strain rate tensor corresponds to

$$\dot{\varepsilon_{ii}} = \dot{\varepsilon}_z + 2\dot{\varepsilon}_r \tag{2.6}$$

Summing over the stress and strain rate tensor's components in Eq. 2.4, and using Eqs. 2.5 and 2.6 yields the following expression

$$\sigma_z + 2\sigma_r = 6\eta_0 \varkappa_r \left(\dot{\varepsilon_z} + 2\dot{\varepsilon_r} \right) + 3p_L - 3p_p \tag{2.7}$$

Porosity dependence of the constitutive parameters

Determination of the overall effective response of a viscoplastic heterophase body in terms of the thermo-mechanical and geometrical characteristics of its constituents has been a long-standing challenge for material scientists. The dependence of the effective properties on porosity is just one particular case. For porous materials, a considerable amount of work has been carried out on materials with linear viscous and power law creep behaviour [Skorohod, 1972; Hsueh et al., 1986; Venkatachari & Raj, 1986; Rahaman et al., 1987; Cocks, 1989; McMeeking & Kuhn, 1992; Du & Cocks, 1992a,b; Kuhn & McMeeking, 1992]. For the determination of the relative shear and bulk viscosities, I will stick to the approach developed by Skorohod [1972]. Following a hydrodynamic analogy of the theory of elasticity, for which a corresponding problem can be solved assuming elastic properties of the material due to the similarity between the constitutive equations describing the behaviour of linear viscous and linear elastic materials, he derived the following approximation

$$\eta_r = (1-\varphi)^2 \tag{2.8}$$

for the relative shear viscosity, and

$$\varkappa_r = \frac{2\,(1-\varphi)^3}{3\varphi} \tag{2.9}$$

for the relative bulk viscosity. Here φ denotes the porosity.

At the microscopic level, the Laplace pressure is the result of collective action of local capillary stresses in a porous material (*i.e.*, the interstitial pressure acting at the surface of the pores or of the particles, thereby providing a sintering driving potential). The relationship between the relative p_{Lr} and the local Laplace pressure p_{L0} (acting on a single pore) depends on the procedure of averaging the aforementioned local stresses over a macroscopic porous volume. A substantial number of publications is dedicated to this topic [Coble, 1961; Skorohod, 1972; Scherer, 1979; Bhat & Arunachalam, 1980; de Jonghe & Rahaman, 1984; Hsueh, 1985; Rahaman et al., 1986; Hsueh et al., 1986; Raj, 1987; de Jonghe & Rahaman, 1988]. I will consider the derivation based upon the 3D stochastic approach employed by Skorohod [1972]. The achieved result may be stated as follows

$$p_{Lr} = (1 - \varphi)^2 \tag{2.10}$$

After Laplace's original work, the local Laplace pressure acting on any spherical surface reads as

$$p_{Lo} = \frac{2\Gamma}{r} \tag{2.11}$$

for which Γ is the surface tension and r is the radius of the sphere. For convenience, r can be generalised to either the characteristic radius of a pore or of a particle. The product of the local and the relative Laplace pressure gives its general expression (*i.e.*, $p_L = p_{Lo} p_{Lr}$)

2.1.2 POROSITY KINETICS DURING FREE SINTERING

During the first and intermediate stages of sintering $p_p = 0$ and in the case of free sintering (*i.e.*, $\sigma_z = 0$ and $\sigma_r = 0$), Eq. 2.7 becomes

$$\dot{\varepsilon}_z + 2\dot{\varepsilon}_r = -\frac{p_L}{2\eta_0 \varkappa_r} \tag{2.12}$$

Because of mass continuity and of the assumed incompressibility of the matrix (the shrinkage is only due to porosity change), the evolution law for porosity is given by [Olevsky, 1998]

$$\dot{\varepsilon}_z + 2\dot{\varepsilon}_r = \frac{\dot{\varphi}}{1 - \varphi} \tag{2.13}$$

Combining Eqs. 2.12 and 2.13 further leads to the continuum porosity kinetics during free densification of a porous body from an initial packing of particles to a bubble-bearing suspension

$$\frac{\dot{\varphi}}{1-\varphi} = -\frac{p_L}{2\eta_0 \varkappa_r} \tag{2.14}$$

Injecting Eqs. 2.9, 2.10 and 2.11 into Eq. 2.14 yields the following differential equation

$$\frac{\dot{\varphi}}{\varphi} = -\frac{3\Gamma}{2\eta_0 r_i} \tag{2.15}$$

which, once integrated between the initial porosity $\varphi\left(t=0\right) = \varphi_i$ and $\varphi\left(t\right)$, gives the approximated form of the porosity evolution of a relaxing porous body derived from the work of Mackenzie & Shuttleworth [1949]

$$\varphi\left(t\right) = \varphi_i \exp\left(-\frac{3\Gamma}{2\eta_0 r_i}t\right) = \varphi_i \exp\left(-\frac{t}{\lambda_{MS}}\right) \tag{2.16}$$

where λ_{MS} is the sintering timescale given by

$$\lambda_{MS} = \frac{2\eta_0 r_i}{3\Gamma} \tag{2.17}$$

2.2 THEORY OF FRACTURE MECHANICS

Fracture mechanics applies the physics of stress and strain in deforming solids to problems invoking the likelihood of fracture from the unstable propagation of pre-existing flaws or cracks. The theory identifies the conditions under which fracturing processes occur, and their dynamic and kinetic effects. Ultimately, it attempts to predict when fracture propagates and how a solid fails. Fracturing is inherent to many dynamic processes in the Earth system. Volcanic eruptions, in particular, are generally viewed as the result of magma ascent through fractures occurring on a broad range of lengthscales within the Earth's upper crust. Magmas themselves can equally fracture during transport and so it is reasonable to assume that under high deformation rates they respond like any other brittle material.

2.2.1 A FRACTURE CRITERION

In essence, Griffith [1921] was the first to propose a criterion of rupture based on the energy budget in a solid. He used the first law of thermodynamics to infer changes of the total energy as flaws or cracks grow. During elastic loading, a stressed body stores strain potential energy, which is provided by the work done on itself (in turn controlled by the forces applied), and releases this energy by creating new crack surfaces (*i.e.*, brittle cracking; conversion into a free surface energy). The balance between a crack driving force (energy storage) and a crack resisting force (energy release) is expressed by the total energy U of the system

$$U = U_m + U_s \tag{2.18}$$

for which U_m and U_s are the mechanical and the surface energy respectively. When a crack grows, U_m decreases and, accordingly, U_s increases. In the case of a thin plate under a constant load, the mechanical energy per unit width of a crack length l_c is given by [Lawn & Wilshaw, 1975]

$$U_m = -\frac{\pi l_c^2 \sigma^2}{4E} \tag{2.19}$$

where σ is the remote stress applied normal to the crack surface and E the Young's modulus. Griffith [1921] provides the expression for the surface energy per unit width of a crack length (for each surface of a crack), which depends on the surface energy density γ, as follows

$$U_s = 2 l_c \gamma \tag{2.20}$$

At equilibrium $\frac{dU}{dc} = 0$ and injecting Equations 2.19 and 2.20 into Equation 2.18 results in a critical failure stress σ_c, such that

$$\sigma_c = 2\sqrt{\frac{E\gamma}{\pi l_c}} \tag{2.21}$$

Equation 2.21 is a necessary criterion to explain the strength of elastic materials such as glasses or single crystals. However, in ductile materials (and, to some extent, in materials appearing to be brittle), plasticity at the crack tips starts to play a major role. In this case a dissipative term (corresponding to the release of heat at the crack tips) must be added in Equation 2.20. In the case of stressed brittle material, a crack may be energetically favourable to extend but, if its tip is not sharp enough to concentrate the applied stress and exceed its strength (Equation 2.21), it will not propagate. Since the theory developed by Griffith [1921] is based on thermodynamic equilibrium, it cannot predict the kinetics of a crack system that is perturbed from the equilibrium state. All these considerations pose a serious limitation to the applicability of this theory; the critical failure stress is not a sufficient criterion for material fracturing.

The works of Sneddon [1946] and Irwin [1958] widen the applicability of the ideas developed by Griffith [1921] by looking at the stress concentration and the stress field around a crack tip in an elastic body under stress. By introducing the notion of stress intensity factor (denoted as K), which depends on the crack geometry and on loading conditions (cast as a function f), it is shown that the stress around a crack tip depends on the angular coordinates r and ϑ, such that

$$\sigma_{i,j} = \frac{K}{\sqrt{2\pi r}} f_{i,j}\left(\vartheta\right) \tag{2.22}$$

Under mode I loading[3], the stress intensity factor in the vicinity of a crack tip is derived from Equation 2.22 as

$$K_I = \sigma\sqrt{\frac{\pi l_c}{2}} \tag{2.23}$$

This stress intensity factor provides a sufficient criterion for fracture propagation since it represents a measure of the stress singularity at the crack tip. Therefore, unstable crack propagation will occur if $K_I > K_{Ic}$. The critical stress intensity factor K_{Ic} is also known as the fracture toughness of a material. While K is a local parameter, a global parameter related to the crack growth energetics may be defined. This is quantified by the strain energy release rate G and the relationship with K under mode I loading is given by Lawn [1993]

$$K_I = \sqrt{EG_I} \tag{2.24}$$

By taking account of the stress field surrounding a crack, its geometry and material properties, the stress intensity approach gives insight into the mechanisms responsible for crack initiation and propagation in elastic materials.

2.2.2 Subcritical crack dynamics

Time-dependent deformation during elastic loading is termed "subcritical" since it refers to stable, quasi-static crack growth below a critical value of the stress intensity factor or of the

---

[3] Mode I fracturing describes an opening action (*i.e.*, tensile stress normal to the plane of the crack).

strain energy release rate. Subcritical crack dynamics is inherently sensitive to the applied stress, temperature and chemical environment. Several kinetic laws of crack growth have been therefore proposed to describe crack growth velocity v_c as a function of the stress intensity factor [Anderson & Grew, 1977; Atkinson, 1982]. One of the most commonly used expression for subcritical crack growth velocity is the power law proposed on purely empirical grounds by Charles [1958]

$$v_c\left(t\right) = v_{c,i}\left(\frac{K}{K_i}\right)^n \tag{2.25}$$

with $v_{c,i}$ and K_i the crack growth velocity and the stress intensity factor at $t = 0$ respectively, and n the subcritical crack growth index. Equation 2.25 can be rationalised in terms of viscous behaviour in the vicinity of the crack tip [Maugis, 1985; Lawn, 1993] and is consistent with the growth of multiple cracks in stochastic granular medium [Main, 1999]. Other relationships have been developed [Charles & Hillig, 1962; Wiederhorn & Bolz, 1970; Lawn & Wilshaw, 1975; Lawn, 1993], including the following exponential model

$$v_c\left(t\right) = v_{c,i}\exp\left(\alpha K\right) \tag{2.26}$$

and

$$v_c\left(t\right) = v_{c,i}\exp\left(\beta G\right) \tag{2.27}$$

where α and β are constants. In Equations 2.25, 2.26 and 2.27 the temperature dependence can be introduced as an Arrhenian factor in the constants n, α and β respectively. In particular, Charles [1958] suggested the following relationship

$$v_c\left(T\right) \sim C\left(\frac{l_c}{l_{c,cr}}\right)^{\frac{n}{2}}\exp\left(-\frac{E_a}{RT}\right) \tag{2.28}$$

for which C is a constant, l_c and $l_{c,cr}$ are the crack length and critical crack length respectively, E_a the activation energy and R the universal gas constant.

2.3 The ductile-brittle transition in magmas

Magmas may be treated as elastic materials under certain conditions, but they inherently remain viscoelastic materials due to pressure and temperature conditions in volcanic systems. At depth a melt may be idealised as a relaxed, Newtonian fluid[4]; however, during ascent in the volcanic conduit, pressure, temperature, mechanical and chemical conditions are drastically changing such that it is generally pushed towards a non-relaxed state and forced to readily straddle the ductile-brittle transition, which often results in catastrophic failure and magma fragmentation [Dingwell, 1996]. This metastable region between relaxed liquid and unrelaxed glass is a thermo-kinetic barrier and is known as the glass transition interval. Crossing this interval does not always imply fragmentation (*e.g.*, if no deformation is applied) but always results in a state where the melt reacts as an elastic material. Following Maxwell [1866], the boundary between the relaxed and non-relaxed state may be defined according to a very simple viscoelastic model, which describes the structural relaxation timescale λ_r of the melt as

$$\lambda_r = \frac{\mu}{G_\infty} \tag{2.29}$$

for which μ and G_∞ are the Newtonian shear viscosity and the shear modulus at infinite frequency respectively. The shear viscosity η_0 defined earlier[5] would be equivalent to the Newtonian shear viscosity μ as long as the melt remains in a Newtonian state and Equation 2.29

---

[4] A fluid is considered as being Newtonian when it is in an equilibrium state (no deformation) or when its shear viscosity displays no dependence on the applied deformation rate.

[5] See Section 2.1.

would hold. One can already see that, when a melt is subjected to a shear stress, the structural relaxation timescale will compete against the deformation timescale (commonly given by the shear strain rate), thereby dictating the state of the melt [Dingwell, 1996]. This competition can be framed in terms of the dimensionless Deborah number (as classically used in rheology), which characterise the "fluidity" of a material by expressing the ratio of the characteristic relaxation timescale of the material to the observation timescale [Reiner, 1964]. Using Equation 2.29 the Deborah number De is thus given by

$$De = \frac{\eta_0}{G_\infty}\dot{\varepsilon} \tag{2.30}$$

It has been demonstrated experimentally that, for silicate melts, the onset of the non-Newtonian behaviour[6] and the onset of the brittle behaviour are reached when the strain rate approaches a 1000th and a 100th of the structural relaxation timescale respectively [Dingwell & Webb, 1989; Webb & Dingwell, 1990a,b; Cordonnier et al., 2012b]. Therefore, it straightforwardly follows that $De = 10^{-3}$ and $De = 10^{-2}$ for the non-Newtonian and brittle behaviour onset respectively. The glass transition, which defines the interface between glass and melt, is in the same way given by $De = 1$. Since the infinite-frequency shear modulus of all silicate melts does not vary significantly as a function of temperature and chemical composition, we tend to approximate it to 10^{10} Pa s for most practical (macroscopic) purposes [Dingwell & Webb, 1989]. Equation 2.30 allows us, in turn, to consider isorate lines in a Deborah number versus temperature space (Figure 2.2). In such a space the glass transition can be crossed by changing the strain rate and/or the temperature. For natural systems such as silicic vol-

---

[6] A fluid is considered as being non-Newtonian when it exhibits a strain rate dependence of its shear viscosity when sheared.

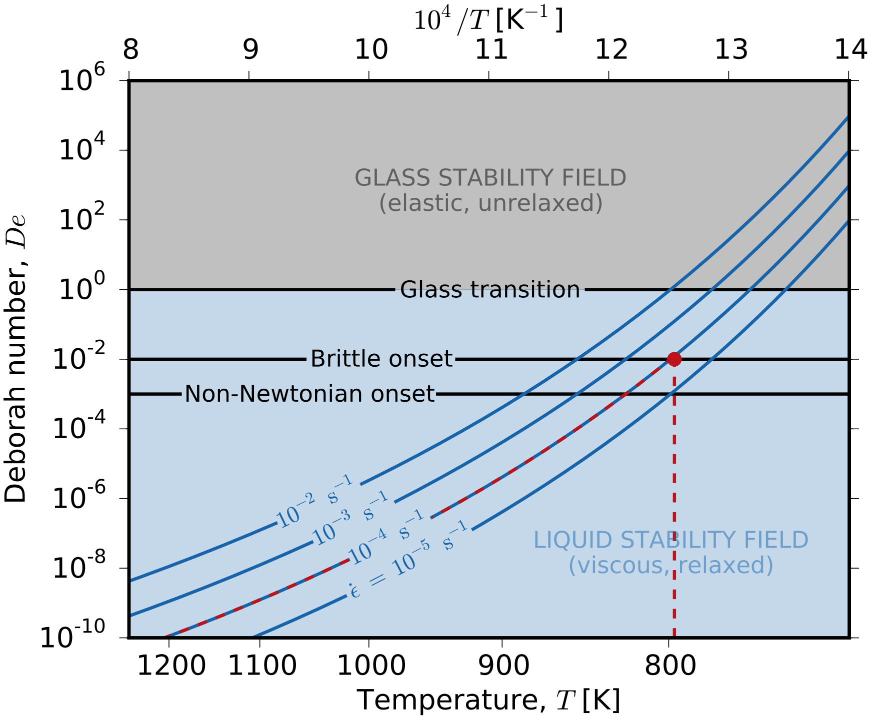

Figure 2.2: A map of the ductile-brittle transition in silicate melts. The dashed red lines are typical trajectories for a constant deformation rate (left) and an isothermal (right) process; the filled red circle indicates where the system-sized failure would occur. The solid blue lines are calculated using Equations 2.30 and 3.1.

canoes, it is more likely that the trajectory followed by the magma would be a combination of changes in strain rate and in temperature, with the failure point corresponding to magma fragmentation. Since magmas undergo chemical changes associated with volatile exsolution and crystallisation during ascent, it is reasonable to assume that the critical Deborah numbers defining the transitions will shift throughout an eruption [Cordonnier et al., 2012a]. Nevertheless, it remains that the trajectories invoked would almost always result in a shift from a coherent to a particulate melt, thereby providing mechanisms for the generation of heterogeneity within volcanic edifices. Conversely, this newly created particulate magma could transition again back to a pore-free, dense melt by following a re-heating trajectory and will be the subject of the next chapter.

Break a vase, and the love that reassembles the fragments is stronger than that love which took its symmetry for granted when it was whole. The glue that fits the pieces is the sealing of its original shape.

Derek Walcott

3

The death of heterogeneity

Sintering and densification are ubiquitous processes influencing the emplacement of both effusive and explosive products of volcanic eruptions. Here I sinter ash-size angular fragments of a synthetic NIST viscosity-standard glass (from the National Institute of Standards and Technology, USA) and near-spherical synthetic glass beads (produced by

Potters Industries Inc.) at temperatures at which the resultant melt has a viscosity of ∼10^8–10^9 Pa s and at ambient pressure conditions to assess sintering dynamics under near-surface volcanic conditions. I track the evolution of porosity and density during sintering, as well as elastic moduli, and the strength recovery via uniaxial compressive tests. I observe that volcanic ash sintering is dominantly time-, temperature- and particle size-dependent and may thus be interpreted to be controlled by melt viscosity and surface tension. Sintering evolves from particle agglutination to viscous pore collapse and is accompanied by a reduction in connected porosity and an increase in isolated pores. Sintering and densification result in a non-linear increase in strength. Micromechanical modelling shows that the pore-emanating crack model explains the strength of porous lava as a function of pore fraction and size.

3.1 SINTERING AS A WAY TO DENSIFY MAGMAS

Welding or sintering of volcanic ash and lava densification occurs by a combination of viscous flow and chemical diffusion, and takes place in a variety of volcanic settings. This process is evident in rheomorphically welded ignimbrites [Sparks et al., 1999], tuffisite veins [Stasiuk et al., 1996; Kolzenburg et al., 2012], shallow conduits [Tuffen et al., 2003; Tuffen & Dingwell, 2005], lava flows [Cabrera et al., 2011] and lava domes.

High-grade (high temperature) pyroclastic density currents can sinter during deposition, resulting in dense welded ignimbrites [*e.g.*, Smith, 1960; Ragan & Sheridan, 1972; Branney & Kokelaar, 1992] that are sometimes mistaken for lavas in the field. In this process, a density-graded particulate flow is thought to progressively agglutinate (*i.e.*, syn-deformational sintering) to a non-particulate, viscously deformable flow, forming a rheomorphic ignimbrite [Branney & Kokelaar, 1992]. The sintering or welding intensity can be estimated from strain markers in such deposits [Quane & Russell, 2005, 2006] and using existing experimental models, the timescale over which strain is accumulated can be estimated [Russell & Quane, 2005].

Fracture and subsequent healing also occurs in shallow conduits and lava domes [Tuffen & Dingwell, 2005]. This phenomenon is observed at all scales and is in all likelihood integral to the structural stability of lava domes. Thermochemical, kinetic investigation of fractures in obsidian has demonstrated the efficiency of these processes [Cabrera et al., 2011; Castro et al., 2012]. During this process, strength can be recovered and repeated fracture and healing may take place [Tuffen et al., 2003]. In some instances, fractures may be filled by fragmented particles generating tuffisite veins. Tuffisites form during magmatic fragmentation, subsequent transport through, and deposition in, fracture networks. Tuffisites consist of fine-grained fragments (1–10^3 µm) that relax and sinter *in situ*, forming diagnostic vein-filled brecciated textures [Tuffen et al., 2003; Tuffen & Dingwell, 2005; Kolzenburg et al., 2012]. Kolzenburg et al. [2012] have demonstrated that the strength of tuffisites can be recovered during the healing process and as such, suggested that the influence of tuffisites on the rheological, mechanical and physical behaviour of lava domes is limited to the timeframe over which the vein heals.

Rheological experiments have shown that during welding the apparent viscosity of the porous particulate lava progressively recovers in value to that of the liquid [Quane & Russell, 2003]. The rate of the process depends on stress and melt viscosity before vitrification (at the glass transition) or crystallisation [Smith, 1960; Sparks et al., 1999; Quane & Russell, 2005; Russell & Quane, 2005; Quane et al., 2009]. As the kinetics of the process is viscosity-dependent, the degree of densification could be strongly influenced by the presence of volatiles in the liquid phase [Hess & Dingwell, 1996] and thus by the availability of gas in the pore space to resorb into the liquid structure [Sparks et al., 1999]. Rheological studies addressing welding in volcanic systems have however neglected conditions in which no external stress is applied, where the fundamental mechanisms by which melt droplets coalesce yield the kinetics of the surface tension driven end-member of this process. In material science these phenomena are well-studied[1] [*e.g.*, Frenkel, 1945; Mackenzie & Shuttleworth, 1949; Scherer & Bachman, 1977; Prado et al., 2001]. Here I build on previous rheological studies to investigate the kinetics of sintering and magma densification to constrain, in turn, strength recovery during healing. Micromechanical analysis is then employed to provide a failure criterion for porous lavas.

3.2 EXPERIMENTAL METHODS

3.2.1 MATERIAL PROPERTIES

The process of glass particle sintering has been investigated using well-constrained materials: (1) a viscosity-standard borosilicate glass (SRM 717a) from the National Institute of Standards and Technology (NIST, USA), which I powdered into angular particles[2], and (2) populations of industrial soda-lime silica glass beads (Spheriglass® A-glass microspheres 1922 and 2530, Potters Industries Inc.) with known chemical and physical properties[3]. The chemical composition of these glasses is listed in Table 3.1. The NIST glass has been selected because it has a well-constrained temperature dependence of viscosity, a precise description of the calorimetric glass transition T_g interval (780–795 K at 10 K min^{-1} natural cooling rate), a deter-

---

[1] See Section 2.1.

[2] From now on referred as "NIST glass".

[3] From now on referred as "glass beads".

Table 3.1: Composition of materials.

Oxide	NIST glass	Glass beads
-	wt %	wt %
SiO_2	68	72.5
B_2O_3	18.5	-
Al_2O_3	3.5	0.4
MgO	-	3.3
CaO	-	9.8
Li_2O	1	-
Na_2O	1	13.7
K_2O	8	0.1
Fe_2O_3	-	0.2

mined fracture toughness [Wiederhorn, 1969], an excellent glass-forming ability (*i.e.*, it does not crystallise, degas or show liquid-liquid immiscibility at the experimental conditions and timescales), and has been used extensively in background studies to constrain volcanic processes [*e.g.*, Hess et al., 2007; Robert et al., 2008b; Whittington et al., 2009; Cordonnier et al., 2012b]. Similarly, the glass beads have been shown to be a chemically and thermally stable material over the experimental conditions and timescales investigated here (*i.e.*, the mass loss is negligible and the onset of the glass transition interval varies insignificantly over repeated heating cycles, and no crystallisation may occur below 970 K) [Wadsworth et al., 2014].

The temperature dependence of viscosity η_0 of the NIST glass is given by the following certified calibration of a Volger-Fulcher-Talmann (VFT) equation

$$\log_{10}(\eta_0) = -2.5602 + \frac{4852.2}{T - 465.762} \tag{3.1}$$

where T stands for temperature. The temperature dependence of viscosity of the glass beads has been predicted by using the multicomponent model of Fluegel [2007] developed for in-

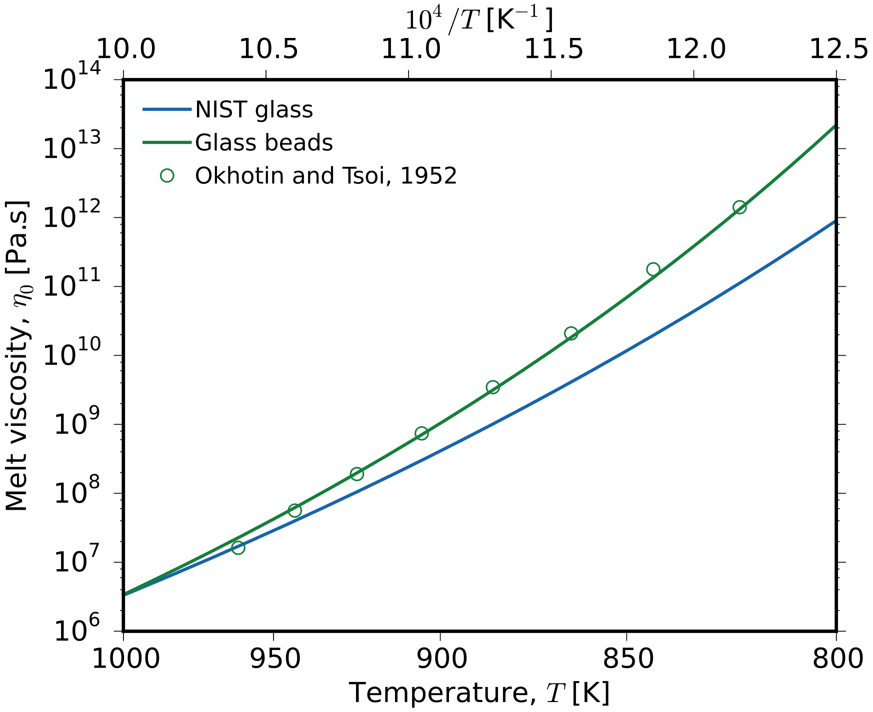

Figure 3.1: The temperature dependence of melt viscosity of the NIST glass from Equation 3.1 (calibrated and provided by NIST) and of the glass beads from Equation 3.2 (calculated after the composition-dependent model of Fluegel [2007]). The green open circles are viscosity measurements using a glass of near-identical composition to the glass beads.

dustrial glass-forming silicate melts. The resultant VFT equation reads as follows

$$\log_{10}(\eta_0) = -2.6387 + \frac{4303.36}{T - 530.754} \tag{3.2}$$

One can observe that Equations 3.1 and 3.2 are very close to each other (Figure 3.1), thereby providing a robust rheological comparable basis.

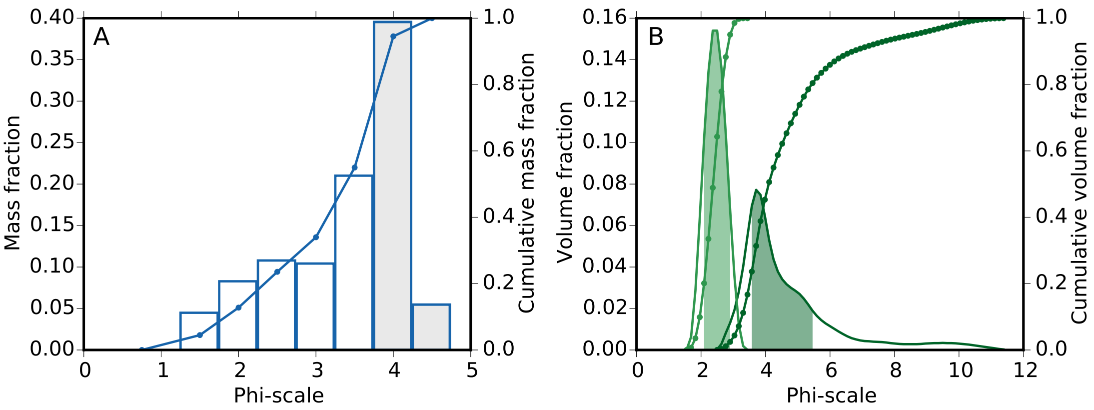

Figure 3.2: The particle size distributions of the experimental materials: (A) NIST glass powder (as measured from manual sieving) and (B) glass beads (as measured by laser refraction); the fine and the coarse distributions are displayed in dark and pale green respectively.

3.2.2 SAMPLE PREPARATION

I crushed the NIST glass to a powder using a concussion mill for intervals of 10–15 s and measured the resultant particle size distribution by sieving with half-phi intervals (Figure 3.2A). A laser refraction particle size analyser (LS230, Beckman Coulter Inc.) with a measuring range of 0.375–2000 µm was used to determine the particle size distributions of the two populations of glass beads (Figure 3.2B). The particle size distribution of both the NIST glass powder and the glass beads used are monomodal. The two glass beads populations have well-defined monomodal peaks at 76 and 177 µm from dark[4] to pale green[5] respectively. The distributions range between 0.4 and 177 µm, and 92 and 340 µm respectively. The NIST glass powder also has a monomodal peak around 63 µm and ranges between 44 and 354 µm. This powder consists of angular fragments (Figure 3.5A top-left), whereas the glass beads are near-spherical (Figure 3.5B top-left).

---

[4] From now on referred as the “fine” distribution.

[5] From now on referred as the “coarse” distribution.

I systematically filled alumina ceramic crucibles (44 mm in diameter and 75 mm in height) with particles, ensuring close to a maximum packing by tapping the powder flat every time I poured a few millimetres of particles in the crucible. The maximum packing is a function of the particle size distribution, sorting and clast angularity for heterogeneous powder populations [*e.g.*, Evans & Gibson, 1986]. As such, a compact of irregular fragments leads to a more dense packing that that of spherical particles, thus it is expected that the NIST glass powder compact to reach a lower porosity. The sample-laden crucibles were heated at 10 K min^{-1} to isotherms above the glass transition and at which the melt viscosity is 1.1×10^{8} and 2.24×10^{9} Pa s for the NIST glass and 2.09×10^{8} Pa s for the glass beads. Viscous sintering took place during dwells of 0.5 to 10 hours for the NIST glass powder and 1 to 32 hours for the glass beads. After sintering, the samples were cooled at a slower rate of $\sim$5 K min^{-1} to minimise cracks induced by the thermal contraction of the sample. Note that the sintering times shown here are the dwell time at the isotherm and do not include the heating and cooling portions of the sample excursions to and from high temperature. Due to the fast heating rate, sintering occurring during the heating portion above the glass transition temperature is considered negligible (for a treatment of non-isothermal sintering, see Wadsworth et al. [2014]). The samples show no preferential compaction at the base nor cracking; both of which would affect the bulk porosity. The densified products were drilled from the crucible to sample cores of 25 mm diameter by 50 mm height for further physical and mechanical analysis (Figure 3.3).

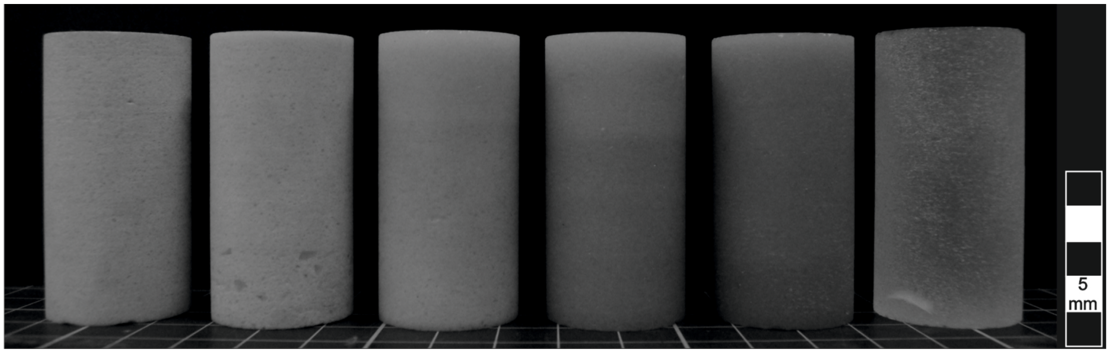

Figure 3.3: Typical suite of sintered glass sample cores using the NIST glass powder as starting material. The sintering time increases incrementally from the left to the right; the farthest right sample core being the pure NIST glass.

3.2.3 SAMPLE CHARACTERISATION

A physical description of the welded products requires an accurate description of the porous network. The total porosity φ_T is defined by the relative amount of pores in the sample and its counterpart the relative density ϱ_r by the relative amount of solid in the sample. By denoting the total volume as V_{total}, and the volume of the solid matrix V_{matrix} and of the pores $V_{pores} = V_{total} - V_{matrix}$, the relative density can be written as

$$\varrho_r = \frac{V_{matrix}}{V_{total}} = \frac{\varrho_{bulk}}{\varrho_0} \tag{3.3}$$

where ϱ_{bulk} and ϱ_0 are the bulk density and the density of the pore-free, dense material (*i.e.*, the solid matrix). Therefore, total porosity reads

$$\varphi_T = \frac{V_{pores}}{V_{total}} = 1 - \varrho_r \tag{3.4}$$

The connected porosity ϕ_C of the samples was measured by helium pycnometry (Micromeritics Accupyc 1330 and Quantachrome Ultrapyc 1200e). The isolated porosity was estimated from the difference between the total and connected porosity. The density of both the NIST glass and the glass beads is dependent on the cooling rate at which the melt crossed the glass transition interval and therefore I used a corrected glass density for the post-experimental samples given the cooling rate of $\sim$5 K min^{-1}.

Ultrasonic wave velocities were measured in a benchtop apparatus (Figure 3.4A), where the specimen is placed between two vertical endcaps equipped with piezoelectric transducers (with a resonant frequency of <1 MHz) connected to a pulse generator (Agilent Technologies 33210A, 10 MHz function/waveform generator) and an oscilloscope (Agilent Technologies DSO5012A). The onset of P-wave arrival at the receiver was individually picked as the first deviation from the baseline signal.

Oriented thin sections were obtained in the axial plane of the sintered samples and photomicrographs were recorded using an optical microscope in plane-polarised light. Accordingly, backscattered electron images of oriented thick sections of the sintered samples were recorded. The images were converted to binary, allowing for automatic thresholding of hues and greyscales to black and white. The minimum and maximum pore sizes were measured. These measurements were of connected vesicle widths in the case of the poorly sintered samples and of isolated vesicle radii in the case of the well-sintered samples.

A series of compressive deformation tests was performed on the prepared porous magmatic suspensions using a uniaxial press equipped with a surrounding furnace ($\leq$1373 K), which can apply a $\leq$300 kN force vertically (Figure 3.4B; see Hess et al. [2007] for details of the apparatus). These Uniaxial Compressive Strength (UCS) tests were performed on a

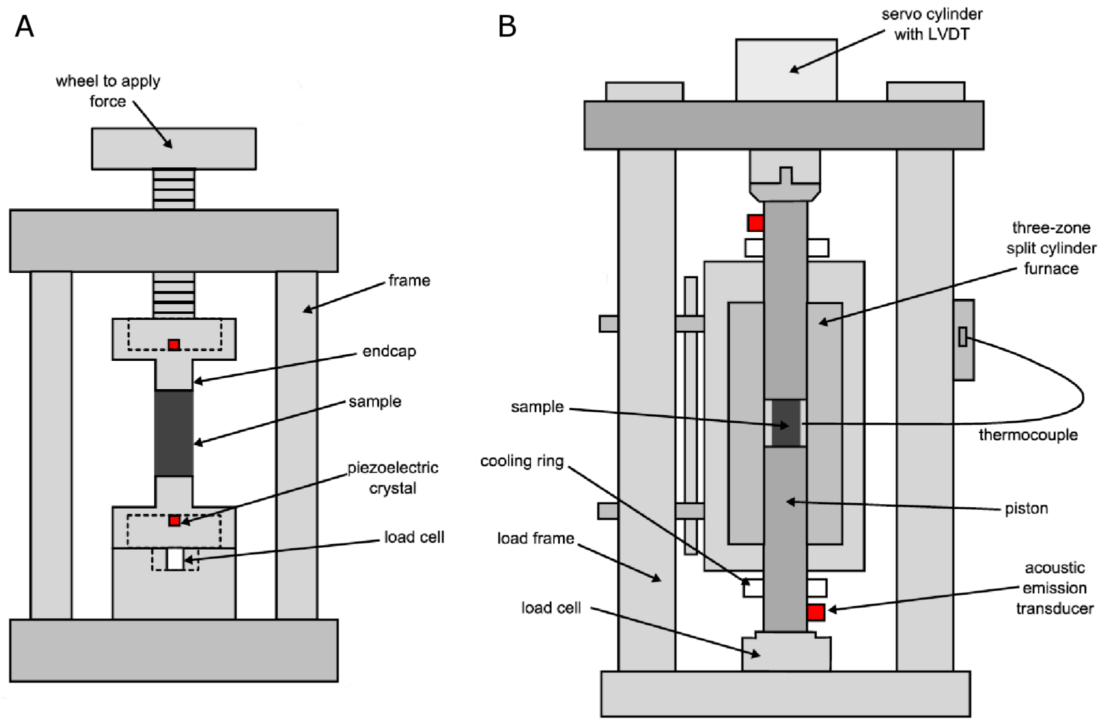

Figure 3.4: Schematic diagrams of the experimental devices used (A) to determine benchtop elastic waves velocities and (B) for uniaxial compression tests. Both schematics after Heap et al. [2014].

relaxed (liquid) magma at a temperature of ∼810 K in the case of the NIST glass and at a temperature of ∼825 K in the case of the glass beads. For both materials, these experiments were carried out slightly above the calorimetric glass transition interval. At this temperature a negligible amount of viscous sintering occurred on the timescale of the experiment due to the relatively high viscosity of the suspension (in contrast to the sintering experiment conditions). I loaded the porous magma up to failure at a constant strain rate of $\sim 10^{-3}\,\mathrm{s}^{-1}$ to ensure deformation in a purely elastic regime. In each experiment, the component of strain, which could not be viscously relaxed, resulted in a stress accumulation that triggered brittle failure; the peak axial stress was recorded as a measure of the UCS.

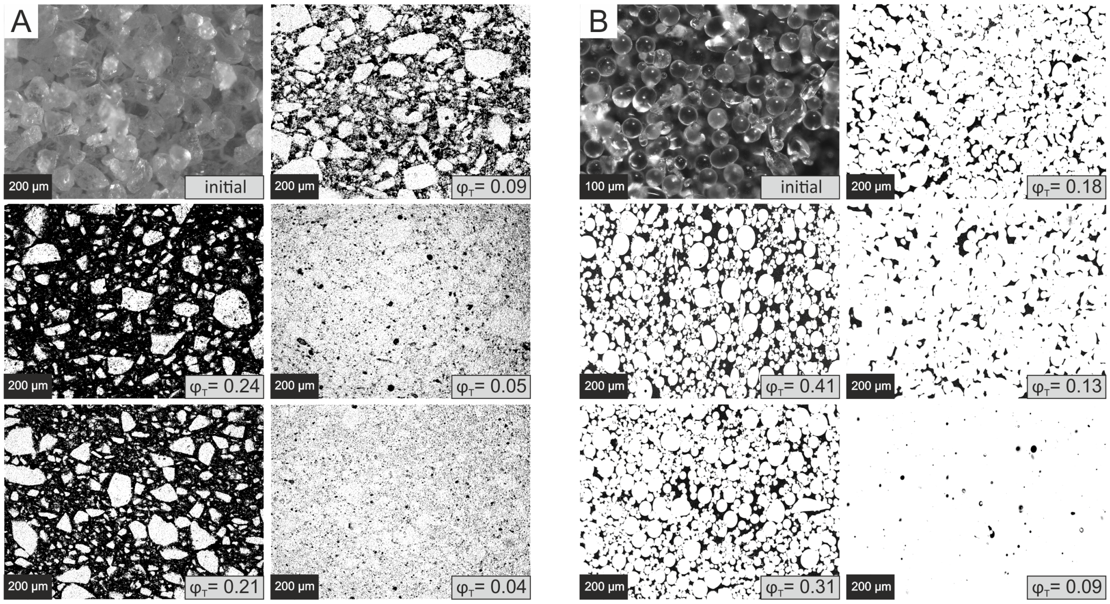

Figure 3.5: Textural evolution during sintering. (A top-left) Photomicrograph (reflected light) of the NIST glass powder sieved between 100 and 150 µm. (A middle-left to bottom-right) Binary false-colour thin section photomicrographs of NIST glass samples sintered at 923 K for incremental times. Black represents the pores and white the glass matrix. (B top-left). Photomicrograph (reflected light) of the coarse distribution of the glass beads. (B middle-left to bottom-right) Backscattered electron images in binary false-colour of thick sections of glass bead samples sintered at 923 K for incremental times. Black represents the pores and white the glass matrix.

3.3 DENSIFICATION AND HEALING OF SYNTHETIC GLASSES

Microstructural analysis reveals details of the sintering process. I note a rapid coarsening of the ash fragments due to agglutination. This densification process results, in turn, in an overall decrease in average pore size, which evolves from $\sim$1 to $\sim$0.01 mm over the sintering timescale in the case of the NIST glass powder (Figure 3.5). The findings are consistent with the general observation that sintering results in viscous pore collapse, densification, strengthening and elasticity recovery of porous lava.

3.3.1 Timescales and mechanisms

The total and connected porosity decrease during sintering, whereas isolated porosity increases (Figure 3.6). The rate of porosity change is influenced by the sintering temperature and the size of the particles. For the NIST glass powder, at 923 K the liquid has a viscosity of 1.1×10^8 Pa s and the total and connected porosity decrease from a common starting maximum packing value of ∼0.4 to a minimum value of 0.05 in the case of total porosity (Figure 3.6A) and 0 in the case of connected porosity (Figure 3.6B top). Simultaneously, the isolated porosity increases from 0 to ∼0.05 (Figure 3.6B bottom). At 873 K the melt viscosity is 2.24×10^9 Pa s and over the experimental time of 10 hours, the total and connected porosity evolve from ∼0.4 to ∼0.25 (Figure 3.6A) and to ∼0.2 (Figure 3.6B top) respectively. The isolated porosity evolves from 0 to ∼0.07 (Figure 3.6B bottom).

For the glass beads, at 923 K the liquid has a viscosity of 2.09×10^8 Pa s and the total and connected porosity decrease from the starting maximum packing value of ∼0.48 to a minimum value of 0.12 (Figure 3.6C) and of 0 (Figure 3.6D top) respectively. The timeframe over which the densification process occurs depends on the particle size distribution and one can observe that within 10 and 35 hours for the smallest and highest particle size distributions respectively, both porosities have reached their final values. For all particle size distributions, the isolated porosity increases from 0 to ∼0.12 (Figure 3.6D bottom). Relative density—the standard metric of sintering in ceramics and glass-technology studies—is inversely proportional to the total porosity (see Equation 3.4) and I observe that the preservation and accumulation of isolated porosity prevents the recovery of the defect-free glass density for both the NIST glass and the glass beads (Figure 3.7).

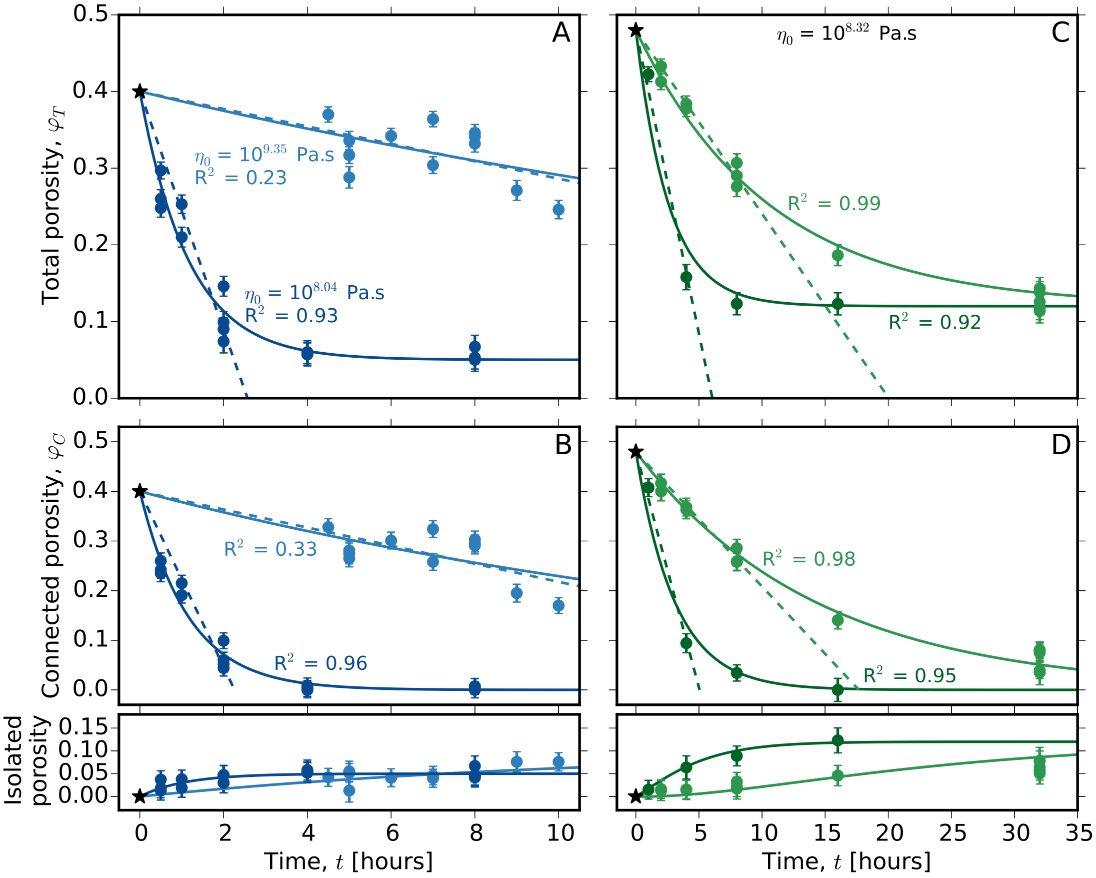

Figure 3.6: Results for porosity evolution in the sintered sample suite. The evolution of total, connected (top) and isolated (bottom) porosity with best-fit curves to the models (solid and dashed lines; see text) for (A) and (B) the NIST glass powder, and (C) and (D) the glass beads respectively. The colour coding of the NIST glass data refers to the two viscosities investigated and that of the glass beads data to the two particle size distributions investigated (see Figure 3.2B).

First stage sintering

As described in Section 2.1, sintering stages have been approximated by theoretical and empirical relationships. Neck formation is well-described by the Frenkel [1945] and Scherer & Bachman [1977] sintering models and variations of these studies which states that relative density

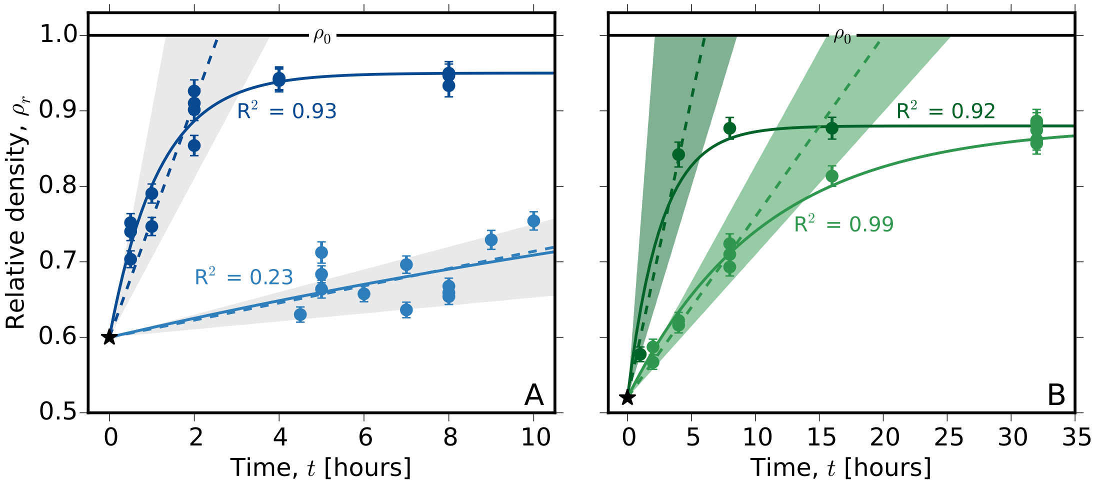

Figure 3.7: Results for relative density evolution in the sintered sample suite with best-fit curves to the models (solid and dashed lines; see text) for (A) the NIST glass and (B) the glass beads. The colour coding of the NIST glass data refers to the two viscosities investigated (see Figure 3.6A) and that of the glass beads data to the two particle size distributions investigated (see Figure 3.2B).

will increase with time between relative densities of 0.3 and a threshold value <1 [Frenkel, 1945; Scherer & Bachman, 1977; Scherer, 1977; Cahn, 1991]. I find that a combination of their approaches yields an empirical, linear relationship valid for the range of relative densities over which neck formation dominates, such that

$$\varrho_r(t) = 1 + \left(\varrho_{r,i} - 1\right)\left(1 - \frac{t}{\lambda_s}\right) \tag{3.5}$$

where $\varrho_{r,i}$ is the initial relative density, t is time since the onset of the isotherm and λ_s is the characteristic timescale of sintering. I can combine Equations 3.4 and 3.5 to derive the total porosity as a function of time (note that total and connected porosity are interchangeable in this particular case)

$$\varphi_T(t) = \varphi_{T,i}\left(1 - \frac{t}{\lambda_s}\right) \tag{3.6}$$

where $\phi_{T,i}$ is the total porosity at $t = 0$. Equations 3.5 and 3.6 show that the initial stage of isothermal viscous sintering can be approximated by a linear relationship with time. This model, which neglect externally applied stress, requires that viscous sintering is characterised by a dominant sintering timescale λ_s. Uhlmann et al. [1975] suggest that this timescale is related to the melt viscosity η_0, the melt-vapour interfacial tension Γ and the initial radius of the sintering particles $r_{p,i}$

$$\lambda_s = \frac{r_{p,i}\eta_0}{\Gamma} \tag{3.7}$$

I use a least squares regression to fit all the linear portions of the total and connected porosity data shown in Figure 3.6, as well as all the linear portions of the relative density data shown in Figure 3.7. For each experimental temperature (NIST glass) and each particle size distribution (glass beads), values of λ_s were adjusted such that they yield best-fit controlling particle sizes. The best-fit models are represented as coloured dashed lines in Figures 3.6 and 3.7.

For a melt surface tension of 0.3 N m^{-1} for a borosilicate E-glass of a similar composition [Kraxner et al., 2009] to the NIST glass, I find that the best-fit timescale for my data relates to a dominant particle radius of 17–25 µm in the case of the sintering NIST glass powder. This particle size range is consistent for both experimental temperatures and is in very good agreement with the particle size analysis, which indicates that the most frequent particle radii are in the range 26–37 µm and the finest fraction is <26 µm (grey shaded area in Figure 3.7A). In the case of the sintering glass beads, the best-fit timescale relates to a dominant particle radius of 31 and 103 µm for the dark and pale green data respectively, which is also in very good agreement with both particle size distributions indicating a dominant range of 10–45 µm (dark green shaded area in Figure 3.7B) and of 60–170 µm (pale green shaded area in Figure 3.7B). I therefore suggest that for unimodal distributions, it is the finest particle sizes that dominate the timescale of effective sintering because those particles will occupy the interstices of larger particles and share the most contact surface area for viscous neck formation. Prado et al. [2001] also concluded that Equation 3.7 holds, as the finest particles cluster in pore spaces between larger particles and control sintering rates due to the high stress at their surface driving sintering.

Intermediate and final stages sintering

In Equation 3.7 the driving stress for deformation is derived from the surface tension and the interconnected pore-geometries. The fact that I can approximate the evolution of porosity and density using Equation 3.7 implies that the deformation is viscous and that diffusive neck growth is not the dominant transport mechanism. Equation 3.7 is identical to the approximation for the viscous relaxation time of a bubble in a melt defined by Oldroyd [1953] in which $r_{b,i}$ is the initial bubble radius, such that

$$\lambda_d = \frac{r_{b,i}\eta_0}{\Gamma} \tag{3.8}$$

I note that there is a packing-dependent proportionality between $r_{p,i}$ of statically sintering particles in a granular material and $r_{b,i}$ of bubbles in the resultant viscously relaxing suspension. This consideration permits me to describe a continuum in the processes of sintering and bubble relaxation, as the material progresses from granular to a suspension medium. As such, the data can be empirically approximated by the following exponential expression

$$\phi_T(t) = \phi_{T,f} + \left(\phi_{T,i} - \phi_{T,f}\right) \exp\left(-\frac{t}{\lambda_d}\right) \tag{3.9}$$

where $\varphi_{T,i}$ and $\varphi_{T,f}$ are the initial and final total porosity respectively, and λ_d is the characteristic densification timescale, which is dominantly related to the bubble collapse and relaxation timescale. It is clear that Equation 3.9 is an adaptation of Equation 2.16 derived from theory[6], by accounting for the final porosity value (*i.e.*, the remaining isolated porosity when the sintering process is over). Because the total porosity includes isolated and connected pores, and because in some instances the results for viscous sintering show that the connected porosity decays to zero (*i.e.*, $\varphi_{C,f} = 0$; Figure 3.6B and D), Equation 3.9 becomes

$$\varphi_C(t) = \varphi_{C,i} \exp\left(-\frac{t}{\lambda_d}\right) \tag{3.10}$$

which is, indeed, the same as Equation 2.16 (although describing the evolution of total porosity). By injecting Equation 3.9 into Equation 3.4 one can provide the following relative density evolution with time

$$\varrho_r(t) = \varrho_{r,i} + \left(\varrho_{r,f} - \varrho_{r,i}\right)\left(1 - \exp\left(-\frac{t}{\lambda_d}\right)\right) \tag{3.11}$$

As for the first stage of sintering, a least squares regression analysis has been applied to all the total and connected porosity data shown in Figure 3.6, and all the relative density data shown in Figure 3.7. For each experimental temperature (NIST glass) and each particle size distribution (glass beads), values of λ_d were adjusted such that they yield best-fit controlling bubble sizes. The best-fit models are represented as coloured solid curves in Figures 3.6 and 3.7. I note that ${}^{r_{p,i}}/_{r_{b,i}}$ is $\sim$1.3–2.3 (Table 3.2), which is consistent with the pore space radii expected between particles of a heterogeneous population at maximum packing.

---

[6] See Section 2.1.

Table 3.2: Melt parameters known or estimated for use in sintering models (see text) and relative density model outputs.

Material –	T K	η_0 Pa s	Γ N m^{-1}	λ_s hours	$r_{p,i}$ μm	λ_d hours	$r_{b,i}$ μm	$r_{p,i}/r_{b,i}$ –
NIST powder	873	2.24×10^9	0.3	35.1	17	26.8	13	∼1.3
NIST powder	923	1.1×10^8	0.3	2.6	25	1.2	11	∼2.2
Fine beads	923	2.09×10^8	0.3	6.1	31	2.6	13	∼2.3
Coarse beads	923	2.09×10^8	0.3	20	103	10.6	54	∼2

The data presented in Figure 3.6 can be cast in a porosity space (*i.e.*, connected against total porosity), where the data points plot below the isoline (total = connected porosity) and any vertical distance from this isoline is given by the isolated porosity. I observe that both sintering NIST glass powder and glass beads data lie sub-parallel to the isoline and systematically deviate from it, as connected porosity decays to zero (Figure 3.8). Mechanisms such as cracking, crack healing, coalescence by bubble growth and bubble collapse have been inferred from trajectories in this porosity space [*e.g.*, Kennedy et al., 2010]. I observe that the sintering trajectories followed by the data points in Figure 3.8 indicate an overall pore collapse mechanism, which is consistent with the viscous sintering theory[7].

The efficacy of the models in Equations 3.9 and 3.10 can be tested by non-dimensionalisation of the controlling parameters. As such, a relative porosity ϕ_r can be defined as

$$\phi_r = \frac{\phi_C}{\phi_{C,i}}; \qquad \phi_r = \frac{\phi_T - \phi_{T,f}}{\phi_{T,i} - \phi_{T,f}} \tag{3.12}$$

for the connected and total porosity respectively, which implies that the initial and final values

---

[7] See Section 2.1.

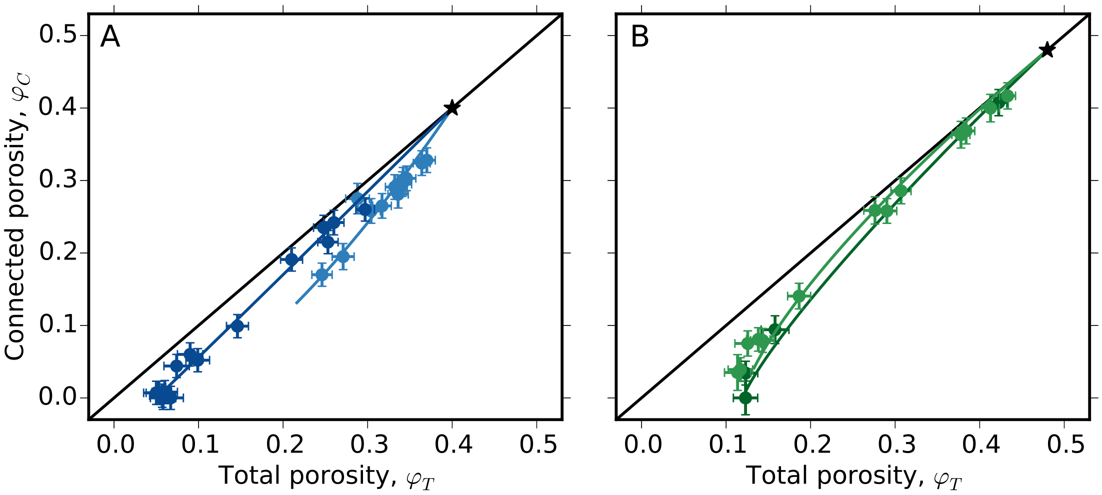

Figure 3.8: Trajectories in the total-connected porosity space with best-fit curves to the models (see text) for (A) the NIST glass and (B) the glass beads. The colour coding of the NIST glass data refers to the two viscosities investigated (see Figure 3.6A) and that of the glass beads data to the two particle size distributions investigated (see Figure 3.2B).

become 1 and 0, and a specific time of sintering τ_d can be defined by

$$\tau_d = \frac{t}{\lambda_d} \tag{3.13}$$

These definitions yield a master sintering curve for all viscous sintering of metastable single-phase melts (Figure 3.9).

3.3.2 STRENGTH RECOVERY

High temperature uniaxial compressive strength tests show that stress accumulation is mostly elastic and that macroscopic failure is preceded by a minor amount of strain hardening, highlighting the predominantly brittle nature of porous lava at such viscosity and high strain rate (Figure 3.10). Note that the defect-free NIST glass (pure melt; black curve in Figure 3.10A)

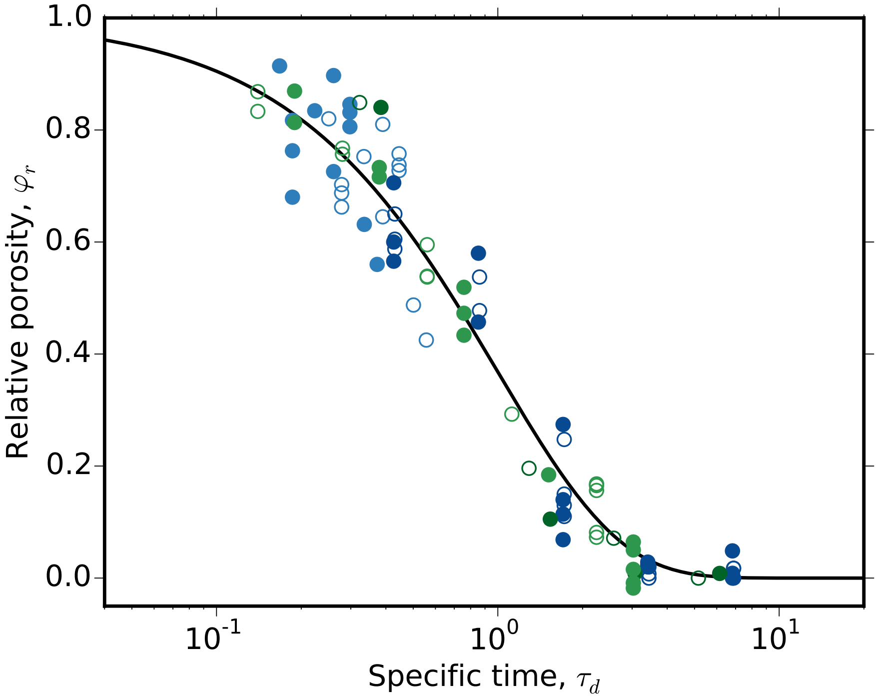

Figure 3.9: A master sintering curve for all the data presented in Figure 3.6. The filled symbols stand for the total porosity, whereas the unfilled ones for the connected porosity. The colour coding of the NIST glass data refers to the two viscosities investigated (see Figure 3.6A) and that of the glass beads data to the two particle size distributions investigated (see Figure 3.2B).

displays the most strain hardening prior to failure. One can observe that the stress-strain curves are very similar for both the sintered NIST glasses and sintered glass beads, suggesting that the microstructure of the porous network is not a first-order control during deformation and therefore less relevant. Sintering and densification result in strength recovery (*i.e.*, when the sintering time approaches λ_s, the strength of single-phase, defect-free melt (glass) is recovered). This result is expressed by the UCS (peak stress at failure; here measured at 10^{-3} s^{-1}). I observe that the UCS drastically increases with sintering time and thus decreases non-linearly with total porosity (Figure 3.11).

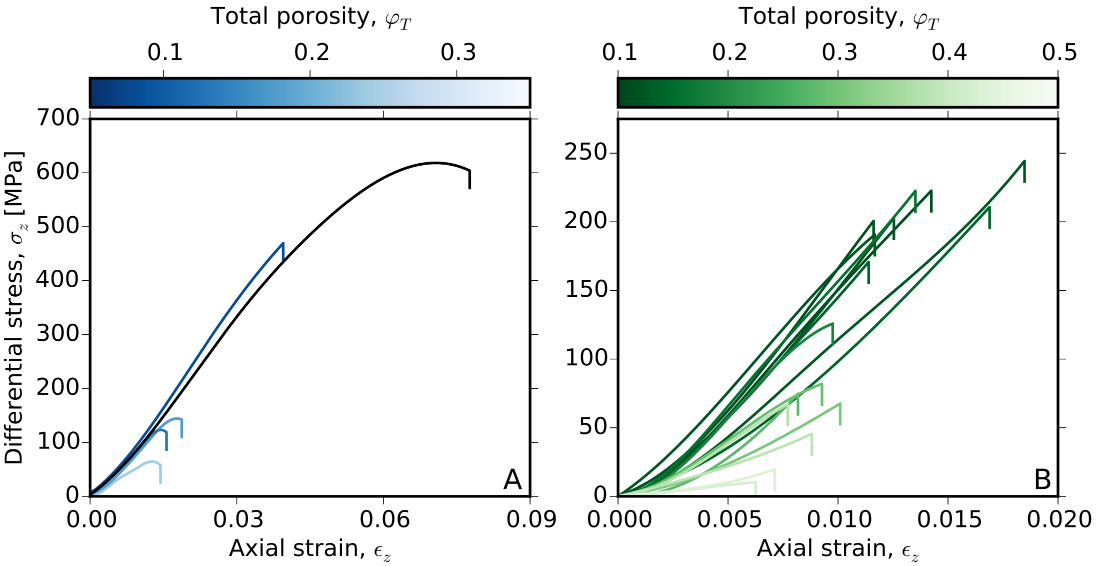

Figure 3.10: Micromechanics during sintering. The differential stress (*i.e.*, the axial stress) and axial strain resulting from strength tests performed at a constant strain rate of 10^{-3} s^{-1} for sintered samples of (A) NIST glass and (B) glass beads. The black line in (A) represents the stress-strain curve for the defect-free NIST glass.

As the porous structure of my medium mainly consists of pores (instead of cracks), I tested the applicability of the pore-emanating crack model to constrain the UCS results [Sammis & Ashby, 1986]. Zhu et al. [2011] provide an analytical approximation for the pore-emanating crack model as follows

$$\sigma_P = \frac{1.325 K_{Ic}}{\phi^{0.414}\sqrt{\pi r_{pores}}} \tag{3.14}$$

where σ_P is a compressive strength, r_{pores} the average radius of the pores and K_{Ic} is the fracture toughness or the critical stress intensity factor of glass through which a fracture needs to propagate to achieve complete failure. Note that fractures propagate by the conversion of strain energy to fracture surface energy; here, viscous dissipation of strain energy above the calorimetric glass transition is negligible, as the viscosity and strain rate are high: relaxation

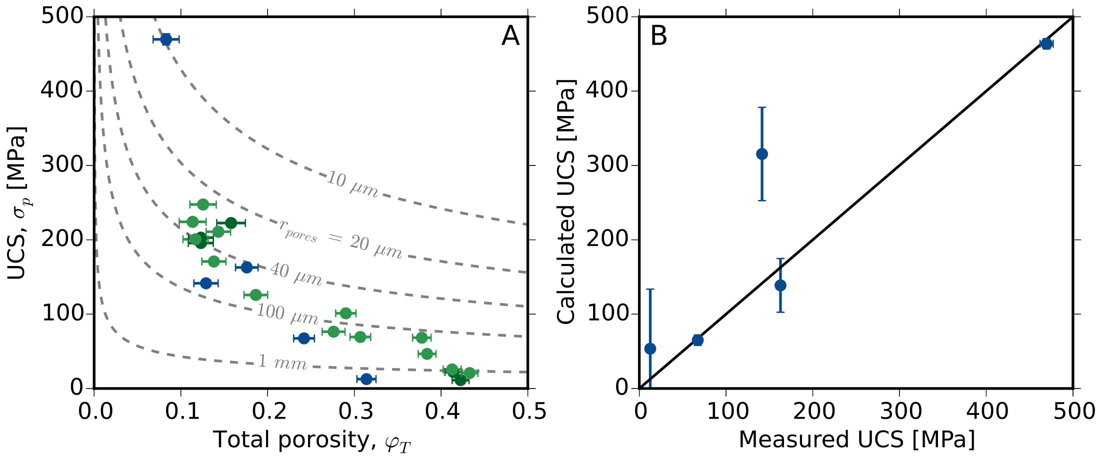

Figure 3.11: Strength recovery during sintering. (A) Uniaxial Compressive Strength (UCS) as measured by the peak stress at failure. Displayed are predicted isopore lines for different radii from which cracks initiate in the pore-emanating crack model [Sammis & Ashby, 1986; Zhu et al., 2011]. (B) The correlation between the UCS measured and the UCS predicted by the pore-emanating crack model for pore sizes measured in similarly sintered samples (see Figure 3.5A). The colour coding of the NIST glass data refers to the two viscosities investigated (see Figure 3.6A) and that of the glass beads data to the two particle size distributions investigated (see Figure 3.2B).

would require >100 s but the strength tests are performed in ≪100 s. This ensures deformation in a purely brittle regime. Combining measured porosities and estimated values of K_{Ic} for intact, defect-free borosilicate glass of a similar composition [Wiederhorn, 1969] to the NIST glass of ~0.7 MPa $m^{1/2}$, I can approximate the relationship between the pore radius r_{pores} and compressive strength using Equation 3.14 (see grey dashed lines in Figure 3.11A). This modelled relationship agrees with my experimental data (Figure 3.11B; NIST glass data only), as poorly-sintered samples with a high fraction of relatively large (~1 mm) pores have a compressive strength appropriate to their pore size; similarly, highly-sintered samples with a low fraction of relatively small (100 μm) pores have a compressive strength comparable to the modelled strength. This comparative analysis suggests that the pore-emanating crack model is wholly applicable to the strength of bubbly magma as a function of pore fraction and size at the porosities investigated here.

3.3.3 ELASTICITY RECOVERY

I tracked two elastic moduli during sintering: (1) the P-wave modulus $\mathcal{M}$ measured statically[8] and (2) the Young's modulus or tensile modulus E measured dynamically (*i.e.*, during elastic loading of the samples). The P-wave modulus is defined as

$$\mathcal{M} = \varrho_{bulk} v_P^2 \tag{3.15}$$

where v_P is the P-wave velocity, and the Young's modulus is given by the linear slope of the stress-strain curve during elastic deformation.

I observe that the total porosity is linearly proportional to the inverse of the measured ultrasonic P-wave velocity. Therefore, the P-wave modulus is also linearly, inversely proportional to total porosity (Figure 3.12) until the granular threshold value [Nur et al., 1998]. This critical porosity threshold is constrained here to a value of ~0.33 for the NIST glass; that is, the porosity at which the solid phase of the material is no longer load bearing and the bulk material behaves in a granular manner at low loads [Nur et al., 1998]. This relationship is well-established and suggests that the progressive sintering of fragments consistently densifies the material to below the theoretical critical porosity. The porosity range of the initial starting material is above the threshold, as it is granular. A simple linear regression may describe the trends observed as follows

$$\mathcal{M} = \mathcal{M}_0 - b_M \phi_T \tag{3.16}$$

---

[8] See Section 3.2.3.

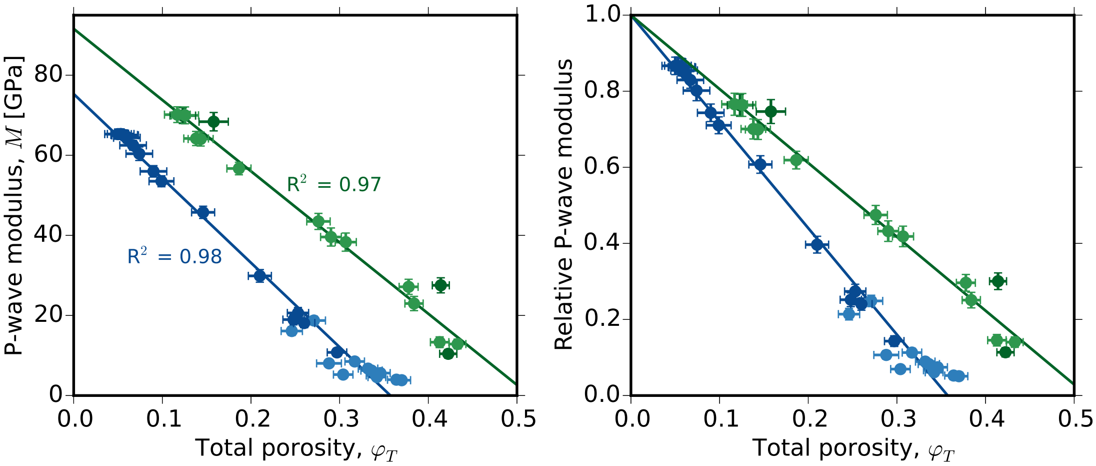

Figure 3.12: The effect of the total porosity on (A) the P-wave modulus and (B) the relative P-wave modulus, during sintering. The solid lines are the best-fits to the data using Equation 3.16. The colour coding of the NIST glass data refers to the two viscosities investigated (see Figure 3.6A) and that of the glass beads data to the two particle size distributions investigated (see Figure 3.2B).

for which M_0 is the P-wave modulus of the pure glass (*i.e.*, the value at $\varphi_T = 0$) and b_M the slope. The difference between the two materials used here; that is, the distance between the two best-fit lines shown in Figure 3.12A, corresponds to (1) the difference in P-wave modulus of the pore-free, dense specimens and (2) differences in the pore microstructure associated with particle packing and angularity. The first difference serves to modify M_0 whereas the second difference serves to modify b_M. This first difference is, in turn, controlled by the difference in glass density between the NIST glass (2375 kg m^{-3}) and the glass beads (2755 kg m^{-3}). The second difference is further illustrated by normalising the P-wave modulus by its fitted glass value (Figure 3.12B; relative P-wave modulus).

In the same manner as for the UCS[9], the Young's modulus shows a non-linear trend with total porosity (Figure 3.13). Both materials tend to recover their glass value at zero porosity.

---

[9] See Section 3.3.2.

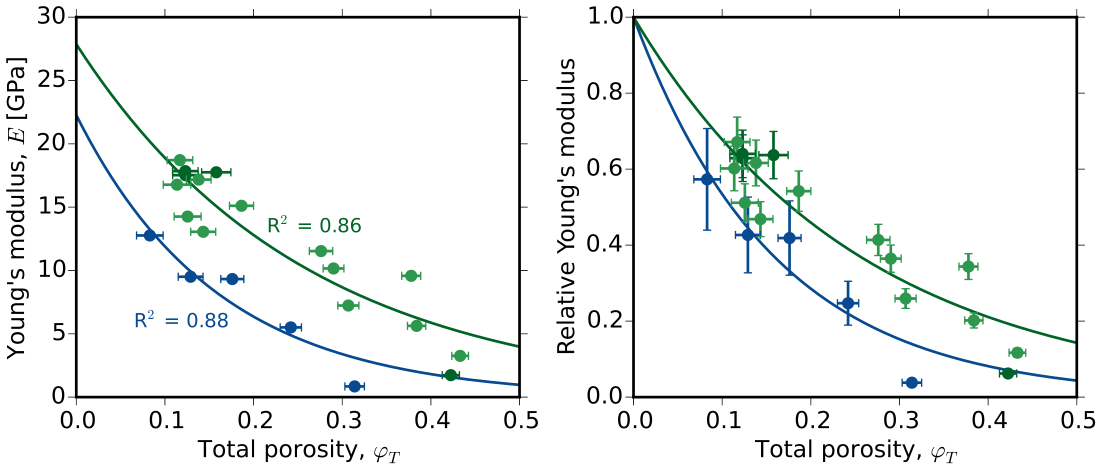

Figure 3.13: The effect of total porosity on (A) Young's modulus and (B) the relative Young's modulus, during sintering. The solid lines are the best-fits to the data using Equation 3.17. The colour coding of the NIST glass data refers to the two viscosities investigated (see Figure 3.6A) and that of the glass beads data to the two particle size distributions investigated (see Figure 3.2B).

An empirical relationship for the effect of porosity on Young's modulus of polycrystalline refractory materials and used in the field of rock mechanics is given by Spriggs [1961]

$$E = E_0 \exp\left(-b_E \phi_T\right) \tag{3.17}$$

for which E_0 is the non-porous Young's modulus and b_E an empirical constant. Using Equation 3.17 the data can be fitted by least square analysis, which shows that it is well-encompassed by this model (Figure 3.13A). As for the P-wave modulus, I see that the difference in trends is controlled by the difference in the non-porous elastic moduli of the specimens, which is likely due to the difference in glass density. Similarly, when normalising the Young's modulus by its fitted glass value (Figure 3.13B; relative Young's modulus), a difference remains and may be again inferred from differences in microstructure of the porous networks.

3.4 IMPLICATIONS FOR MAGMAS

The results presented in this study show that surface tension is capable of sintering ash particles and densifying porous lavas. Limitations in my experiments remain however as, in nature, sintering at low pressures in conduits may be accelerated if volatiles are resorbed into the melt, locally lowering the viscosity [Hess & Dingwell, 1996] and facilitating neck formation. However, sintering in surficial deposits, such as ignimbrites, may occur in the presence of air, which has a low solubility in silicate melts and is therefore not a significant viscosity-forcing factor [Castro, pers. comm.]. Additionally stress, whether compressive or tensional, can contribute to the total stress forcing densification. The results nonetheless demonstrate the near-static limiting conditions under which these processes can operate and may help provide a basic constraint on condition of sintering and densification of eruptive products in nature.

3.4.1 PLUG DENSIFICATION AND STIFFENING

Sintering and densification may be important processes occurring during lava dome extrusion. The porosity of lava domes varies widely (0–80 %; Castro & Cashman [1999]) and the lava commonly undergoes cycles of fracture and subsequent healing with or without the presence of tuffisite ash fragments [Tuffen & Dingwell, 2005; Kolzenburg et al., 2012]. During magma fragmentation, the fragments, which are not ejected from the shallow conduit, will sinter, heal and recover strength. Although my experiments only considered uniaxial compressive stress (neglecting confining stress, which accelerates compaction and pore pressurisation but counteracts dilatation), application of the aforementioned sintering timescale relationship suggests that healing is indeed very rapid (*e.g.*, minutes to hours) for crystal-free melts, as speculated by Kolzenburg et al. [2012], who were dealing with crystal-rich tuffisites which relax at a presumably lower rate. I note that even at surficial stress conditions a significant strength recovery can be achieved within the initial 15 % densification. Magmastatic stress and differential stress from magma ascent, which are greater than the stress imparted by surface tension, will accelerate this process. Thus the strength of a lava dome plugging a conduit should be seen as transient and requires knowledge of the porous network in real time if we wish to accurately constrain the eruption style [*e.g.*, Edmonds & Herd, 2007].

3.4.2 VOLCANIC ASH SINTERING IN RHEOMORPHIC FLOWS

The description of sintering in natural volcanic settings is typically referred to as welding and only occasionally is the term "sintering" used to describe the low-grade end-member of a welding continuum [Wilson & Hildreth, 2003]. Grunder & Russell [2005] suggest that, in fact, welding only applies to sintering that is coupled with flattening, compaction or stretching of pyroclasts. In the ceramics and glass science literature the description of sintering refers to the entire continuum and encompasses the diffusive and viscous components depending on the material state.

Most volcanic ash is dominantly composed of glass and so any scenario where volcanic ash is deposited close to or above the glass transition interval or where ash is subjected to a trajectory of reheating above the glass transition interval will result in a degree of viscous sintering dependent on the ratio of melt drop radius and surface tension (*e.g.*, Equation 3.7). Pervasive ductile deformation structures in so-called welded ignimbrites deposited from pyroclastic density currents are interpreted to result from the continued shear stress imposed by flow of the overlying mass on viscously deformable lava-like flows [Branney & Kokelaar, 1992; Manley, 1995]. The bed-load suspended in the pyroclastic density currents, which sinter upon deposition, is estimated to range between very fine ash (μm) and blocks (cm–m). Therefore, understanding of the particle size influence is critical for correctly estimating sintering timescales or temperatures of emplacement. The normalised density of such deposits has been used to rank the strain associated with sintering and compaction [Smith, 1960; Wilson & Hildreth, 2003; Quane & Russell, 2005]. Normalised densities for non-welded material ranges from 0.3–0.4 whereas foliated and welded vitrophyric material ranges from ~0.7–1.0 (welding intensity rank I–VI; Quane & Russell [2005]). Application of my modelled relationship provides a lower constraint of the timescale of the sintering interval over which porosity can be reduced to the values observed in the deposits under ambient pressure conditions; that is, neglecting the load of the overlying flowing mass. These data suggest that for a pyroclastic density current containing suspended fragments of super-cooled silicate liquid with long relaxation times, the sintering time upon deposition can be approximated by Equation 3.7. Some authors invoke a geometrical parameter to approximate the sintering fragments to spheres, which in cases of low-angularity particles may be more appropriate [*e.g.*, Scherer & Bachman, 1977]. Thus my considerations complement previous studies and provide detailed insights into the relationship between the particle size and the melt properties which should be incorporated into the rheological relationships developed for volcanic welding [*e.g.*, Quane et al., 2009].

If I consider a pyroclastic deposit in its entirety, an overburden stress of 10^5 Pa is predicted for a deposit ~10 m, which exceeds surface tension and thus induces compressive flattening and foliation during sintering [Russell & Quane, 2005]. However, densely welded ignimbrites commonly result from progressive aggradation from sustained density currents [Branney & Kokelaar, 1992] and therefore the overburden is an end-state and sintering, initiated at low axial stress and would be partially controlled by the processes I describe.

Prediction is very difficult, especially if it's about the future.

Niels Bohr

4

Material failure forecasting

Elastic waves are generated when materials fracture under given stress conditions. Their number and energy increase non-linearly, ending in a system-sized catastrophic failure event. Accelerating rates of geophysical signals (*e.g.*, seismicity and deformation) preceding large-scale dynamic failure can serve as proxies for damage accumulation in the Failure Forecast Method (FFM). Here I test the hypothesis that the style and mechanisms of deformation, and the accuracy of the FFM, are both tightly controlled by the degree of microstructural heterogeneity of the material under stress. I generate a suite of synthetic samples with variable heterogeneity, expressed by the total porosity. I experimentally demonstrate that the accuracy of failure prediction increases drastically with the degree of material heterogeneity. These results have significant implications in a broad range of material-based disciplines for which failure forecasting is of central importance. In particular, the FFM has been used with only variable success to forecast failure scenarios both in the field (volcanic eruptions and landslides) and in the laboratory (rock and magma failure). My results show that this variability may be explained, and the reliability and accuracy of forecast quantified significantly improved, by accounting for material heterogeneity as a first-order control on forecasting power.

4.1 DAMAGE ACCELERATION AND FAILURE

Most Earth materials exhibit significant structural heterogeneities. Common examples are local density fluctuations, pores, cracks and crystals [Alava et al., 2006]. The presence of these so-called Griffith flaws in materials provides sites of stress concentration where isolated cracks may nucleate favourably [Griffith, 1921] and their growth dynamics under subcritical loading may be strongly affected [*e.g.*, Petri et al., 1994; Ramos et al., 2013]. Ultimately, sustained microcrack initiation, multiplication and coalescence often results in a critical density of fractures whereby macroscopic rupture ensues. In this manner, fracturing in heterogeneous materials is pervasive prior to failure, as cracks propagate small distances between flaws and strain energy can be readily dissipated elastically [Paterson & Wong, 2005; Wong &

Baud, 2012]. In non-porous glasses, such elements of heterogeneity are lacking and the few crack nucleation sites available are typically nanoscopic in scale [Célarié et al., 2003; Bonamy et al., 2006]. Therefore, the crack propagation distance is relatively large and the strain energy stored must exceed the activation energy required for nucleation and propagation of fractures across the sample [Griffith, 1921]. In such cases, little or no strain energy is released prior to rupture and fracturing is localised rather than pervasive. Thus more homogeneous materials possess a great propensity for highly catastrophic failure through rapid, unstable crack propagation associated with few precursory signals [Alava et al., 2006].

In the Earth system, strain localisation and material failure yield threshold for natural disasters. At volcanoes the onset of an eruption is often preceded by an acceleration in seismicity originating from the fracturing of rocks and formation of a conduit [Kilburn, 2003; Smith et al., 2009]; likewise eruptive transitions to explosions are also preceded by such characteristic seismic patterns [De la Cruz-Reyna & Reyes-Dávila, 2001] that have been experimentally demonstrated to originate from magma failure [Lavallée et al., 2008; Tuffen et al., 2008]. In the case of landslides, a similar acceleration in seismicity may also be observed [*e.g.*, Fukuzono, 1985; Kilburn & Petley, 2003]. Thus empirical mechanistic models have been developed to describe the stress and strain rate extant upon failure of both porous rocks [Paterson & Wong, 2005] and magmatic suspensions. Material deformation and failure is generally accompanied by accelerating precursory signals [*e.g.*, Mogi, 1962; Lockner & Byerlee, 1977; Lockner, 1993; Petri et al., 1994; Davidsen et al., 2007; Ramos et al., 2013]. This acceleration represents the basis for the application of time-to-failure forecasting models [Fukuzono, 1985; Voight, 1988; Cornelius & Voight, 1994; Main, 1999]. During rock deformation, microcracking releases acoustic emissions prior to macroscopic failure [Lockner, 1993]. Their temporal, spatial and size distribution follow a power law [Voight, 1989; Petri et al., 1994; Main, 2000; Davidsen et al., 2007], which is also observed in tectonic earthquake aftershock activity [Shaw, 1993; Utsu et al., 1995; Shcherbakov et al., 2004] as well as in seismic precursors to volcanic eruptions [Voight, 1988; Main, 1999; Kilburn & Voight, 1998]. Nevertheless, the wide range of materials in nature and especially the degree of material heterogeneity (at all scales) challenges our understanding of precursory signals leading to natural disasters [Sornette, 2002].

4.2 EXPERIMENTAL METHODS

4.2.1 SAMPLE PREPARATION

The suite of samples was fabricated by viscous sintering under no external applied stress[1]. I used industrial soda-lime silica beads (Spheriglass® A-glass microspheres 1922 and 2530, Potters Industries Inc.) with well-constrained chemical and physical properties such as the calorimetric glass transition interval and the viscosity-temperature dependence. This material is also chemically stable and does not crystallise or degas at the experimental conditions. I systematically packed glass beads in alumina ceramic crucibles (44 mm diameter and 75 mm height) and heated them at 10 $\mathrm{K\,min^{-1}}$ to an isotherm above the glass transition at which the melt viscosity is 2.09×10^8 Pa s. Viscous sintering took place during dwells of 1 to 32 hours and the samples were cooled down at a slower rate of $\sim$5 $\mathrm{K\,min^{-1}}$ to avoid induced thermal cracks. The densified products were finally drilled out from the crucibles to sample cores of 25 mm diameter by 50 mm height. The total porosity in the suite of cores was calculated from the density of the bulk sample and the powdered glass density as measured after sintering.

---

[1] See section 3.2.2

4.2.2 SAMPLE CHARACTERISATION

Connected and total porosity, and ultrasonic wave velocities of the porous glass samples were characterised using the methods described in section 3.2.3. Accordingly, a series of UCS tests was performed in a high load, high temperature uniaxial press[2] equipped with a split furnace surrounding the pistons (in order to simulate magma deformation in the upper volcanic conduit) at a constant strain rate of $10^{-3}\,\mathrm{s}^{-1}$ and a temperature of $\sim$825 K. Because the samples are only composed of two phases, porosity strongly controls the subcritical dynamics during brittle deformation. Similarly to the critical point analogy[3] [Davies, 1992; Alava et al., 2006], I define a sample "order parameter" Q based on the normalised difference between the areas of both phases in Figure 3.5 (which would directly provide a quantitative metric for structural heterogeneity in porous glass samples)

$$Q = \left| \frac{A_{white} - A_{black}}{A_{total}} \right| \tag{4.1}$$

where A_{white}, A_{black} and A_{total} and the areas described by the glass matrix and the pores, and the total area respectively. Since the field is boolean (*i.e.*, a change of dimension does not add to the complexity), I can interconvert between area and volume, such that Equation 4.1 becomes

$$Q = \left| \frac{V_{matrix} - V_{pores}}{V_{total}} \right| \tag{4.2}$$

---

[2] See schematic in Figure 3.4B

[3] During the approach to a critical point or the in the neighbourhood of a critical point, a system is appropriately described on lengthscales on the order of the correlation length (*e.g.*, the size of the largest crack for a specimen under subcritical loading), since details on smaller lengthscales are irrelevant to the overall behaviour.

By injecting Equations 3.3 and 3.4 into Equation 4.2 I further get

$$Q = \left| \frac{\left(1 - \varphi_T\right) V_{total} - \varphi_T V_{total}}{V_{total}} \right| = \left|1 - 2\varphi_T\right| \tag{4.3}$$

It follows that at $\varphi_T = 0$ (pore-free) or $\varphi_T = 1$ (no solid phase), $Q = 1$ (*i.e.*, perfect order), and that at $\varphi_T = 0.5$, $Q = 0$ (*i.e.*, maximum disorder). The heterogeneity index (or disorder index) is thus straightforwardly calculated from $H = 1 - Q$.

4.2.3 Microseismic data acquisition

During deformation at high temperature in the uniaxial press, the cooler ends of the pistons were equipped with two (one on each end) Acoustic Emission (AE)[4] broadband transducers of 125 kHz central frequency. The pistons were thus used as waveguides for AEs released during microfracturing processes and catastrophic sample failure. The AE signal was transferred using buffered 40 dB pre-amplifier to a data acquisition system (Richter system, Applied Seismology Consultants), which recorded AE voltage data continuously (12-bit A/D full-waveform resolution) at a sampling rate of 20 MHz. From these continuous streams, AE event onsets were (1) triggered using a standard STA/LTA (Short-Term Average over Long-Term Average) detector [Baer & Kradolfer, 1987] and (2) automatically picked using an adaptation of the standard autoregressive-Akaike-Information-Criterion (AR-AIC) picker [*e.g.*, Sleeman & van Eck, 1999; Leonard, 2000; Zhang et al., 2003].

In seismology, event detection[5] is of foremost importance since seismological surveillance of the globe implies the storage of huge quantities of informations. Detection algorithms

---

[4] AEs are high-frequency (in the range of 1 kHz to 1 MHz), transient stress waves generated by release of accumulated elastic energy during mechanical loading of a material.

[5] Also known as “event triggering”.

have been developed and are all based on seismic onset characteristics: (a) the signal amplitude increases tremendously and (b) the main frequencies become those of the earthquake. In AE testing, event detection is commonly based on one of these characteristics and made by setting a set of defined parameters, such as a simple voltage threshold. However, other energy-based algorithms such as the STA/LTA method are widely used in seismology to characterise the evolution of the local signal-to-noise ratio. They often involve the computation of the signal envelope

$$E_s\left(t\right) = \sqrt{s\left(t\right)^2 \bar{s}\left(t\right)^2} \tag{4.4}$$

where s and $\bar{s}$ are the signal and its Hilbert transform. During the arrival of a wave, the signal envelope average at short term (STA: approximation of the local signal) over the its average at longer term (LTA: approximation of the global noise) varies significantly. Thus, when a threshold fixed *a priori* is exceed, detection ensues. For my AE records, I found that setting the STA and LTA windows to 1 and 20 ms respectively, and the threshold to 2 yielded the best results.

Accordingly, event picking is also a critical component of signal processing in seismology. Modelling the signal as an autoregressive process is an usual approach for onset time determination. Akaike [1974] was the first to show that a time series could be divided into locally stationary segments, each of which representing an autoregressive process, and to define a mathematical criterion to solve for the separation point between two segments. For a time series $x\left[1, N\right]$ for which N is the total number of samples, the Akaike Information Criterion (AIC) is given by

$$AIC\left[k\right] = k \ln\left(\mathrm{var}(x\left[1, k\right])\right) + \left(N - k - 1\right) \ln\left(\mathrm{var}(x\left[k+1, N\right])\right) \tag{4.5}$$

where k is the current sample index. The function compares the logarithm of the variance before and after the current sample. Since the variance measures the dispersion of the data around the mean, an important difference in dispersion occurs before and after the sample k in Equation 4.5 during the arrival of a seismic wave, such that its onset often corresponds to the minimum of the AIC function. In the case of AE the signal was de-noised prior to AIC computation.

Once triggering, P-wave picking and event selection have been performed, characteristics of each AE event are computed, such as the peak amplitude in dB and the energy in nJ (based on a resistance reference standard value of 10 kΩ). Altogether, this procedure permits the generation of pre-failure catalogues of AE events for each deformation experiment. These catalogues are further used as the basis for the application of the FFM.

4.3 Failure predictability

4.3.1 Models of acceleration

A great number of catastrophic events share similar characteristic accelerating trends in warning signals [Sornette, 2002] and are potentially describable via similar scaling laws [Bak et al., 2002; Davidsen et al., 2007]: rupture of engineering structures, natural catastrophes (such as great earthquakes, volcanic eruptions, landslides and avalanches), abrupt weather changes, some stock market crashes and even human parturition, amongst others. In many current models for precursory acceleration, the rate of seismic events $\dot{\omega}$ can be described by the Time-Reversed Omori Law (TROL) [Hirata, 1987; Shaw, 1993; Utsu et al., 1995; Shcherbakov et al., 2004]

$$\dot{\omega}\left(t\right) = k_{PL}\left(t_c - t\right)^{-p} \tag{4.6}$$

for which k_{PL} is a scaling parameter, p parameterises the rate of acceleration (in turn dependent on the dominant crack mechanism [Kilburn, 2003]) and t_c is the critical time (corresponding to the time of system-sized catastrophic failure). This critical point is defined by a mathematical singularity as the quantity $\dot{\omega}$ evolves toward infinity. Equation 4.6 is directly analogous to the approach to a critical point in a second-order phase transition for the correlation length (size of the largest cluster or in my case the largest growing crack)[6] as a function of temperature rather than time (also with a critical exponent analogous to p, which depends on the microscopic physics) [Main, 2000; Alava et al., 2006]. The TROL is of widespread interest as a forecasting tool and has been extensively applied to material failure phenomena [*e.g.*, Tokarev, 1971; Fukuzono, 1985; Voight, 1988; Cornelius & Voight, 1994; Kilburn & Voight, 1998; Main, 1999; De la Cruz-Reyna & Reyes-Dávila, 2001; Kilburn & Petley, 2003; Kilburn, 2003; Lavallée et al., 2008; Smith et al., 2009; Smith & Kilburn, 2010; Bell et al., 2011a, 2013]. The FFM is an empirical relationship relating the acceleration of a geophysical observable $\ddot{\omega}$ to its rate $\dot{\omega}$ under steady state conditions (stress or strain rate, temperature)

$$\ddot{\omega} = A\dot{\omega}^m \tag{4.7}$$

with $A \sim k_{PL}$ and $p = \frac{1}{m-1}$. In this context $\dot{\omega}$ can be applied to any accelerating signal whereupon after linearisation of the TROL, the FFM takes the following form

$$\dot{\omega}(t)^{-\frac{1}{p}} = k^{-\frac{1}{p}}(t_c - t) \tag{4.8}$$

---

[6] See Section 2.2.2.

In a volcanic context, p has been shown to decrease toward 1 as cracks grow [Kilburn, 2003]. Retrospective analyses of pre-eruptive seismic activity have thus commonly assumed that $p = 1$, which implies that the solution is straightforwardly found by means of a linear regression of the inverse rate with time. However, this approach may yield a biased and inaccurate solution [Bell et al., 2011b] because the FFM fails to account correctly for the true Poisson error structure of the data. Therefore, I apply the Maximum Likelihood (ML) method to the full point process, in order to provide (a) a more reliable estimate of the precision (random error) and (b) a more accurate solution, which reduces the potential for residual bias (systematic error) in forecasting the failure time [Bell et al., 2013]. Following Ogata [1983], the logarithm of the likelihood function L for the TROL takes a similar form to that of the modified Omori law for aftershock occurrence and is, in an interval (t_0, t_1), given by

$$\ln\left(L\right) = \sum_{i=1}^{N} \ln\left(k_{PL}\left(t_c - t_i\right)^{-p}\right) + \frac{k_{PL}}{1-p}\left(\left(t_c - t_1\right)^{1-p} - \left(t_c - t_0\right)^{1-p}\right) \tag{4.9}$$

for $p \neq 1$, and

$$\ln\left(L\right) = \sum_{i=1}^{N} \ln\left(k_{PL}\left(t_c - t_i\right)^{-1}\right) + k_{PL}\left(\ln\left(t_c - t_1\right) - \ln\left(t_c - t_0\right)\right) \tag{4.10}$$

for $p = 1$. The TROL is most commonly employed to describe the rate of pre-failure seismic events because it has a well-defined failure time. Other models have been proposed on theoretical or empirical grounds, including the exponential model [Lengliné et al., 2008; Bell et al., 2011a; Bell & Kilburn, 2012; Kilburn, 2012]

$$\dot{\omega}\left(t\right) = k_{Exp} \exp\left(qt\right) \tag{4.11}$$

with k_{Exp} the pre-exponential scaling parameter and q the rate constant; however, the failure time is not defined by the dynamics underlying the exponential model and failure forecasts using this model must be based on other metrics. In this case the log-likelihood of the exponential model is, in an interval (t_0, t_1), defined by

$$\ln(L) = q\sum_{i=1}^{N} t_i + N\ln\left(k_{Exp}\right) - \frac{k_{Exp}}{q}\left(\exp\left(qt_1\right) - \exp\left(qt_0\right)\right) \tag{4.12}$$

A very simple, non-realistic constant rate model can also be used, such that

$$\dot{\omega}(t) = c \tag{4.13}$$

for which c is the rate constant. The resultant log-likelihood function, in an interval (t_0, t_1), reads

$$\ln(L) = N\ln(c) - c\left(t_1 - t_0\right) \tag{4.14}$$

4.3.2 TIME-TO-FAILURE ANALYSIS

I experimentally test the hypothesis that the accuracy of failure forecasting improves as a function of material heterogeneity using samples of variable quenched disorder, generated by the total porosity (0–0.45) available during the synthesis[7]. This style of heterogeneity also provides a direct analogue for porous magma fragmentation. Specifically I investigate the failure of variably porous silicate liquids undergoing the glass transition. Uniaxial compression of these porous materials was carried out at ~825 K in the elastic, brittle regime by imposing a strain rate of $10^{-3}\ \mathrm{s}^{-1}$ while monitoring AEs during deformation up to bulk failure.

---

[7] See Section 3.3.

ENERGY CONSIDERATIONS

During elastic loading, the energy budget of a specimen is significantly changing, as it is put out of the initial state equilibrium by pushing towards the macroscopic failure envelope. The instability, which is described by the critical point or critical time t_c, is reached upon failure. The strain potential energy stored during deformation is progressively released by brittle fracturing, which implies the conversion of strain energy into dominantly free surface energy (crack opening and propagation), seismic or acoustic energy (mechanical waves), and minor amounts of heat and light. AE energy is therefore a proxy for the mechanical energy dissipated by crack formation. The interplay between stored and released energy controls the overall energy balance and is investigated hereafter. Note that the AE energy computed here is surely an underestimation of the full energy released for multiple reasons: (a) as just mentioned, the stored energy is not entirely converted into acoustic waves; (b) the AE energy computed (although gain-corrected) does not represent the energy released at the source because of path effects in the sample and in the pistons; and (c) the AE signal is not recorded in joules directly, which implies that there is an inherent calibration error when computing the energy of a signal.

The calculated AE energy release rate during deformation and failure shows typical hyperbolic (power law) acceleration underlying the definition of Equation 4.6 (Figure 4.1A). Drastic fracture propagation upon macroscopic failure releases the highest rate of AE energy, and this rate decreases systematically with increasing heterogeneity (Figure 4.1B). Nevertheless, AE energy cannot be used in a failure forecasting perspective based on the ML method[8] since a point process approach has of yet not been developed and is potentially not trivial

---

[8] See Section 4.3.1.

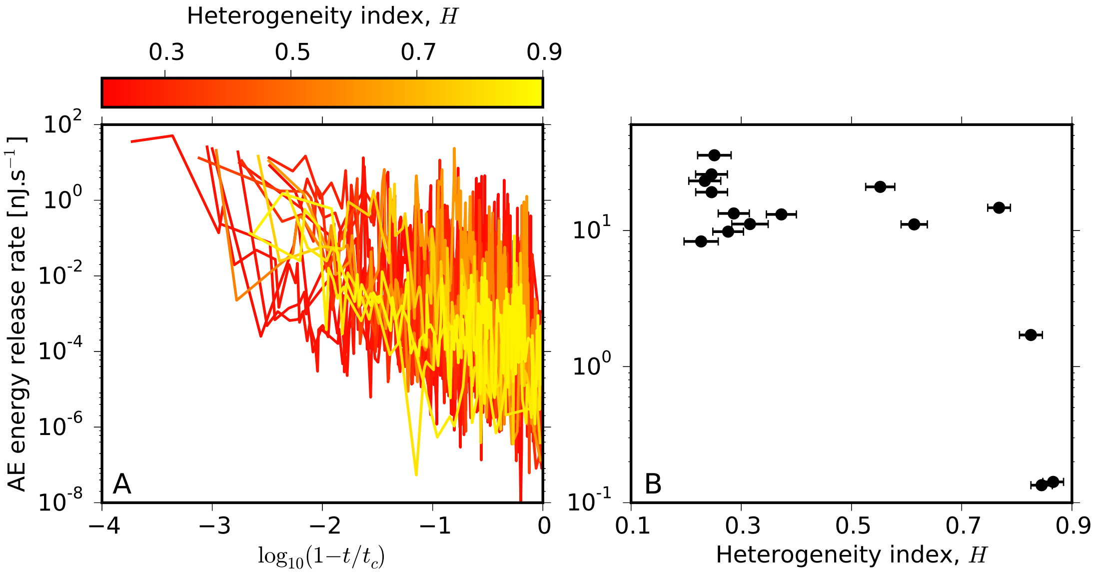

Figure 4.1: Rate of acoustic energy released from porous glasses during deformation and failure (A) for the full time series and (B) at failure. The logarithmic space used in (A) is to test the adequacy of a power law form of acceleration towards failure (see text). The data in (A) are colour-coded from low to high heterogeneity samples.

[Bell, pers. comm.].

Damage accumulation relates directly to subcritical crack dynamics[9] and the AE energy provides a good indication of fracture processes occurring inside a specimen. Under constant stress, Equation 2.25 predicts the acceleration of crack length l_c and reduces to an equation of the form [Das & Scholz, 1981; Main, 1999]

$$l_c\left(t\right) = l_{c,i}\left(1 - \frac{t}{t_c}\right)^{\frac{2}{2-n}} \tag{4.15}$$

when $n > 2$, with $l_{c,i}$ the crack length at $t = 0$. As described in Section 4.3.1, one can directly observe that Equation 4.15 has a similar form to Equation 4.6 but with a different power law

---

[9] See Section 2.2.2.

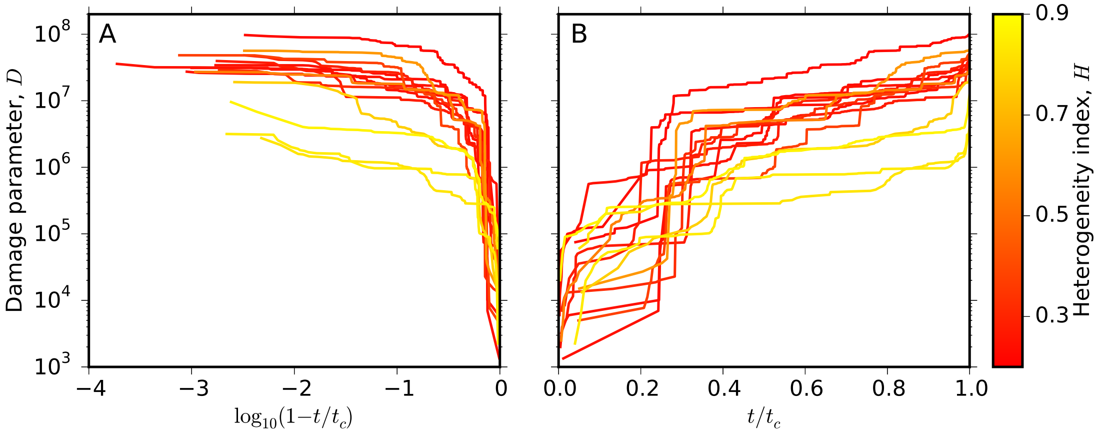

Figure 4.2: Damage accumulation in porous glasses during deformation and failure plotted in (A) a log-log and (B) a semi-log space, and colour-coded from low to high heterogeneity samples. The plotting space used in (A) is to test the adequacy of a hyperbolic trend towards failure, whereas the plotting space in (B) is to test an exponential form (see text).

exponent. This link was formally made between subcritical crack growth and the FFM by Main [1999]. When the stress is increasing linearly, the resultant acceleration takes a similar form [Main, 2000] with a shorter acceleration for a given value of n.

A damage parameter D is directly calculated from the decibel amplitude A_{dB} of the AE events [Cox & Meredith, 1993]

$$D = \sum_{i=i}^{N} 10^{\frac{3A_{dB}}{40}} \tag{4.16}$$

The accumulation of damage displays a supra-exponential acceleration for my experiments (Figure 4.2). Such damage accumulation is not predicted best by the power law formulation for subcritical crack growth derived in Equation 4.15 (Figure 4.2A). However, when it is plotted against $\frac{t}{t_c}$ in a linear space instead of $1 - \frac{t}{t_c}$ in a logarithmic space, the resultant trends appear close to linear (Figure 4.2B). Such evolution can be derived by setting $n = 2$ in Equa-

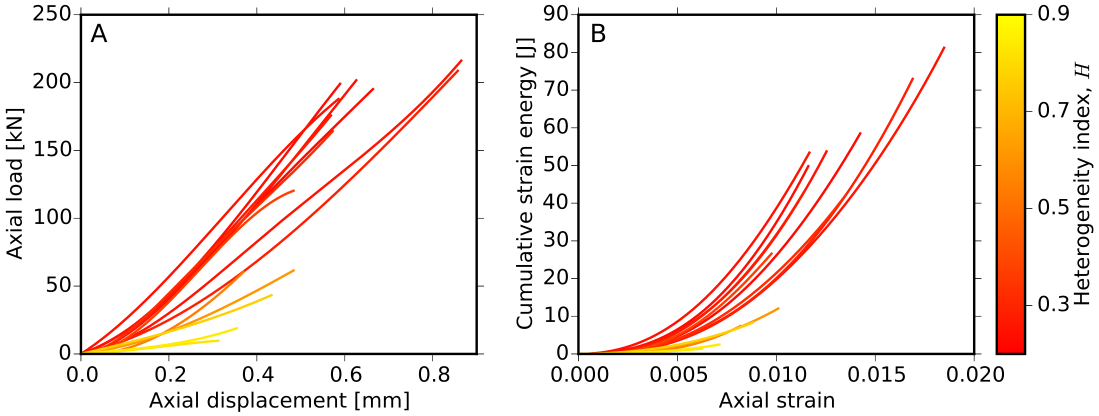

Figure 4.3: Mechanical response and strain energy of porous glasses during deformation and failure. (A) Axial load against axial displacement (data from Figure 3.3.2B). (B) Cumulative strain energy stored as estimated by the area under the curves in (A). All lines are colour-coded from low to high heterogeneity samples.

tion 2.25 and the subcritical crack length can be shown to be [Ojala et al., 2003]

$$l_c\left(t\right) = l_{c,i} \exp\left(\nu \frac{t}{t_c}\right) \tag{4.17}$$

where ν is an empirical constant. Nevertheless, damage accumulation can also not be used in a failure forecasting perspective for the same reasons discussed above; Equations 4.15 and 4.17 are therefore disregarded as potential forecasting tools.

I use the data presented in Section 3.3.2 to calculate the strain energy stored during deformation, here recast as axial force against axial displacement (Figure 4.3A). The strain energy is simply estimated by the integrated area under the force-displacement curve (Figure 4.3B). I observe non-linear trends for all samples, which can be decomposed into (1) an incurved onset at low axial strain corresponding to some reduction in pore volume (*i.e.*, much of the strain is accommodated elastically), (2) a linear portion during which the strain is stored into the glass

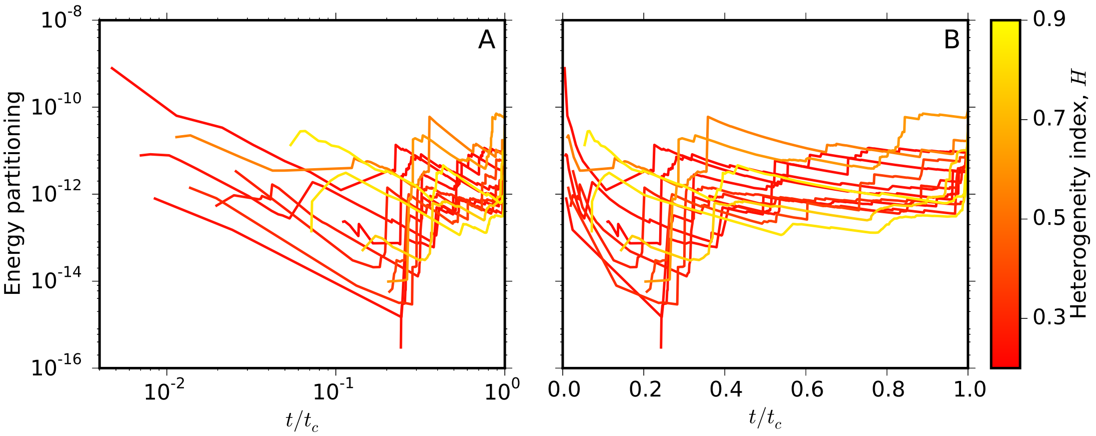

Figure 4.4: Acoustic-mechanic response of porous glasses during deformation and failure. Energy partitioning (as calculated from ratio of cumulative acoustic over cumulative strain energy) plotted in (A) a log-log and (B) a semi-log space, and colour-coded from low to high heterogeneity samples.

matrix, and (3) a peak at which macroscopic failure occurs and the energy is released. The stress drops are not shown in Figure 4.3 but they display full energy release for all samples, which implies that the remaining strain energy stored (*i.e.*, not released during microcracking events) is completely consumed upon fragmentation.

The seismo-mechanical coupling can further be formally assessed by looking at the energy partitioning during deformation and failure. I compute the ratio between the acoustic energy released and the mechanical energy stored, and track it over the deformation process (Figure 4.4). A general realisation is that the trends display two stages as (1) the ratio decreases drastically with time (*i.e.*, more energy is stored than it is released, relatively speaking) and (2) the ratio increases in increments (*i.e.*, more energy is released than it is stored, relatively speaking). The first stage quantifies the strain energy partition into aseismic processes occurring during the onset of deformation (interpreted as pore volume reduction or even pore closure) while the second stage quantifies the strain energy partition into seismic processes.

Retrospective failure forecasting

I applied the TROL to catalogues of acoustic events in order to retrospectively forecast failure. Equation 4.6 has three free parameters (k_{PL}, p and t_c) to adjust since they are not known *a priori*. The ML method has been shown to provide statistically stable and repeatable estimates of these parameters [Bell et al., 2013]. Additionally, this method uses the timings of individual AE events rather than event rates determined in equally spaced bins (as is commonly the case when applying the standard FFM). The ML solution is found by minimising the negative log-likelihood function (see Equations 4.9 and 4.10) using a downhill simplex algorithm. The forecasting window was restricted to 90% of the known failure time. Uncertainties on the fitted parameters require prior constraint to be reliably computed such that this precludes the estimation of meaningful error bars on the forecasted failure times. I define the forecast error δ as the absolute difference between the predicted failure time $t_{c,f}$ and the experimental failure time $t_{c,e}$ normalised by the deformation time, namely

$$\delta = \frac{t_{c,p} - t_{c,e}}{t_{c,e}} = \frac{t_{c,p}}{t_{c,e}} - 1 \tag{4.18}$$

since the deformation time corresponds to the experimental failure time. It follows that when $t_{c,p} = t_{c,e}$, $\delta = 0$ (*i.e.*, failure time perfectly resolved); when $t_{c,p} < t_{c,e}$, $\delta < 0$ (*i.e.*, early forecast); and when $t_{c,p} > t_{c,e}$, $\delta > 0$ (*i.e.*, late forecast).

I hereafter show three experimental examples of samples with a range of heterogeneity between 0.25 and 0.77. The TROL and exponential models (Equations 4.6 and 4.11) are illustrated in cumulative form to compare against the total number of AE events

$$\Omega\left(t\right) = \frac{k_{PL}}{1-p}\left(\left(t_c - t\right)^{1-p} - \left(t_c - t_0\right)^{1-p}\right) \tag{4.19}$$

for the TROL, and

$$\Omega\left(t\right) = \frac{k_{Exp}}{q}\left(\exp\left(qt\right) - \exp\left(qt_0\right)\right) \tag{4.20}$$

for the exponential model. Prospective forecasting at 90% of the raw data using the TROL and the exponential models shows that they are almost indistinguishable for heterogeneities of 25% and 37% (Figures 4.5A and 4.6A), unlike for 77% where they start to diverge from each other (Figure 4.7A). In the latter a more pronounced singularity as time tends towards the failure time (power law asymptote) is observed, whereas in the formers this singularity is seemingly not present or has not been reached. Henceforth, the retrospective ML TROL fits the data very well for any degree of heterogeneity. By means of a statistical tool called the Bayesian Criterion Information (BIC)[10], the discrepancy between the ML TROL and exponential fit may be picked apart. This is illustrated by the ΔBIC, which almost never favours the TROL over the exponential model (*i.e.*, $\Delta BIC > 0$) for $H = 0.25$ and $H = 0.37$ (Figures 4.5B, 4.6B), whilst starting to slightly prefer the TROL (*i.e.*, $\Delta BIC < 0$) for $H = 0.77$ (Figure 4.7B). However, the results indicate that the AEs released during the first stages of deformation generally follow an exponential trend. It is known from fracture mechanics that exponential trends are controlled by the activation of an increasing number of cracks, whereas hyperbolic trends are determined by the coalescence of major cracks [*e.g.*, Kilburn, 2003, 2012].

---

[10] For a comprehensive definition and analysis, see Section 4.3.3.

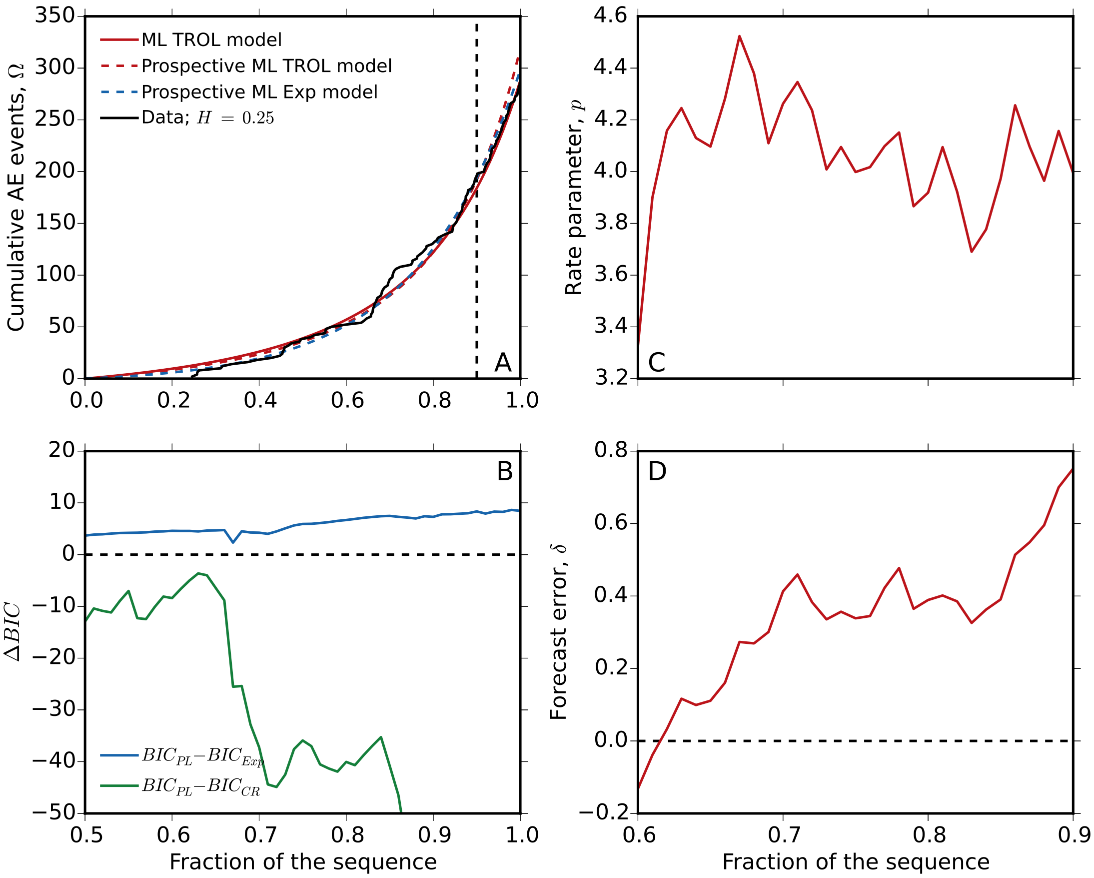

Figure 4.5: Maximum Likelihood failure forecasting for a sample with $H = 0.25$. (A) Cumulative number of AE events (solid black line), retrospective ML TROL model (solid red line), and prospective ML TROL (dashed red line) and exponential model (dashed blue line) at 90% of the failure time. The vertical dashed line indicates the cut-off for prospective forecasting. (B) ΔBIC for TROL–exponential (solid blue line) and TROL–constant rate (solid green line). $\Delta BIC = 0$ is indicated as a horizontal dashed black line. (C) ML estimate of the rate parameter for the TROL model. (D) Forecast error as calculated from the ML estimate of the failure time.

The fact that the power law singularity is not present for low and medium heterogeneity samples implies that the TROL almost always predict a rate parameter that has not yet reached a value around 1 (Figures 4.5C and 4.6C) and a failure time relatively far from the observed one (Figures 4.5D and 4.6D) (which remains true while moving along the data se-

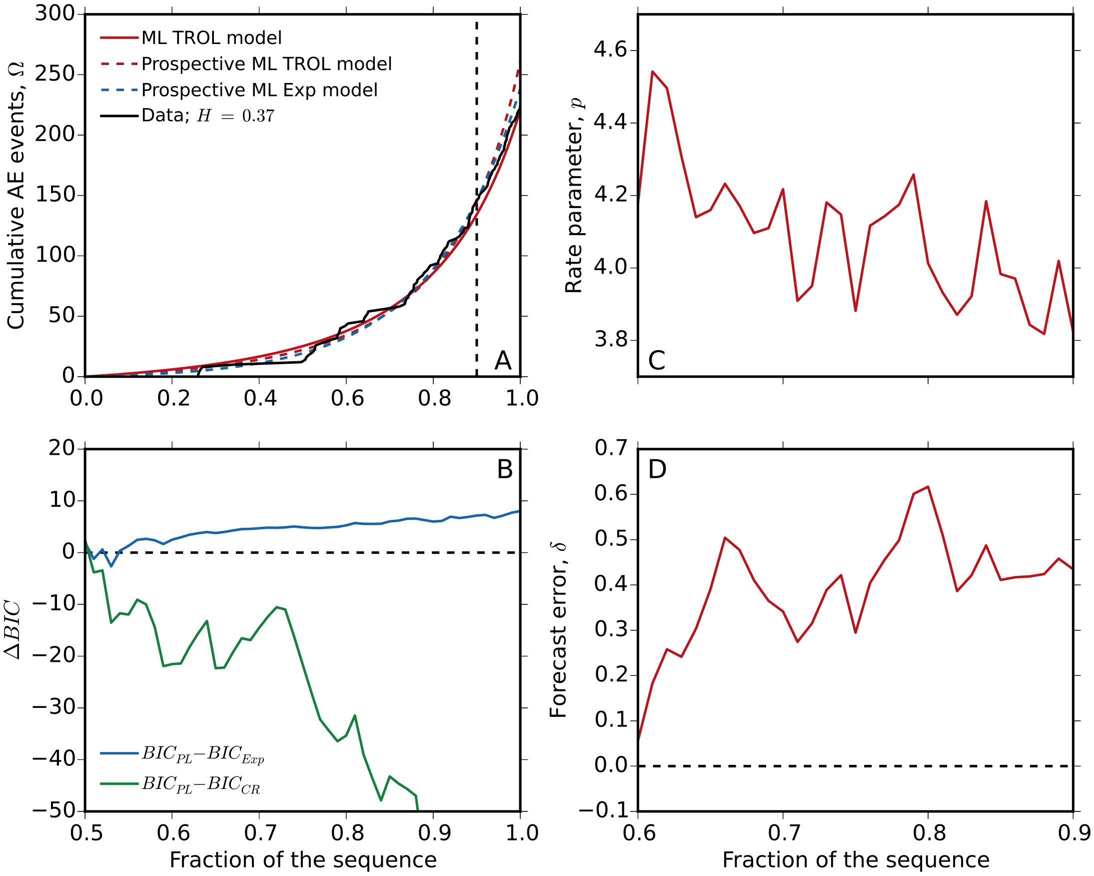

Figure 4.6: Maximum Likelihood failure forecasting for a sample with $H = 0.37$. The composition of panels (A) to (D) and line colour scheme is as for Figure 4.5.

quence). I can note that the forecast error progressively worsens and indicates an overestimation of the actual failure time (late forecast). It is even displayed that in Figure 4.5D the failure time is perfectly resolved at ~61% of the sequence. However, the failure time is better predicted in Figure 4.7D as time approaches it, due to the presence of the power law singularity in the raw data sequence, and the rate parameter decreases toward, or fluctuates around, a value of 1 (Figure 4.7C)

When applying the same methodology to the full AE dataset, the forecasting performance

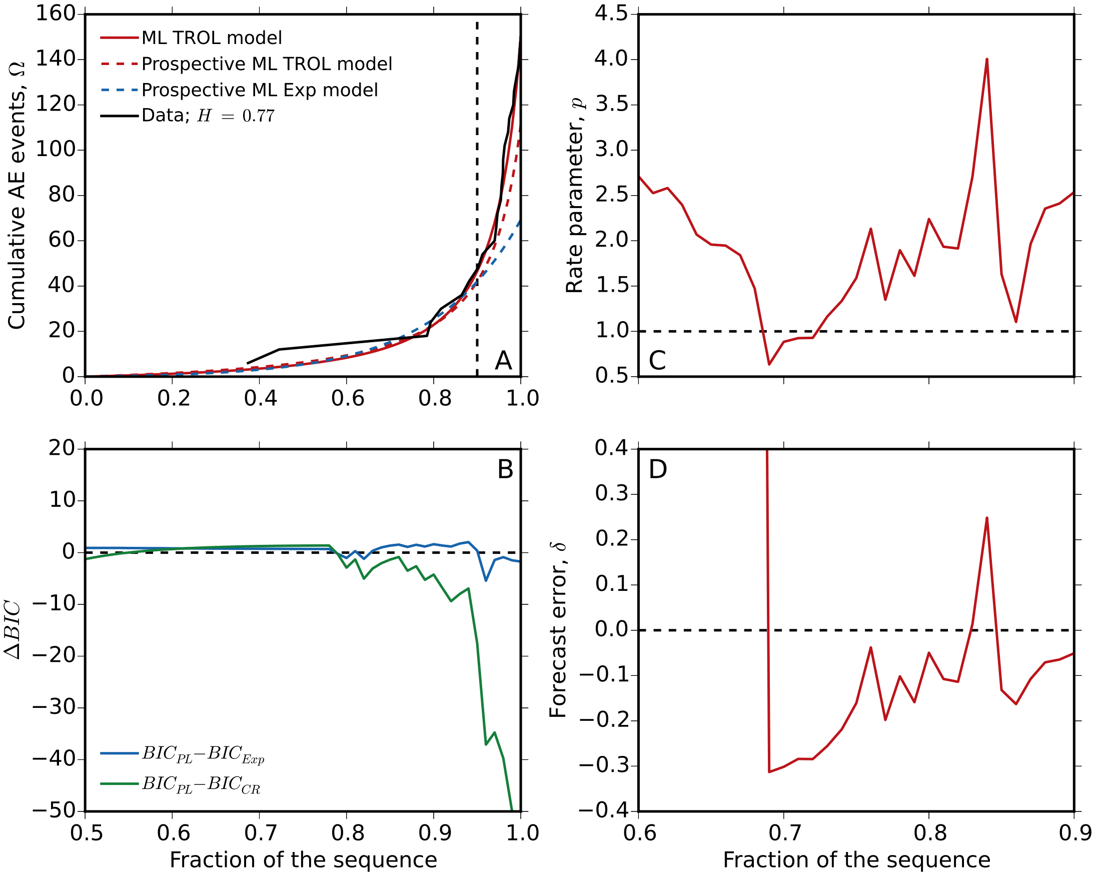

Figure 4.7: Maximum Likelihood failure forecasting for a sample with $H = 0.77$. The composition of panels (A) to (D) and line colour scheme is as for Figure 4.5.

can be evaluated quantitatively as a function of the heterogeneity index (Figure 4.8). The rate parameter shows and overall decrease toward a value of 1 and the absolute forecast error improves systematically, with an increase in the degree of heterogeneity (Figures 4.8A and 4.8B). This is most likely due to the fact that more heterogeneous materials act to inhibit dynamic fractures by crack arrest and/or by introducing a more heterogeneous stress field (consistent with the quasi-static theories used to derive Equation 4.6). In the more homogeneous materials failure results in an abrupt run-away instability that occurs before the forecast singularity is

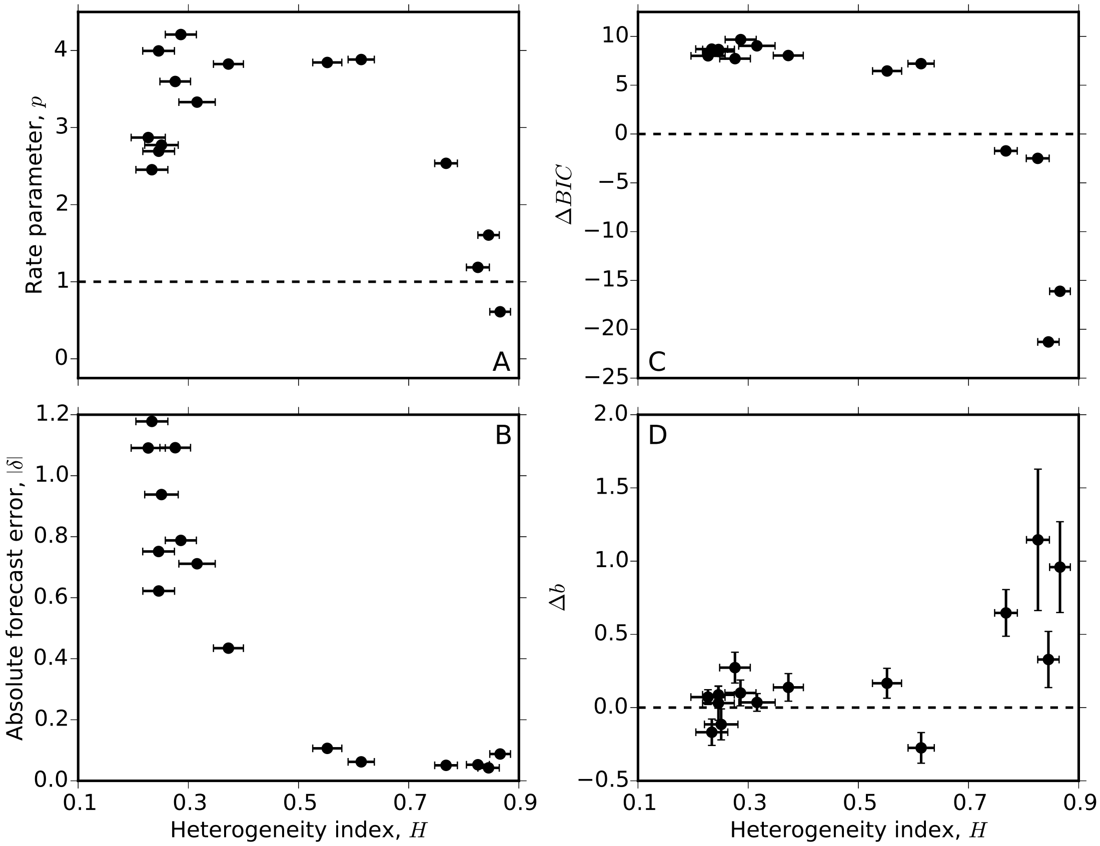

Figure 4.8: Heterogeneity influences on material failure forecasting. As the degree of heterogeneity increases, (A) the rate parameter p generally decreases, (B) the absolute forecast error $|\delta|$ improves, (C) the ΔBIC ($BIC_{PL} - BIC_{Exp}$) displays a marked preference of the TROL over the exponential model and (D) the Δb ($b_{initial} - b_{final}$; see Figure 4.10) shows a higher relative proportion of large to small AE events towards failure.

reached. As a consequence, the systematic forecast error is smaller (the predicted failure time is more accurate) when applied to more heterogeneous materials containing total porosities >0.2, whereas at total porosities <0.2 the error in the predicted failure time can be >100 % of the deformation time.

The TROL is strongly, non-linearly preferred over the exponential model when the entire dataset is used and importantly, as heterogeneity increases (Figure 4.8C). On the other hand, as heterogeneity decreases I observe (1) fewer AEs (providing less advance warning), (2) a preference for the exponential acceleration model (making failure time harder to define) and (3) a sudden-onset singularity at the time of catastrophic failure. All of these elements combine to degrade the forecasting power significantly. In operational terms this would present a serious challenge, for example in forecasting the probability of an eruption during a period of unrest. Additionally, difference in *b*-values[11] shows that it generally decreases as failure approaches, indicating that there is an increase in the relative proportions of large to small AE events that accompany increasingly macroscopic fracturing events (Figure 4.8D).

Since the pioneering studies in the field of earthquake seismology in the early 1960s, the important role of heterogeneity in fracture processes has been evident [Mogi, 1962]. However, this concept has not been developed due to a lack of a physical description of what constitutes heterogeneity inside a material [Sornette, 2002]. Physically I show that it can be described by the simple observable of the volume-averaged quantity of flaws, which, in my chemically stable sintered glass specimens, can be attributed to the pores. The porous network is therefore a good proxy for the effective heterogeneity via its control of the subcritical crack dynamics. Furthermore, the degree of heterogeneity has been shown to either accelerate the dynamics when many spatially diffuse flaws are present or, conversely, to retard dynamics when these flaws are more widely spaced [Ramos et al., 2013]. Although these results contradict apparent advances made by theoretical models [Kierfeld & Vinokur, 2006], they support the idea of sudden rupture in materials that develop more localised, slow crack propagation prior to the expected bulk failure; hence leading to a diminished ability to predict such failure.

---

[11] For a comprehensive analysis, see Section 4.3.3.

4.3.3 STATISTICAL ANALYSIS

MODEL COMPARISON

I undertook a comparative analysis, testing how well the different models of acceleration[12] explain the observed evolution of AE rate with time. I used the BIC (see Kass & Raftery [1995] for a comprehensive review) to quantify the relative performance of different models. This statistical tool is based on the likelihood of the observation given the model, with a weighting favouring the model with fewer parameters. The BIC is given by

$$BIC = -2 \ln (L) + N_p \ln (N_o) \tag{4.21}$$

where L is the likelihood of the observations given the model, N_p is the number of free parameters and N_o is the number of observations. When making an inference, the preferred model is more likely to have the lower BIC. Therefore, calculating the positive difference ΔBIC between two models helps discriminate the preferred model. Here I computed these differences (*i.e.*, $\Delta BIC = BIC_{PL} - BIC_{Exp}$ and $\Delta BIC = BIC_{PL} - BIC_{CR}$) for the AE dataset continuously from 50 to 100% of the sequence such that, when ΔBIC becomes negative it indicates a strong statistical preference for the power law over the other models (Figure 4.9).

AE *b*-VALUE

Complementary statistical analysis of the AE signals following the seismic Gutenberg-Richter (G-R) *b*-value (*i.e.*, the slope of the log-linear frequency-magnitude relationship) indicates that cracking occurs on a broad range of scales as deformation proceeds. The frequency-

---

[12] See Section 4.3.1

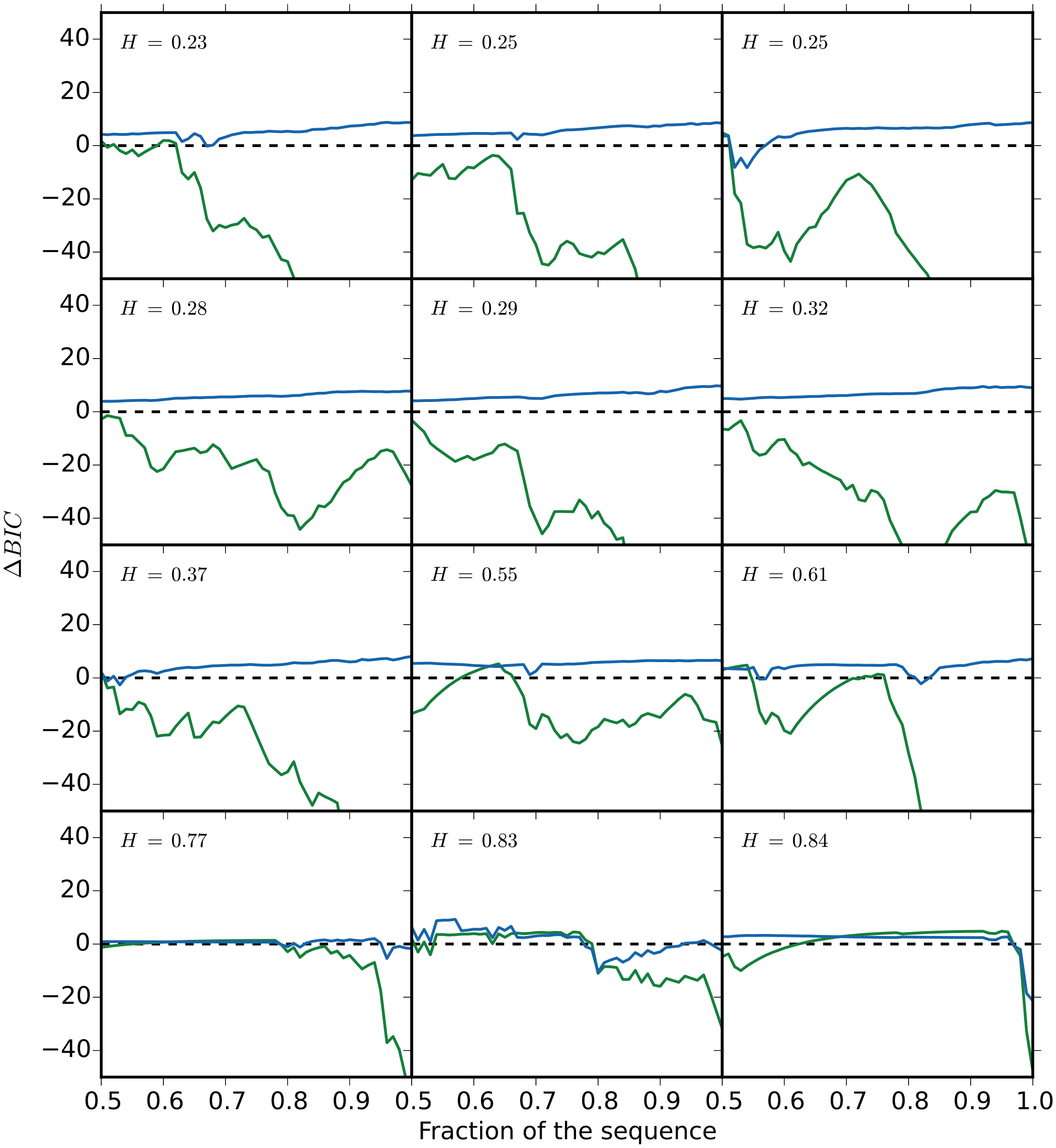

Figure 4.9: Comparison of the ΔBIC between the TROL and exponential model (solid blue lines) and between the TROL and constant rate model (solid green line) as a function of the time fraction to achieve failure (corresponding to 1). Negative values of ΔBIC suggest that the TROL is preferred over the other models. $\Delta BIC = 0$ (*i.e.*, no preference) is indicated as a horizontal dashed black line.

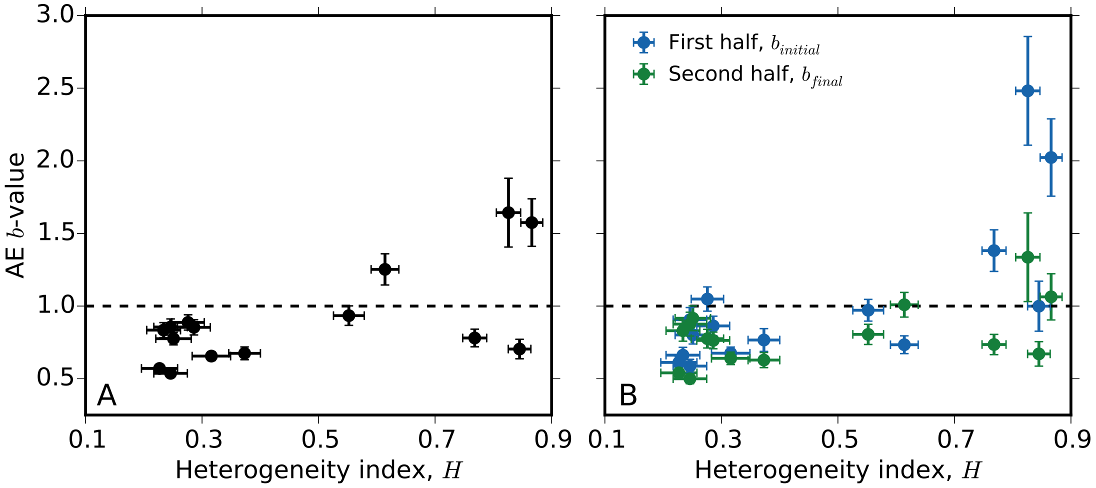

Figure 4.10: AE b-value as a function of heterogeneity. The b-values were determined for (A) the complete experimental AE record, and (B) the first and last halves of the AE events acquired in each experiment (with completeness magnitudes being calculated separately for each half of the data). The AE b-values lie in the range 0.5–1.0, except for samples with higher degrees of heterogeneity, where two experiments show b-values of $\sim$1.6.

magnitude data for the AEs is consistent with a G-R distribution (Figure 4.10A). The G-R b-value was determined for AE events above the completeness magnitude using the ML estimate [Aki, 1965]. Completeness magnitude is taken as the higher of the two values determined by the maximum curvature and b-value stability methods [Mignan & Woessner, 2012] (Figure 4.11). Sensitivity analysis showed that the key b-value results were robust to different completeness magnitude estimation methods and to small uncertainties in the completeness magnitude.

The AE b-value is strongly controlled by the degree of heterogeneity, confirming early observation [Mogi, 1962]. The temporal evolution of the b-value with stress is harder to examine due to the small number of events. The b-value is therefore examined in a coarse way by splitting the data set into two halves, one early and one later (Figure 4.10B). In general the b-

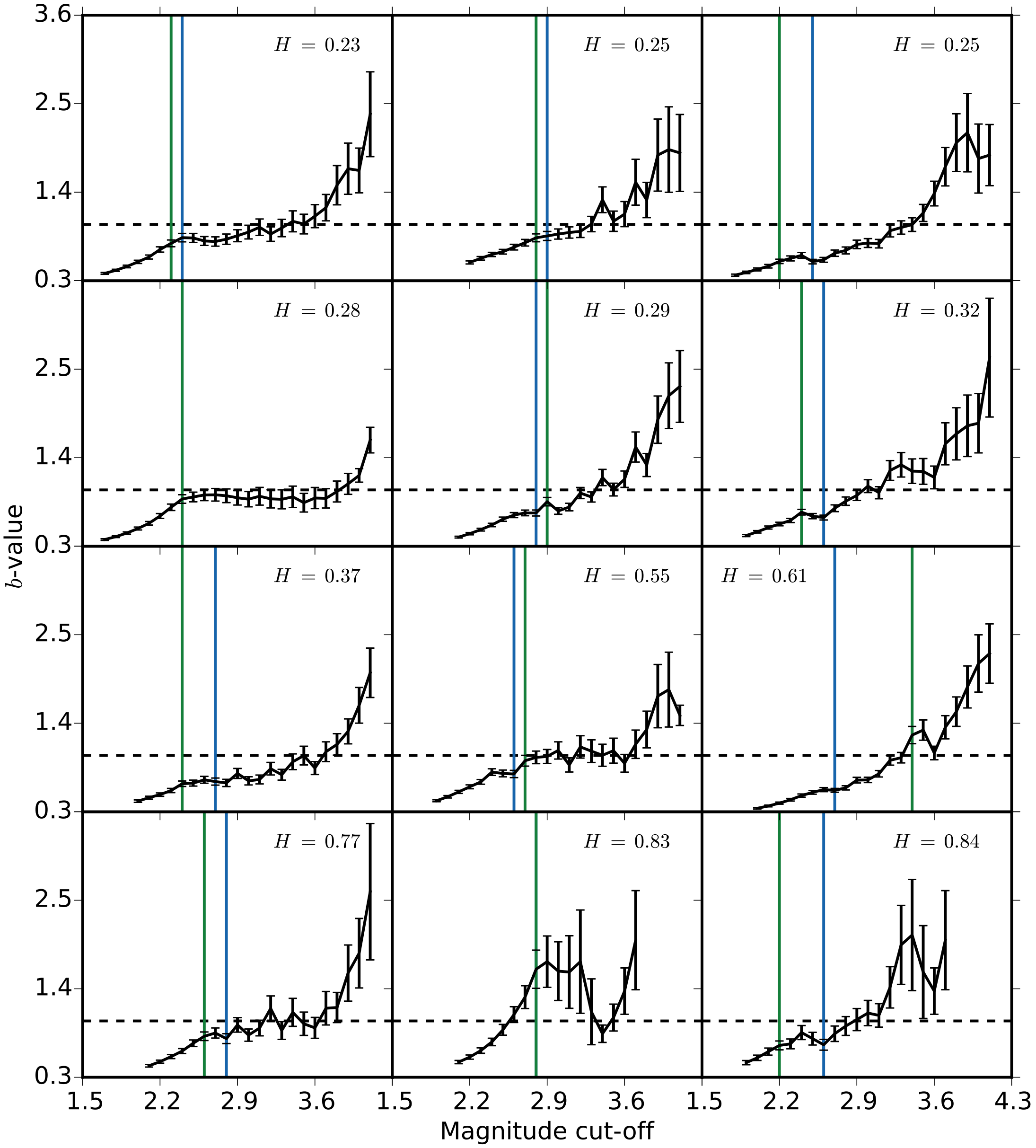

Figure 4.11: Evolution of the AE b-value with the magnitude cut-off as computed using the ML estimate (solid black line). The completeness magnitude determined from the maximum curvature method is indicated by a vertical blue line and from the b-value stability method by a vertical green line. $b = 1$ is indicated as a horizontal dashed black line.

value for materials with large heterogeneity tends to decrease dramatically from >2 to ~ 1, well above the level expected from the estimated random error (plotted as error bars). This is interpreted as initially pervasive microscopic fractures coalescing into macroscopic ones [Main et al., 1989] and the deformation localising on the eventual fracture plane. In contrast, the b-value of less porous material remains around low values of 0.5–1 throughout, suggesting a high degree of localisation throughout [Main et al., 1989]. This is consistent with there being fewer nucleation sites for the low-porosity material. The data presented here is not sufficient to distinguish between models with (a) simple G-R behaviour with variable b-value and (b) an exponentially-truncated G-R model with constant b-value and variable correlation length (*i.e.*, the size of the largest fracture). The latter model and a smooth acceleration in event rate for the heterogeneous samples are however both consistent with the behaviour expected of a second-order phase transition at the critical point [Alava et al., 2006]. On the other hand the sudden-onset instability for the more homogeneous samples is more reminiscent of a first-order phase transition. Numerical simulations should be employed in future to explore this transition from first- to second-order more formally.

4.4 Implications for volcanic eruptions

An estimated 10% of the world's population live in a close vicinity of a historically active volcano [Peterson, 1986]. A great number of volcanic hazards permanently threatens these populations and risk management is of paramount importance in order for inhabitants to be safely evacuated prior to catastrophes. Experts dealing with the tools for hazard assessment often encounter the problem of eruption forecasting; that is to issue a timely warning of not only the expected time and location of a potential eruption, but also the size and the style of activity. Indeed, highly dynamics associated phenomena such as pyroclastic flows pose a more serious risk than other associated phenomena. Forecasting strategies tends more and more to be cast in a probabilistic framework [Marzocchi & Bebbington, 2012], in which physics-based predictive models should be coupled with empirical statistics as well as expert opinion. Predictive models are, as of now, solely based on the temporal evolution of precursory geophysical signals, such as seismicity[13]. Understanding the potential drawbacks and limitations of the FFM is therefore an essential aspect of their responsible application to hazard assessment and risk mitigation.

Previous studies have evaluated the statistical performance of the FFM applied to natural, experimental and synthetic datasets [Bell et al., 2011b, 2013] but to date no study (to the best of my knowledge) has assessed its efficacy as a function of material properties, and the trade-off between quasi-static and dynamic effects at the system size. At volcanoes, successful forecasting is as yet sporadic and requires the laborious classification of volcano-seismic signals. While the onset of magma extrusion due to continued fracturing towards the Earth surface has been retrospectively successfully forecast or "hind-casted" [*e.g.*, Kilburn & Voight, 1998; Kilburn, 2003], this is a necessary but not sufficient criterion for operational or real-time forecasting. In the case of fracturing during magma ascent, seismicity is most likely triggered by fracture propagation in the weakest, most porous parts of the magmatic column. In cases where low-porosity, fine-grained rock or glassy obsidian undergoes fracturing initiated from fewer flaws, I expect to encounter a poor resolution of failure. Such a variable failure forecasting power should equally well apply to the prediction of explosive eruptions for magmas erupting with

---

[13] The relatively low cost and easiness of seismic network deployment makes seismicity a significant geophysical observable at volcanoes; it is also generally recognised as the most reliable precursory activity to volcanic eruptions.

different porosities.

The results presented here shed new light onto the basic physical mechanisms responsible for inaccuracy of time-to-failure forecasting laws, especially in the context of volcanic eruptions. In scenarios where magma ascent timescale is very brief and shorter than that of the seismic unrest, strong deviations from the ideal preparatory fracturing behaviour must be expected. I predict that adaptation of material failure forecasting methods with heterogeneity-based mechanistic constraints will allow predictability of volcanic events in cases when even little warning is available.

The most exciting phrase to hear in science, the one that heralds new discoveries, is not "Eureka!" but "That's funny..."

Isaac Asimov

5

Conclusion and outlook

I INVESTIGATED THE TIMESCALES OF VOLCANIC ASH DENSIFICATION AND HEALING by performing static rheological experiments at temperatures above the glass transition interval of the starting materials. I used different starting materials: (a) a powdered borosilicate glass and (b) two populations of soda-lime silica glass beads. The experiments demonstrated that viscous sintering of volcanic ash is rapid, even under low stress conditions, and is dominantly controlled by melt viscosity (as underlined by the use of (a) at different temperatures), interfacial tension between pores and melt, and particle size (as underlined by the use of (b) at the same temperature). Viscous sintering from a granular material to a homogenous melt is a continuum process involving the evolution from particle agglutination to melt pore collapse. This transition from weak, granular to strong coherent behaviour is observed both texturally and mechanically. The elastic properties of the resultant suspension progressively recover its glass value: (a) the strength recovers according to bubble-bearing liquid failure criterion and (b) the elastic moduli recover according to empirical laws. Although particle angularity has a minor influence on viscous sintering kinetics, it does strongly determine the initial packing and especially the final pore structure. I therefore observed that the elastic moduli is affected by differences in pore shape of the end-products.

Densification and healing of particulate eruptive products is evident in nature and underpins processes of welding by viscous flow under pressure-temperature conditions encountered in volcanic areas. A vast breadth of scenarios have been identified and may occur both inside and outside volcanic conduits. A few examples include tuffisites veins formed during magma ascent in the conduit or during lava dome extrusion following local decompression events due to the opening of fractures, which are thought to be the result of post-decompression sintering of magma fragments, and ignimbrite deposited from downslope pyroclastic density currents, which are thought to be the result of the progressive aggradation and welding of volcanic ash. Since the sintering process essentially implies destruction of pore networks, thereby promoting the evolution of mechanical properties towards those of a dense magma, newly formed sintering material from fallout deposition of ash particles in the conduit or in lava domes will further contribute to sealing of the degassing pathways and the formation of a plug. This behaviour will consequently affect the structural stability of the edifice and supports cyclical-type explosive eruptions observed at many volcanoes around the world.

Applicability of the present sintering experiments to a natural context could be however improved by incorporating the effect of many other physico-chemical parameters. First of all, sintering in a more relevant volcanic atmosphere, such as a water-laden atmosphere, would affect the kinetics by the occurence of coupled viscous-diffusive transport mechanisms. Resorption of chemical species into the melt is a significant viscosity-forcing factor and would either accelerate or retard sintering dynamics. Furthermore, the interaction between gas species and glassy ash particles in volcanic jets or plumes generates the surficial deposition of salt crystals and, upon agglutination, would equally affect sintering kinetics (ongoing study with Dr Paul Ayris, LMU).

Sintering under different loading conditions is something that would also strongly affect the process and results in anisotropic shrinkage (*i.e.*, differential densification). The addition of either a uniaxial or a triaxial stress field would completely alter the dynamics and contribute to a higher degree of densification (under compressive forces) or little, and even no, densification (under tensile forces). Relevant to a volcanic environment would be the simultaneous occurence of shear deformation, which would induce creep-like and densification behaviours. In this case, a creep rate term would have to be added to the differential equation governing the free sintering dynamics, which would imply the derivation of an additional timescale due to a stress intensification factor. The ratio of the creep to the densification rate would thus control the overall kinetics and intuitively be independent of temperature under isothermal conditions, since both of these rates would still depend on melt viscosity. However, in volcanic environments processes are rarely isothermal and the application of heating or cooling rates is yet another viscosity-forcing factor. Sintering during simultaneous heating would enhance the dynamics and could result in fully dense end-products. The timescale involved in this case would have to be translated in terms of a "temperature-scale" by introducing time-dependency of the temperature and integrating the melt viscosity over two extreme values, since it is the only parameter depending significantly on temperature[1]. Conversely, sintering during simultaneous cooling would not enhance the dynamics and could result in preservation of the pore networks.

I also investigated the role of structural heterogeneity during dynamic mechanical experiments on the resultant suite of sintered glass samples, which have been performed in a uniaxial press equipped with a surrounding furnace and a dual acoustic emission recording system. I ran a series of elastic deformation tests until macroscopic sample failure at a constant temperature slightly above the glass transition of the melt (viscous component), but at a constant strain rate high enough to stay within the brittle regime. The application of a statistically-improved failure forecasting method to precursory accelerating microseismic signals, originating from brittle cracking events, demonstrated that failure predictability has a strong non-linear dependence on the degree of sample heterogeneity (which is straightforwardly calculated from the amount of voids). The results are backed up by complementary statistical analyses of the signals: (a) the Gutenberg-Richter *b*-value is in the same fashion controlled by the presence of heterogeneities and cracking mechanisms are inferred from its temporal evolution (a shift from the nucleation and propagation of distributed small-scale to more localised large-scale cracks with decreasing heterogeneity is observed), and (b) com-

---

[1] Wadsworth et al. [2014] have already treated the non-isothermal sintering of synthetic glass particles relevant to volcanic ash under linear heating conditions.

parison of acceleration models indicates that an exponential-like trend (crack nucleation) is favoured over a hyperbolic-like trend (crack coalescence) as heterogeneity decreases, which results in a progressive truncation of the forecast singularity as the sample tends to more unexpectedly shatter from the propagation of pervasive cracks rather than the propagation and coalescence of cracks into a major shear fracture. However, due to very rapid acceleration of the precursors, bulk failure prediction is generally only reliable a short time in advance.

These last results highlight the first-order physical controls on failure predictability in porous materials and have important implications for the prediction of volcanic eruptions. They also highlight the need to reconsider empirical failure forecasting laws in a wider context and better couple them with mechanical parameters, such as failure criteria for heterogeneous materials. Nevertheless, the effect of other forms of heterogeneity could be investigated in the future. The inclusion of crystals in the samples would, for instance, affect the subcritical crack growth dynamics in a non-trivial way. Larger scale heterogeneities (due to the presence of permeable channels) rather than local ones (as it is the case in the porous samples used here) would equally affect the dynamics and possibly boost failure resolution. Performing the same experiments under a range of strain rates, such that they straddle the viscous-brittle transition, would also be the subject of future studies. In this case I would expect an enhancement of failure predictability in the viscoelastic window due to steadiness increase of the cracking dynamics from the occurrence of fracture and healing events during deformation. Future studies should also explore cyclic loading scenarios, which may better represent the pulsatory nature of magma ascent. Only with a thorough understanding of material response to diverse stress conditions will volcanology move forward in the integration of rheology into improve monitoring strategies at active volcanoes.

A

Sandbox for thermo-mechanical modelling

A.1 VISCOUS COMPACTION OF GLASS SHARDS

Here I present a fully analytical approach combining a one-dimensional model for conductive heat transfer with a viscoelastic mechanical model to account for progressive changes in heat conductivity in a porous magma undergoing compaction. This approach has been developed in order to constrain the eruption and emplacement timescales of an ignimbrite deposit.

The assumptions are that (1) the ignimbrite was deposited instantaneously and (2) it experienced no deformation during aggradation. The approach developed here is a simplification of nature as it has been constrained that the deposition of pyroclastic density currents results from progressive aggradation [*e.g.*, Branney & Kokelaar, 1992]; yet I assume that deposition is extremely rapid and that deposition temperature may be relatively uniform, in order to use current mechanical models. Thus, the starting conditions of the model are homogeneous initial temperature and total porosity. The heat transfer is governed by conservation of energy following the one-dimensional heat equation in Cartesian coordinates

$$\frac{\partial T}{\partial t} = D\frac{\partial^2 T}{\partial z^2} \tag{A.1}$$

for which T is the temperature, t is the time, z represents the vertical distance perpendicular to the surface of the deposit and D is the thermal diffusivity of the porous material. The classical definition of the thermal conductivity assumes a pore-free material and, here, I refine this definition to consider the insulation provided by the total porosity φ_T of the material [*e.g.*, Connor et al., 1997]

$$D = \frac{k}{\varrho C_p \left(1 - \varphi_T\right) + \varrho^f C_p^f \varphi_T} \tag{A.2}$$

where k is the thermal conductivity, ϱ and ϱ^f the skeletal and pore fluid density respectively, and C_p and C_p^f the skeletal and pore fluid specific heat capacity respectively. The pore fluid pressure is assumed to be atmospheric, which is reasonable considering the lack of confinement to prevent expansion. The thermal conductivity is also a function of the porosity of the material considered. Some empirical models have been proposed to relate the thermal conductivity of a porous rock to its pore-free thermal conductivity k_0 [Bagdassarov & Dingwell, 1994]

$$k = k_0 \left(\frac{1 - \varphi_T}{1 + \varphi_T} \right) \tag{A.3}$$

Analytical solution of Equation A.1 for geological systems has most commonly been achieved by assuming self-similarity of solutions [Carslaw & Jaeger, 1959]. Assuming homogeneous initial temperature, Carslaw & Jaeger [1959] treat the problem of a cooling magma body in contact with a county rock at $z = 0$ and which solidifies at and below its solidus temperature. In our case I use the glass transition temperature in place of the solidus. A derived solution of Equation A.1 for the temperature profile in the melt is as follows

$$T_{melt}(z, t) = T_i + \frac{T_g - T_i}{\operatorname{erfc}\left(\lambda \frac{D_g}{D_m}\right)} \operatorname{erfc}\left(\frac{z}{2\sqrt{D_m t}} \right) \tag{A.4}$$

where T_i and T_g are the initial and the glass transition temperature of the melt respectively, D_m and D_g the thermal diffusivity of the melt and the glass respectively, and λ a non-defined thermal constant. Carslaw & Jaeger [1959] have shown that the temperature profile in the solid portion, here the glass, can be described by the following equation

$$T_{glass}(z, t) = \frac{T_g}{k_g\sqrt{D_c} + k_c\sqrt{D_g}\operatorname{erf}(\lambda)} \left(k_g\sqrt{D_c} + k_c\sqrt{D_g}\operatorname{erf}\left(\frac{z}{2\sqrt{D_g t}} \right) \right) \tag{A.5}$$

where D_c is the thermal diffusivity of the underlying country rock, and k_g and k_c the thermal conductivity of the glass and the country rock respectively. The solidification surface occurs following

$$z_{glass}(t) = 2\lambda\sqrt{D_m t} \tag{A.6}$$

This thermal approach is further combined with a mechanistic and kinetic description of the compaction of the deposited ash [Quane & Russell, 2005, 2006; Quane et al., 2009]. The porosity evolution with stress σ, viscosity of the material at zero porosity η_0 and time t can be derived using the empirical equation [Quane et al., 2009]

$$\Delta t = \frac{\eta_0}{\alpha\sigma\left(1 - \varphi_{T,i}\right)} \left(\exp\left(-\frac{\alpha\varphi_T}{1 - \varphi_T}\right) - \exp\left(-\frac{\alpha\varphi_{T,i}}{1 - \varphi_{T,i}}\right)\right) \tag{A.7}$$

where

$$\varphi_T\left(t\right) = \frac{\beta}{\beta - \alpha} \tag{A.8}$$

and

$$\beta = \ln\left(\frac{\alpha\sigma}{\eta_0\left(1 - \varphi_{T,i}\right)} t + \exp\left(-\frac{\alpha\varphi_{T,i}}{1 - \varphi_{T,i}}\right)\right) \tag{A.9}$$

Here, $\varphi_{T,i}$ is the initial total porosity and α an empirical constant. Following Quane et al. [2009] I use $\alpha = 0.78$ for packing of volcanic ash. The stress distribution across the entire deposit is described by the overburden as

$$\sigma\left(z\right) = \left(1 - \varphi_T\right) \varrho g z \tag{A.10}$$

where g is the acceleration of the gravity.

Equations A.2–A.10 provide the necessary tools to iterate a thermo-mechanical model describing the feedbacks between compaction via destruction of porosity, temperature (and thus viscosity) and stress upon deposition. Using a set of constrained glass parameters (Table A.1; $\varphi_{T,i} = 0.5$ and $\lambda = 3.6$), I simulate the progression of compaction as a function of time and initial temperature (Figure A.1). The model results suggest that for the pyroclasts at a stratigraphic height of $z = 0.3$ m to reach the measured $\varphi_T = 0.075$ at $T = T_g$, and a

Table A.1: Initial parameters.

	k_0 $\mathrm{m^2\,s^{-1}}$	ϱ $\mathrm{kg\,m^{-3}}$	C_p $\mathrm{J\,kg^{-1}\,K^{-1}}$
Melt/Glass	1.59	2.9×10^3	1×10^3
Country rock	1.59	2.33×10^3	1×10^3
Pore fluid	2.5×10^{-2}	1.275	1.007×10^3

constrained cooling rate of 0.1 K min^{-1}, ∼1 hour is required. Due to the interplay between cooling and compaction, I can further deduce that ∼1240 K is the idealised deposition temperature T_i to meet the measured conditions of porosity, stratigraphic position and cooling rate (Figure A.2). This compaction time estimate may be faster if syn-depositional shearing [*e.g.*, Robert et al., 2013] were to have achieved higher stresses than the overburden load considered in our model.

The welding timescale calculated here agrees well with the 12–20 min proposed by similar rheological modelling by Robert et al. [2013], but is significantly shorter than the 10–15 h proposed for the Bishop Tuff (Long Valley Caldera, California, USA) by Wilson & Hildreth [1997]. In contrast it is orders of magnitude more rapid than the thermo-mechanical constraints on the Bandelier Tuff (Valles Caldera, New Mexico, USA) estimated at 1–5 days [Quane et al., 2009], the Rattlesnake Tuff estimated at 10s of days [Riehle et al., 2010], the Bishop Tuff estimated at 10–100s of days [Wilson & Hildreth, 1997; Sheridan & Wang, 2005; Riehle et al., 2010], and on a rheomorphic phonolitic fallout deposit (Las Cañadas Caldera, Tenerife, Spain) estimated at 25–54 days [Soriano et al., 2002]. The study constrains that welding is not, as previously suggested, decoupled from cooling [*e.g.*, Sheridan & Wang, 2005] but rather synchronous with cooling. Here I demonstrate that welding (*i.e.*, sintering and formation of eutaxitic textures) reflects the temperature-time window in which the

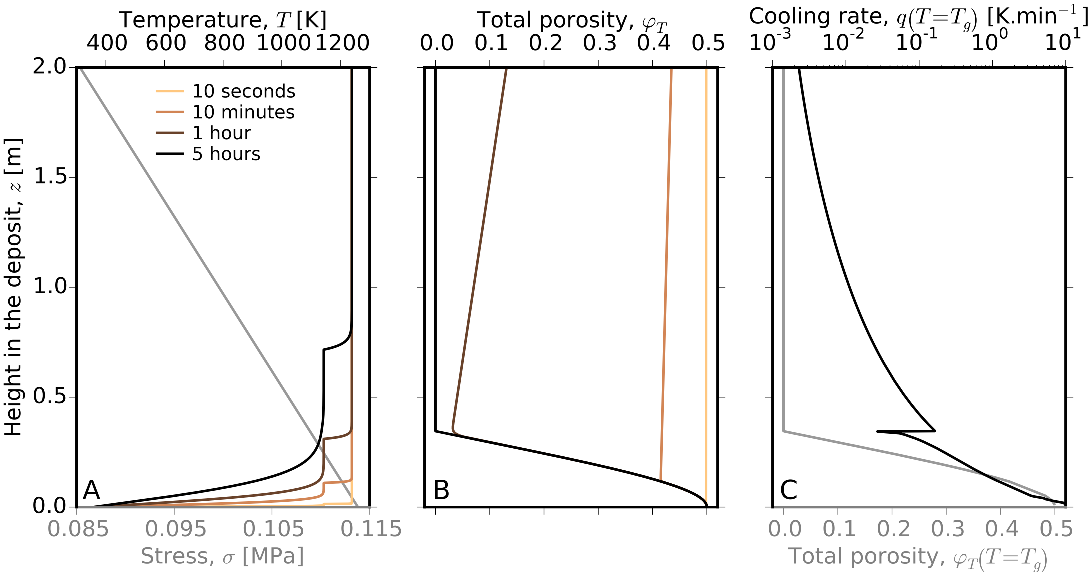

Figure A.1: Results from the 1D analytical thermo-mechanical model for the lower half of the deposit. (A) Overburden stress and time-dependent temperature in the deposit after homogeneous initial conditions of 1240 K and 0.5 total porosity. (B) Total porosity evolution during viscous compaction and cooling between 10 s and 5 h. (C) Cooling rate (solid black line) and total porosity (solid grey line) locked in the glass as the melt crosses T_g.

erupted products remain in the liquid state (above the glass transition temperature of the glass fraction of the pyroclasts).

The general agreement between the onset temperature of welding (1240 K) and the geothermometric constraint (1173–1323 K) suggests that little cooling took place during eruption and transport (unless frictional processes contributed in large amounts; [*e.g.*, Robert et al., 2013; Lavallée et al., 2014]). In this sense, there are strong parallels between large ignimbrites and tuffisites within silicic lava-filled conduits, which exhibit similar dense welding textures [*e.g.*, Tuffen et al., 2003]. In tuffisites, minimal cooling occurs between fragmentation and sintering due to isolation from the atmosphere in intrusive pyroclastic channels. The inference is that for large-volume ignimbrites the bulk of the magma is similarly thermally insulated from

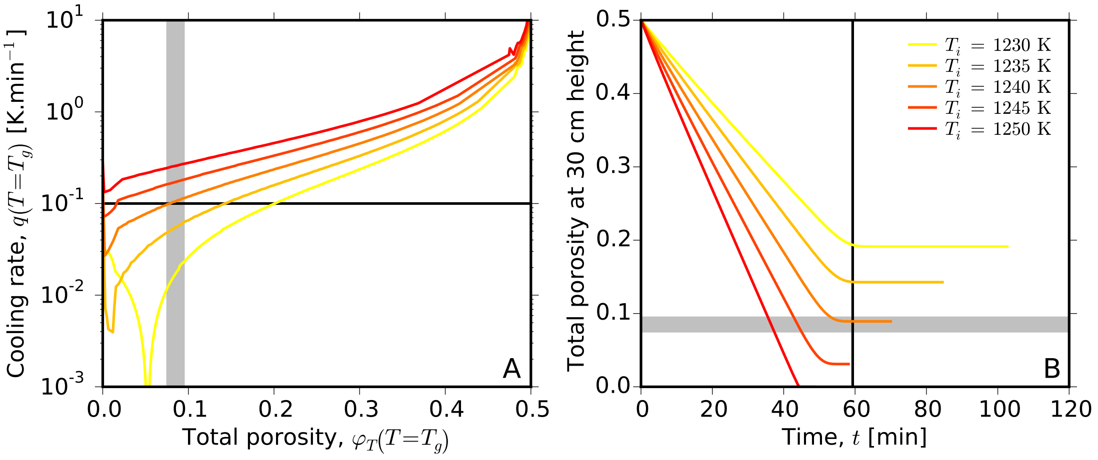

Figure A.2: Estimation of the temperature of deposition and the timescale to reach the measured porosity at a stratigraphic height of 30 cm in the deposit. (A) Intersection of a cooling rate of $0.1\ \mathrm{K\ min}^{-1}$ (horizontal black line) and a total porosity of 0.075 at a height of 30 cm (vertical shaded area) constrains an initial deposition temperature of ∼1240 K. (B) The time required to produce the total porosity observed at a height of 30 cm whilst cooling to ∼1240 K constrained here to ∼60 min (vertical black line). Horizontal shaded area same as for panel (A).

the atmosphere [Suzuki & Koyaguchi, 2010; Sulpizio & Dellino, 2014], despite degassing to near-atmospheric pressure; a similar insulation has been postulated from examination of ignimbrite emplaced sub-aqueously [Kokelaar & Königer, 2000]. This must reflect minimal entrainment of surrounding fluids (air or water) during pyroclastic fountaining and flow. It may also reflect a wide source vent [*e.g.*, Legros et al., 2000]. Cooling of pyroclasts may therefore be largely prevented until deposition [*e.g.*, Lesti et al., 2011], thus supporting the view that the thermal history of explosive eruptions and emplacement are decoupled.

A.2 Temperature delay in a rotary shear apparatus

Here I present a simple solution to heat diffusion in a rotary shear apparatus. The experimental setup is designed to investigate the occurrence of frictional melting at a slip interface between two rocks (see Hirose & Shimamoto [2005] for details of the technique). It consists of two plane-parallel cylindrical rock samples, which are put in face-to-face contact by applying a normal stress (1.5 MPa) to their axial surface; one of them is held stationary while the other is placed in the rotary side of the loading column and suddenly spin following a radial velocity of 1.3 m s^{-1}. The stationary sample has axis-parallel drill holes for the insertion of thermocouples. In the case of rapid heating which accompanies high velocity friction, the temperature monitored in the host rock only provides an approximation of the actual temperature at the slip interface; in fact, the thermocouple reads the temperature dissipated through time. It thus results that each read temperature increments was experienced at the slip interface at an earlier time. I assume a semi-infinite one-dimensional medium undergoing thermal conduction (neglecting dissipation), following the heat equation in Cartesian coordinates

$$-\frac{\partial^2 T}{\partial x^2} = \frac{1}{D}\frac{\partial T}{\partial t} \tag{A.11}$$

for which T is the temperature, t is the time, x is the horizontal distance from the thermocouple and D is the thermal diffusivity. The initial and boundary conditions read as

$$T(x, t = 0) = T_i \tag{A.12}$$

$$T(x = 0, t) = T_c \tag{A.13}$$

where T_i is the uniform initial temperature of the medium, T_c the temperature measured by the thermocouple at a distance monitored during the experiment. Upon slip and heating, a temperature T is imposed at the interface (using a Dirichlet boundary condition which averages the imposed fix temperature at each time interval). I apply the following change of variable $\bar{T} = T - T_i$ to Equation A.11 in order to extract the temperature at a position x, thus obtaining

$$-\frac{\partial^2 \bar{T}}{\partial x^2} - \frac{1}{D}\frac{\partial \bar{T}}{\partial t} = 0 \tag{A.14}$$

with Equations A.12 and A.13 becoming

$$\bar{T}(x, t = 0) = 0 \tag{A.15}$$

$$\bar{T}(x = 0, t) = T_c - T_i \tag{A.16}$$

Equation A.14 can be solved using the following Laplace transform

$$\vartheta(x, p) = L\left\{\bar{T}(t)\right\} = \int_0^\infty \exp(-pt)\, \bar{T}(x, t)\, dt \tag{A.17}$$

which, once applied to Equation A.14, provides me with

$$-\frac{d^2\vartheta}{dx^2} - \frac{1}{D}\left(p\vartheta - \bar{T}(x, t = 0)\right) = 0 \tag{A.18}$$

Using Equation A.15 it further simplifies to

$$-\frac{d^2\vartheta}{dx^2} - q^2\vartheta = 0 \tag{A.19}$$

with

$$q^2 = \frac{p}{D} \tag{A.20}$$

Equation A.19 offers a mathematical solution of the type

$$\vartheta(x,p) = -\left(A\exp(-qx) + B\exp(qx)\right) \tag{A.21}$$

The temperature keeps a finite value when x tends towards infinity, so that $B = 0$ and $A = \frac{T_c - T_i}{p}$ from Equation A.16. Henceforth, the use of the Laplace inverse transform leads to

$$\vartheta(x,p) = -\left(T_c - T_i\right)\operatorname{erf}\left(\frac{x}{2\sqrt{Dt}}\right) \tag{A.22}$$

and finally

$$T(x,t) = T_i - \left(T_c - T_i\right)\operatorname{erf}\left(\frac{x}{2\sqrt{Dt}}\right) \tag{A.23}$$

which is used to approximate the temperature along the slip interface using a thermal diffusivity of $5.3 \times 10^{-7}\ \mathrm{m^2\,s^{-1}}$.

Although simplistic in its discretisation of time and temperature intervals, the estimation provided by Equation A.23 appears to satisfactorily approximate the evolution of temperature during slip, since the modelled temperatures initially diverge from the thermocouple read out (while heating takes place faster than what is recorded), then converge as the sample shortens and the thermocouple approaches and intrudes the melt zone (henceforth providing an in-situ measurement of the melt temperature), as seen in Figure A.3. The thermal constraint has obvious implication for the mechanics experienced at the slip zone. Yet, a more accurate three-dimensional derivation of the temperature evolution via the forward iteration of an analytical solution to Fourier's law of conduction applied to a cylinder will require attention in the future.

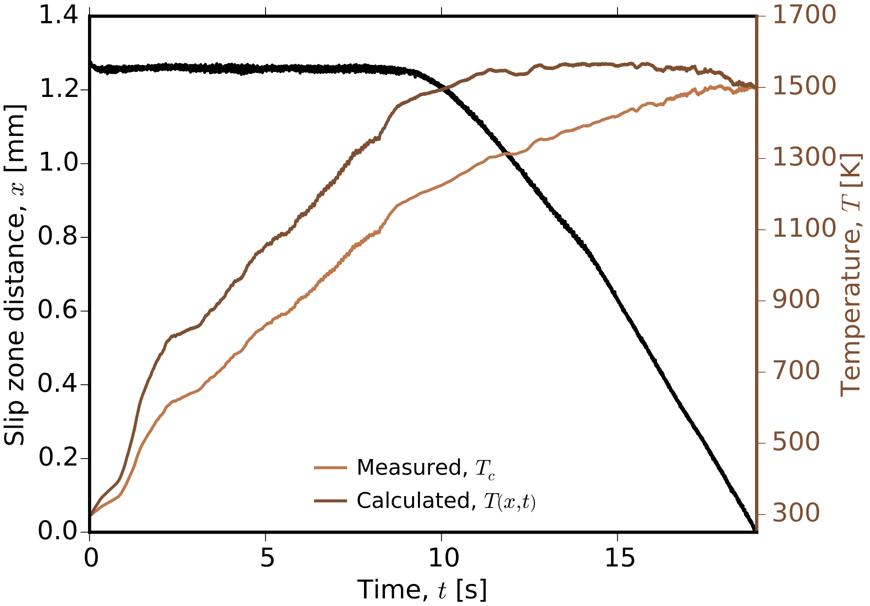

Figure A.3: Evolution of the slip zone (*i.e.*, the interface between the two rocks) distance from the thermocouple (input in the model as x; solid black line), of the temperature recorded at the thermocouple (T_c; solid pale brown line) and of the back-modelled temperature at the slip zone ($T(x, t)$; solid brown line).

B

Toolbox for microseismic data processing

A toolbox for AE data handling and processing has been designed and coded using Python programming language. The scripts are continuously being revised as new analysis becomes necessary to further our understanding of coupled acoustic-mechanic behaviour of volcanic materials. The package is based on, and works together with, the now famous ObsPy toolbox— a free and platform-independent Python toolbox to handle seismological data from observatories—

developed and maintained by the ObsPy Development Team (devs@obspy.org) at the Department of Earth and Environmental Sciences, section Geophysics, of the Ludwig Maximilian University of Munich [Beyreuther et al., 2010].

The AEproc package contains common methods and modules to handle and process continuous AE streams recorded by a Richter data acquisition system using the eXstream software developed by Applied Seismology Consultants (ASC, UK). This system provides up to 20 MHz 12-bit full-waveform acquisition in both streaming and triggering mode. ASC's flagship software, the InSite Seismic Processor, is a full-fledged toolbox for microseismic data handling and processing (including modules for data management, waveform visualisation, event location and mechanism, etc.). The Streamer Leach module of InSite offers the possibility to automatically trigger events from continuous AE signals for further processing. However, research sometimes requires the numerical implementation of newly developed techniques and methods, such that it is more convenient to be able to use a programming language. Here I developed scripts in Python to complete AE data analysis. Python is open-source, platform-independent and modular, and its popularity has been accelerating over the years, such that it is increasingly used in various fields and especially, in seismology. This is because its comprehensive standard library, as well as freely available libraries developed by people and companies around the world, provide tools for all kinds of tasks and, in particular, has excellent features for interfacing C/C++ and Fortran codes.

As of today, AEproc has got essential seismological processing routines via the use of ObsPy. AE data share similar characteristics with classical seismic data; however, their major difference arises from the sampling rate, which implies that specific routines have to be adapted to properly handle AE data. In particular, Obspy's `UTCDateTime` object based on Python's built-in `datetime` object[1] has a maximum time precision on the order of a microsecond, while microseismic signals recorded at >1 MHz require a higher precision to be handled properly. In AEproc, I redefine a `DateTime` object (Figure B.1) based on the excellent eGenix's `mx-DateTime` package, which has a maximum time precision on the order of a nanosecond. AEproc is constituted of five main modules (Figure B.1): (a) a core module (`aeproc.core`) provides classes for date, time and waveform manipulation (via the concept of streams and traces, as originally implemented in ObspPy), classes for raw data file input/output and storage, reading functions[2] and various functions and methods as utilities; (b) a visualisation module (`aeproc.visu`) for waveform and spectrum (power spectrum, spectrogram and scalogram in the form of a continuous wavelet transform) plotting; (c) a signal module (`aeproc.signal`) contains diverse functions for signal processing such as a calibration, de-noising, filtering (finite impulse response filters), root-mean-square computation, AIC computation, etc.; (d) an energy module (`aeproc.energy`) for continuous real-time seismic energy computation on streams; and (e) an events module (`aeproc.events`) for event triggering from continuous streams of data and event manipulation (*e.g.*, amplitude and energy estimation).

---

[1] The `datetime` module supplies classes for manipulating dates and times in both simple and complex ways.

[2] Only the SRM file format is supported at the moment.

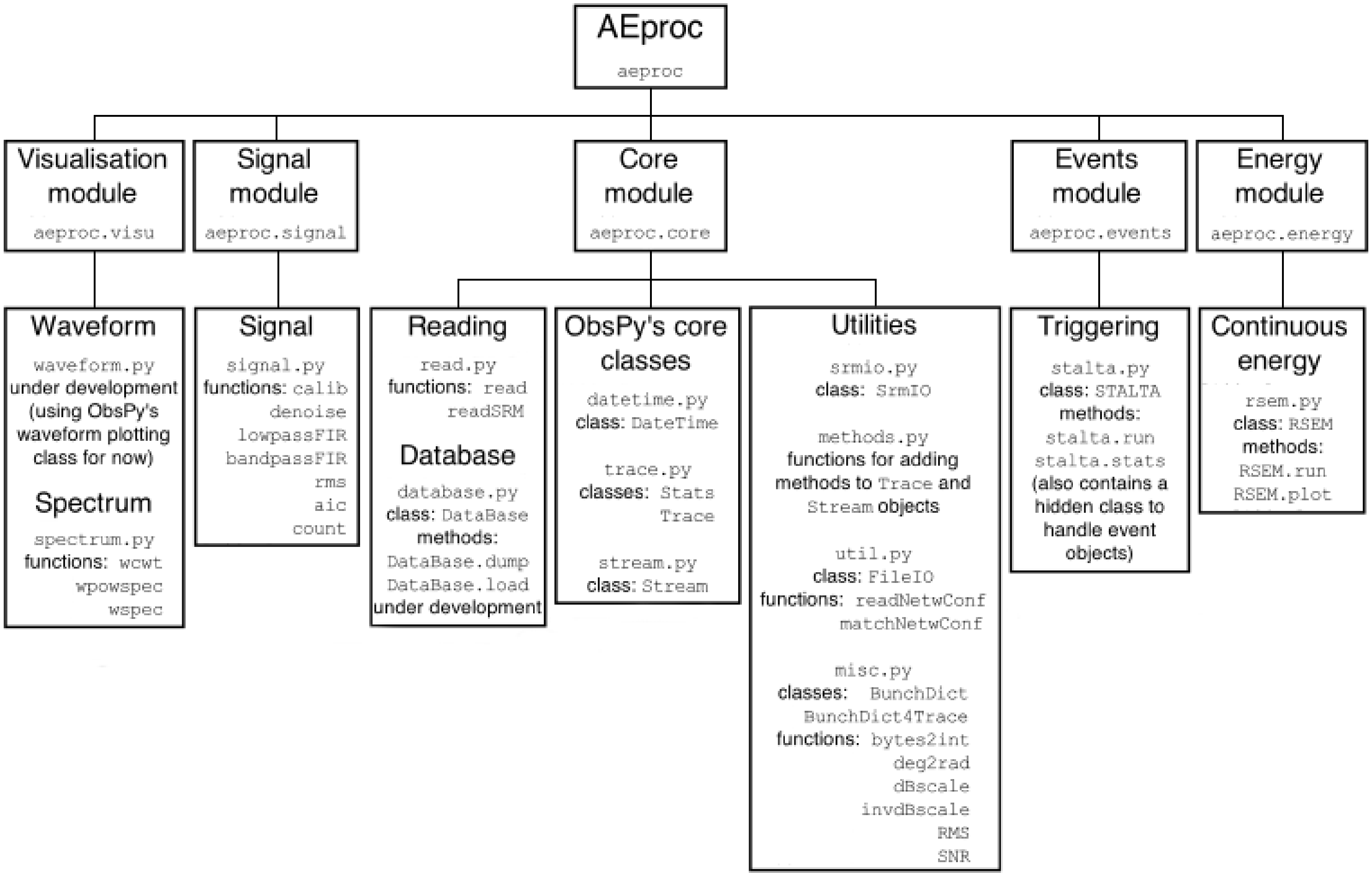

Figure B.1: A diagram summarising the components of AEproc.

References

Akaike, H. (1974). Markovian representation of stochastic processes and its application to the analysis of autoregressive moving average processes. *Annals of the Institute of Statistical Mathematics*, 26(1), 363–387.

Aki, K. (1965). Maximum likelihood estimate of b in the formula log(N) = a - bM and its confidence limits. *Bulletin of the Earthquake Research Institute*, 43, 237–239.

Alava, M. J., Nukala, P. K. V. V., & Zapperi, S. (2006). Statistical models of fracture. *Advances in Physics*, 55(3-4), 349–476.

Anderson, O. L. & Grew, P. C. (1977). Stress corrosion theory of crack propagation with applications to geophysics. *Reviews of Geophysics*, 15(1), 77–104.

Arciniega-Ceballos, A., Alatorre-Ibargüengoitia, M. A., Scheu, B., Dingwell, D. B., & Delgado-Granados, H. (2014). Seismological analysis of conduit dynamics in fragmentation experiments. *Journal of Geophysical Research*, 119(3), 2215–2229.

Ashby, M. F. (1974). A first report on sintering diagrams. *Acta Metallurgica*, 22(3), 275–289.

Atkinson, B. K. (1982). Subcritical crack propagation in rocks: Theory, experimental results and applications. *Journal of Structural Geology*, 4(1), 41–56.

Baer, M. & Kradolfer, U. (1987). An automatic phase picker for local and teleseismic events. *Bulletin of the Seismological Society of America*, 77(4), 1437–1445.

Bagdassarov, N. & Dingwell, D. B. (1994). Thermal properties of vesicular rhyolite. *Journal of Volcanology and Geothermal Research*, 60(2), 179–191.

Bak, P., Christensen, K., Danon, L., & Scanlon, T. (2002). Unified scaling law for earthquakes. *Physical Review Letters*, 88(17), 178501.

Bell, A. F., Greenhough, J., Heap, M. J., & Main, I. G. (2011a). Challenges for forecasting based on accelerating rates of earthquakes at volcanoes and laboratory analogues. *Geophysical Journal International*, 185(2), 718–723.

Bell, A. F. & Kilburn, C. R. J. (2012). Precursors to dyke-fed eruptions at basaltic volcanoes: Insights from patterns of volcano-tectonic seismicity at Kilauea volcano, Hawaii. *Bulletin of Volcanology*, 74(2), 325–339.

Bell, A. F., Naylor, M., Heap, M. J., & Main, I. G. (2011b). Forecasting volcanic eruptions and other material failure phenomena: An evaluation of the failure forecast method. *Geophysical Research Letters*, 38(15), L15304.

Bell, A. F., Naylor, M., & Main, I. G. (2013). The limits of predictability of volcanic eruptions from accelerating rates of earthquakes. *Geophysical Journal International*, 194(3), 1541–1553.

Benson, P. M., Heap, M. J., Lavallée, Y., Flaws, A., Hess, K.-U., Selvadurai, A. P. S., Dingwell, D. B., & Schillinger, B. (2012). Laboratory simulations of tensile fracture development in a volcanic conduit via cyclic magma pressurisation. *Earth and Planetary Science Letters*, 349-350, 231–239.

Benson, P. M., Thompson, B. D., Meredith, P. G., Vinciguerra, S., & Young, R. P. (2007). Imaging slow failure in triaxially deformed Etna basalt using 3D acoustic-emission location and X-ray computed tomography. *Geophysical Research Letters*, 34(3), L03303.

Benson, P. M., Vinciguerra, S., Meredith, P. G., & Young, R. P. (2008). Laboratory simulation of volcano seismicity. *Science*, 322(5899), 249–252.

Benson, P. M., Vinciguerra, S., Meredith, P. G., & Young, R. P. (2010). Spatio-temporal evolution of volcano seismicity: A laboratory study. *Earth and Planetary Science Letters*, 297(1-2), 315–323.

Benson, P. M., Vinciguerra, S., Nasseri, M. H. B., & Young, R. P. (2014). Laboratory simulations of fluid/gas induced micro-earthquakes: Application to volcano seismology. *Frontiers in Earth Science*, 2(32).

Beyreuther, M., Barsch, R., Krischer, L., Megies, T., Behr, Y., & Wassermann, J. (2010). ObsPy: A Python toolbox for seismology. *Seismological Research Letters*, 81(3), 530–533.

Bhat, T. B. & Arunachalam, V. S. (1980). Inhomogeneous flow and the effective pressure concept in pressure sintering. *Journal of Materials Science*, 15(7), 1614–1618.

Bonamy, D., Prades, S., Rountree, C. L., Ponson, L., Dalmas, D., Bouchaud, E., Ravi-Chandar, K., & Guillot, C. (2006). Nanoscale damage during fracture in silica glass. *International Journal of Fracture*, 140(1-4), 3–14.

Branney, M. J. & Kokelaar, P. (1992). A reappraisal of ignimbrite emplacement: Progressive aggradation and changes from particulate to non-particulate flow during emplacement of high-grade ignimbrite. *Bulletin of Volcanology*, 54(6), 504–520.

Burlini, L., Vinciguerra, S., Di Toro, G., De Natale, G., Meredith, P. G., & Burg, J.-P. (2007). Seismicity preceding volcanic eruptions: New experimental insights. *Geology*, 35(2), 183.

Cabrera, A., Weinberg, R. F., Wright, H. M. N., Zlotnik, S., & Cas, R. A. F. (2011). Melt fracturing and healing: A mechanism for degassing and origin of silicic obsidian. *Geology*, 39(1), 67–70.

Cahn, R. W. (1991). Metallic glasses. In *Glasses and amorphous materials*, volume 9 (pp. 493). Weinheim, Germany: Wiley-VCH.

Carslaw, H. S. & Jaeger, J. C. (1959). *Conduction of heat in solids*. Oxford, UK: Clarendon Press.

Castro, J. M. & Cashman, K. V. (1999). Constraints on rheology of obsidian lavas based on mesoscopic folds. *Journal of Structural Geology*, 21(7), 807–819.

Castro, J. M., Cordonnier, B., Tuffen, H., Tobin, M. J., Puskar, L., Martin, M. C., & Bechtel, H. A. (2012). The role of melt-fracture degassing in defusing explosive rhyolite eruptions at volcán Chaitén. *Earth and Planetary Science Letters*, 333-334, 63–69.

Célarié, F., Prades, S., Bonamy, D., Ferrero, L., Bouchaud, E., Guillot, C., & Marlière, C. (2003). Glass breaks like metal, but at the nanometer scale. *Physical Review Letters*, 90(7), 075504.

Charles, R. J. (1958). Static fatigue of glass. *Journal of Applied Physics*, 29(11), 1549–1560.

Charles, R. J. & Hillig, W. B. (1962). The kinetics of glass failure by stress corrosion. In *Symposium sur la Résistance Mécanique du Verre et les Moyens de l'Ameliorer* (pp. 511–527). Charleroi, Belgium.

Coble, R. L. (1961). Sintering crystalline solids. I. Intermediate and final state diffusion models. *Journal of Applied Physics*, 32(5), 787–792.

Cocks, A. C. F. (1989). Inelastic deformation of porous materials. *Journal of the Mechanics and Physics of Solids*, 37(6), 693–715.

Cocks, A. C. F. (1994). The structure of constitutive laws for the sintering of fine grained materials. *Acta Metallurgica et Materialia*, 42(7), 2191–2210.

Coleman, S. C. & Beere, W. B. (1975). The sintering of open and closed porosity in UO2. *Philosophical Magazine*, 31(6), 1403–1413.

Connor, C. B., Lichtner, P. C., Conway, F. M., Hill, B. E., Ovsyannikov, A. A., Federchenko, I., Doubik, Y., Shapar, V. N., & Taran, Y. A. (1997). Cooling of an igneous dike 20 yr after intrusion. *Geology*, 25(8), 711–714.

Cordonnier, B., Caricchi, L., Pistone, M., Castro, J. M., Hess, K.-U., Gottschaller, S., Manga, M., Dingwell, D. B., & Burlini, L. (2012a). The viscous-brittle transition of crystal-bearing silicic melt: Direct observation of magma rupture and healing. *Geology*, 40(7), 611–614.

Cordonnier, B., Schmalholz, S. M., Hess, K.-U., & Dingwell, D. B. (2012b). Viscous heating in silicate melts: An experimental and numerical comparison. *Journal of Geophysical Research*, 117(B2), B02203.

Cornelius, R. R. & Voight, B. (1994). Seismological aspects of the 1989–1990 eruption at Redoubt Volcano, Alaska: The Materials Failure Forecast Method (FFM) with RSAM and SSAM seismic data. *Journal of Volcanology and Geothermal Research*, 62(1), 469–498.

Cox, S. J. D. & Meredith, P. G. (1993). Microcrack formation and material softening in rock measured by monitoring acoustic emissions. *International Journal of Rock Mechanics and Mining Sciences*, 30(1), 11–24.

Das, S. & Scholz, C. H. (1981). Theory of time-dependent rupture in the earth. *Journal of Geophysical Research*, 86(B7), 6039–6051.

Davidsen, J., Stanchits, S., & Dresen, G. (2007). Scaling and universality in rock fracture. *Physical Review Letters*, 98(12), 125502.

Davies, P. (1992). *The new physics*. Cambridge, UK: Cambridge Univ. Press.

de Jonghe, L. C. & Rahaman, M. N. (1984). Pore shrinkage and sintering stress. *Journal of the American Ceramic Society*, 67(10), C–214–C–215.

de Jonghe, L. C. & Rahaman, M. N. (1988). Sintering stress of homogeneous and heterogeneous powder compacts. *Acta Metallurgica*, 36(1), 223–229.

De la Cruz-Reyna, S. & Reyes-Dávila, G. A. (2001). A model to describe precursory material-failure phenomena: Applications to short-term forecasting at colima volcano, Mexico. *Bulletin of Volcanology*, 63(5), 297–308.

Dingwell, D. B. (1996). Volcanic dilemma: Flow or blow? *Science*, 273(5278), 1054–1055.

Dingwell, D. B. & Webb, S. L. (1989). Structural relaxation in silicate melts and non-Newtonian melt rheology in geologic processes. *Physics and Chemistry of Minerals*, 16(5), 508–516.

Du, Z. Z. & Cocks, A. C. F. (1992a). Constitutive models for the sintering of ceramic components—I. Material models. *Acta Metallurgica et Materialia*, 40(8), 1969–1979.

Du, Z. Z. & Cocks, A. C. F. (1992b). Constitutive models for the sintering of ceramic components—II. Sintering of inhomogeneous bodies. *Acta Metallurgica et Materialia*, 40(8), 1981–1994.

Edmonds, M. & Herd, R. A. (2007). A volcanic degassing event at the explosive-effusive transition. *Geophysical Research Letters*, 34(21), L21310.

Evans, K. E. & Gibson, A. G. (1986). Prediction of the maximum packing fraction achievable in randomly oriented short-fibre composites. *Composites Science and Technology*, 25(2), 149–162.

Fluegel, A. (2007). Glass viscosity calculation based on a global statistical modelling approach. *European Journal of Glass Science and Technology*, 48(1), 13–30.

Frenkel, J. (1945). Viscous flow of crystalline bodies under the action of surface tension. *Journal of Physics*, 9(5), 385–391.

Fukuzono, T. (1985). A method to predict the time of slope failure caused by rainfall using the inverse number of velocity of surface displacement. *Journal of the Japanese Landslide Society*, 22(2), 8–13.

Griffith, A. A. (1921). The phenomena of rupture and flow in solids. *Philosophical Transactions of the Royal Society of London*, 221, 163–198.

Grunder, A. & Russell, J. K. (2005). Welding processes in volcanology: Insights from field, experimental, and modeling studies. *Journal of Volcanology and Geothermal Research*, 142(1), 1–9.

Heap, M. J., Lavallée, Y., Petrakova, L., Baud, P., Reuschlé, T., Varley, N. R., & Dingwell, D. B. (2014). Microstructural controls on the physical and mechanical properties of edifice-forming andesites at Volcán de Colima, Mexico. *Journal of Geophysical Research*, 119(4), 2925–2963.

Hess, K.-U., Cordonnier, B., Lavallée, Y., & Dingwell, D. B. (2007). High-load, high-temperature deformation apparatus for synthetic and natural silicate melts. *Review of Scientific Instruments*, 78(7), 75102–75104.

Hess, K.-U., Cordonnier, B., Lavallée, Y., & Dingwell, D. B. (2008). Viscous heating in rhyolite: An in situ experimental determination. *Earth and Planetary Science Letters*, 275(1–2), 121–126.

Hess, K.-U. & Dingwell, D. B. (1996). Viscosities of hydrous leucogranitic melts: A non-Arrhenian model. *American Mineralogist*, 81, 1297–1300.

Hirata, T. (1987). Omori's power law aftershock sequences of microfracturing in rock fracture experiment. *Journal of Geophysical Research*, 92(B7), 6215–6221.

Hirose, T. & Shimamoto, T. (2005). Growth of molten zone as a mechanism of slip weakening of simulated faults in gabbro during frictional melting. *Journal of Geophysical Research*, 110(B5), B05202.

Hsueh, C. H. (1985). Effects of heterogeneity shape on sintering induced stresses. *Scripta Metallurgica*, 19(8), 977–982.

Hsueh, C. H., Evans, A. G., Cannon, R. M., & Brook, R. J. (1986). Viscoelastic stresses and sintering damage in heterogeneous powder compacts. *Acta Metallurgica*, 34(5), 927–936.

Irwin, G. R. (1958). Fracture. In *Handbuch der Physik* (pp. 551–590). Berlin, Germany: Springer-Verlag.

Kass, R. E. & Raftery, A. E. (1995). Bayes factors. *Journal of the American Statistical Association*, 90(430), 773–795.

Kendrick, J. E., Lavallée, Y., Hess, K.-U., Heap, M. J., Gaunt, H. E., Meredith, P. G., & Dingwell, D. B. (2013). Tracking the permeable porous network during strain-dependent magmatic flow. *Journal of Volcanology and Geothermal Research*, 260, 117–126.

Kendrick, J. E., Lavallée, Y., Hirose, T., di Toro, G., Hornby, A. J., de Angelis, S., & Dingwell, D. B. (2014). Volcanic drumbeat seismicity caused by stick-slip motion and magmatic frictional melting. *Nature Geoscience*, 7, 438–442.

Kennedy, B. M., Jellinek, A. M., Russell, J. K., Nichols, A. R. L., & Vigouroux, N. (2010). Time-and temperature-dependent conduit wall porosity: A key control on degassing and explosivity at Tarawera volcano, New Zealand. *Earth and Planetary Science Letters*, 299(1-2), 126–137.

Kierfeld, J. & Vinokur, V. M. (2006). Slow crack propagation in heterogeneous materials. *Physical Review Letters*, 96(17), 175502.

Kilburn, C. R. J. (2003). Multiscale fracturing as a key to forecasting volcanic eruptions. *Journal of Volcanology and Geothermal Research*, 125(3-4), 271–289.

Kilburn, C. R. J. (2012). Precursory deformation and fracture before brittle rock failure and potential application to volcanic unrest. *Journal of Geophysical Research*, 117(B2), B02211.

Kilburn, C. R. J. & Petley, D. N. (2003). Forecasting giant, catastrophic slope collapse: Lessons from Vajont, Northern Italy. *Geomorphology*, 54(1), 21–32.

Kilburn, C. R. J. & Voight, B. (1998). Slow rock fracture as eruption precursor at Soufriere Hills. *Geophysical Research Letters*, 25(19), 3665–3668.

Kokelaar, P. & Königer, S. (2000). Marine emplacement of welded ignimbrite: The Ordovician Pitts Head Tuff, North Wales. *Journal of the Geological Society*, 157(3), 517–536.

Kolzenburg, S., Heap, M. J., Lavallée, Y., Russell, J. K., Meredith, P. G., & Dingwell, D. B. (2012). Strength and permeability recovery of tuffisite-bearing andesite. *Solid Earth*, 3(2), 191–198.

Kraxner, J., Liška, M., Klement, R., & Chromčíková, M. (2009). Surface tension of borosilicate melts with the composition close to the E-glass. *Ceramics–Silikáty*, 53(2), 141–143.

Kuhn, L. T. & McMeeking, R. M. (1992). Power-law creep of powder bonded by isolated contacts. *International Journal of Mechanical Sciences*, 34(7), 563–573.

Lavallée, Y., Benson, P. M., Heap, M. J., Hess, K.-U., Flaws, A., Schillinger, B., Meredith, P. G., & Dingwell, D. B. (2013). Reconstructing magma failure and the degassing network of dome-building eruptions. *Geology*, 41(4), 515–518.

Lavallée, Y., Hess, K.-U., Cordonnier, B., & Dingwell, D. B. (2007). Non-Newtonian rheological law for highly crystalline dome lavas. *Geology*, 35(9), 843.

Lavallée, Y., Hirose, T., Kendrick, J. E., de Angelis, S., Petrakova, L., Hornby, A. J., & Dingwell, D. B. (2014). A frictional law for volcanic ash gouge. *Earth and Planetary Science Letters*, 400, 177–183.

Lavallée, Y., Meredith, P. G., Dingwell, D. B., Hess, K.-U., Wassermann, J., Cordonnier, B., Gerik, A., & Kruhl, J. H. (2008). Seismogenic lavas and explosive eruption forecasting. *Nature*, 453(7194), 507–510.

Lavallée, Y., Varley, N. R., Alatorre-Ibargüengoitia, M. A., Hess, K.-U., Kueppers, U., Mueller, S., Richard, D., Scheu, B., Spieler, O., & Dingwell, D. B. (2012). Magmatic architecture of dome-building eruptions at Volcán de Colima, Mexico. *Bulletin of Volcanology*, 74(1), 249–260.

Lawn, B. R. (1993). *Fracture of brittle solids*. Cambridge, UK: Cambridge Univ. Press.

Lawn, B. R. & Wilshaw, R. (1975). Indentation fracture: Principles and applications. *Journal of Materials Science*, 10(6), 1049–1081.

Legros, F., Kelfoun, K., & Martí, J. (2000). The influence of conduit geometry on the dynamics of caldera-forming eruptions. *Earth and Planetary Science Letters*, 179(1), 53–61.

Lejeune, A.-M. & Richet, P. (1995). Rheology of crystal-bearing silicate melts: An experimental study at high viscosities. *Journal of Geophysical Research*, 100(B3), 4215–4229.

Lengliné, O., Marsan, D., Got, J.-L., Pinel, V., Ferrazzini, V., & Okubo, P. G. (2008). Seismicity and deformation induced by magma accumulation at three basaltic volcanoes. *Journal of Geophysical Research*, 113(B12), B12305.

Leonard, M. (2000). Comparison of manual and automatic onset time picking. *Bulletin of the Seismological Society of America*, 90(6), 1384–1390.

Lesti, C., Porreca, M., Giordano, G., Mattei, M., Cas, R. A. F., Wright, H. M. N., Folkes, C. B., & Viramonte, J. (2011). High-temperature emplacement of the Cerro Galán and Toconquis Group ignimbrites (Puna plateau, NW Argentina) determined by TRM analyses. *Bulletin of Volcanology*, 73(10), 1535–1565.

Lockner, D. A. (1993). The role of acoustic emission in the study of rock fracture. *International Journal of Rock Mechanics and Mining Sciences*, 30(7), 883–899.

Lockner, D. A. & Byerlee, J. (1977). Acoustic emission and creep in rock at high confining pressure and differential stress. *Bulletin of the Seismological Society of America*, 67(2), 247–258.

Mackenzie, J. K. & Shuttleworth, R. (1949). A phenomenological theory of sintering. *Proceedings of the Physical Society of London*, 62(12), 833–852.

Mader, H. M., Manga, M., & Koyaguchi, T. (2004). The role of laboratory experiments in volcanology. *Journal of Volcanology and Geothermal Research*, 129(1), 1–5.

Main, I. G. (1999). Applicability of time-to-failure analysis to accelerated strain before earthquakes and volcanic eruptions. *Geophysical Journal International*, 139(3), F1–F6.

Main, I. G. (2000). A damage mechanics model for power-law creep and earthquake aftershock and foreshock sequences. *Geophysical Journal International*, 142(1), 151–161.

Main, I. G., Meredith, P. G., & Jones, C. (1989). A reinterpretation of the precursory seismic b-value anomaly from fracture mechanics. *Geophysical Journal International*, 96(1), 131–138.

Manley, C. R. (1995). How voluminous rhyolite lavas mimic rheomorphic ignimbrites: Eruptive style, emplacement conditions, and formation of tuff-like textures. *Geology*, 23(4), 349–352.

Marzocchi, W. & Bebbington, M. S. (2012). Probabilistic eruption forecasting at short and long time scales. *Bulletin of Volcanology*, 74(8), 1777–1805.

Maugis, D. (1985). Subcritical crack growth, surface energy, fracture toughness, stick-slip and embrittlement. *Journal of Materials Science*, 20(9), 3041–3073.

Maxwell, J. C. (1866). On the dynamical theory of gases. *Philosophical Transactions of the Royal Society of London*, 157, 49–88.

McMeeking, R. M. & Kuhn, L. T. (1992). A diffusional creep law for powder compacts. *Acta Metallurgica et Materialia*, 40(5), 961–969.

Mignan, A. & Woessner, J. (2012). Estimating the magnitude of completeness for earthquake catalogs. *Community Online Resource for Statistical Seismicity Analysis*, (pp. 1–45).

Mogi, K. (1962). Study of elastic shocks caused by the fracture of heterogeneous materials and its relations to earthquake phenomena. *Bulletin of the Earthquake Research Institute*, 40, 125–173.

Nur, A., Mavko, G., Dvorkin, J., & Galmudi, D. (1998). Critical porosity: A key to relating physical properties to porosity in rocks. *The Leading Edge*, 17(3), 357–362.

Ogata, Y. (1983). Estimation of the parameters in the modified Omori formula for aftershock frequencies by the maximum likelihood procedure. *Journal of Physics of the Earth*, 31(2), 115–124.

Ojala, I. O., Ngwenya, B. T., Main, I. G., & Elphick, S. C. (2003). Correlation of microseismic and chemical properties of brittle deformation in Locharbriggs sandstone. *Journal of Geophysical Research*, 108(B5), 2268.

Oldroyd, J. G. (1953). The elastic and viscous properties of emulsions and suspensions. *Proceedings of the Royal Society of London*, 218(1132), 122–132.

Olevsky, E. (1998). Theory of sintering: From discrete to continuum. *Materials Science and Engineering*, 23(2), 41–100.

Paterson, M. S. & Wong, T. (2005). *Experimental rock deformation: The brittle field*. Berlin, Germany: Springer-Verlag.

Peterson, D. W. (1986). Volcanoes: tectonic setting and impact on society. In *Active Tectonics: Impacts on Society*. Washignton DC, USA: National Academy Press.

Petri, A., Paparo, G., Vespignani, A., Alippi, A., & Costantini, M. (1994). Experimental evidence for critical dynamics in microfracturing processes. *Physical Review Letters*, 73(25), 3423–3426.

Prado, M. O., Zanotto, E. D., & Müller, R. (2001). Model for sintering polydispersed glass particles. *Journal of Non-Crystalline Solids*, 279(2-3), 169–178.

Quane, S. L. & Russell, J. K. (2003). Rock strength as a metric of welding intensity in pyroclastic deposits. *European Journal of Mineralogy*, 15(5), 855–864.

Quane, S. L. & Russell, J. K. (2005). Welding: insights from high-temperature analogue experiments. *Journal of Volcanology and Geothermal Research*, 142(1-2), 67–87.

Quane, S. L. & Russell, J. K. (2006). Bulk and particle strain analysis in high-temperature deformation experiments. *Journal of Volcanology and Geothermal Research*, 154(1-2), 63–73.

Quane, S. L., Russell, J. K., & Friedlander, E. A. (2009). Time scales of compaction in volcanic systems. *Geology*, 37(5), 471–474.

Ragan, D. M. & Sheridan, M. F. (1972). Compaction of the bishop Tuff, California. *Geological Society of America Bulletin*, 83(1), 95–106.

Rahaman, M. N., de Jonghe, L. C., Scherer, G. W., & Brook, R. J. (1987). Creep and densification during sintering of glass powder compacts. *Journal of the American Ceramic Society*, 70(10), 766–774.

Rahaman, M. N., Jonghe, L. C., & Brook, R. J. (1986). Effect of shear stress on sintering. *Journal of the American Ceramic Society*, 69(1), 53–58.

Raj, R. (1987). Analysis of the sintering pressure. *Journal of the American Ceramic Society*, 70(9), C–210–C–211.

Ramos, O., Cortet, P. P., Ciliberto, S., & Vanel, L. (2013). Experimental study of the effect of disorder on subcritical crack growth dynamics. *Physical Review Letters*, 110(16), 165506.

Reiner, M. (1964). The Deborah number. *Physics Today*, 17(1), 62.

Riehle, J. R., Miller, T. F., & Paquereau-Lebti, P. (2010). Compaction profiles of ash-flow tuffs: Modeling versus reality. *Journal of Volcanology and Geothermal Research*, 195(2), 106–120.

Robert, G., Andrews, G. D. M., Ye, J., & Whittington, A. G. (2013). Rheological controls on the emplacement of extremely high-grade ignimbrites. *Geology*, 41(9), 1031–1034.

Robert, G., Russell, J., & Giordano, D. (2008a). Rheology of porous volcanic materials: High-temperature experimentation under controlled water pressure. *Chemical Geology*, 256(3-4), 216–230.

Robert, G., Russell, J. K., Giordano, D., & Romano, C. (2008b). High-temperature deformation of volcanic materials in the presence of water. *American Mineralogist*, 93(1), 74–80.

Russell, J. K. & Quane, S. L. (2005). Rheology of welding: Inversion of field constraints. *Journal of Volcanology and Geothermal Research*, 142(1-2), 173–191.

Sammis, C. G. & Ashby, M. F. (1986). The failure of brittle porous solids under compressive stress states. *Acta Metallurgica*, 34(3), 511–526.

Scherer, G. W. (1977). Sintering of Low-Density Glasses: I, Theory. *Journal of the American Ceramic Society*, 60(5-6), 236–239.

Scherer, G. W. (1979). Sintering inhomogeneous glasses: Application to optical waveguides. *Journal of Non-Crystalline Solids*, 34(2), 239–256.

Scherer, G. W. & Bachman, D. L. (1977). Sintering of Low-Density Glasses: II, Experimental Study. *Journal of the American Ceramic Society*, 60(5-6), 239–243.

Shaw, B. E. (1993). Generalized Omori law for aftershocks and foreshocks from a simple dynamics. *Geophysical Research Letters*, 20(10), 907–910.

Shcherbakov, R., Turcotte, D. L., & Rundle, J. B. (2004). A generalized Omori's law for earthquake aftershock decay. *Geophysical Research Letters*, 31(11), L11613.

Sheridan, M. F. & Wang, Y. (2005). Cooling and welding history of the Bishop Tuff in Adobe Valley and Chidago canyon, California. *Journal of Volcanology and Geothermal Research*, 142(1), 119–144.

Skorohod, V. V. (1972). *Rheological basis of the theory of sintering*. Kiev, Ukraine: Naukova Dumka.

Sleeman, R. & van Eck, T. (1999). Robust automatic P-phase picking: An on-line implementation in the analysis of broadband seismogram recordings. *Physics of the Earth and Planetary Interiors*, 113(1), 265–275.

Smith, R. & Kilburn, C. R. J. (2010). Forecasting eruptions after long repose intervals from accelerating rates of rock fracture: The June 1991 eruption of Mount Pinatubo, Philippines. *Journal of Volcanology and Geothermal Research*, 191(1-2), 129–136.

Smith, R., Sammonds, P. R., & Kilburn, C. R. J. (2009). Fracturing of volcanic systems: Experimental insights into pre-eruptive conditions. *Earth and Planetary Science Letters*, 280(1), 211–219.

Smith, R. L. (1960). Ash flows. *Geological Society of America Bulletin*, 71(6), 795–841.

Sneddon, I. N. (1946). The distribution of stress in the neighbourhood of a crack in an elastic solid. *Proceedings of the Royal Society of London*, 187(1009), 229–260.

Soriano, C., Zafrilla, S., Martí, J., Bryan, S., Cas, R. A. F., & Ablay, G. (2002). Welding and rheomorphism of phonolitic fallout deposits from the Las Cañadas caldera, Tenerife, Canary Islands. *Geological Society of America Bulletin*, 114(7), 883–895.

Sornette, D. (2002). Predictability of catastrophic events: Material rupture, earthquakes, turbulence, financial crashes, and human birth. *Proceedings of the National Academy of Sciences*, 99, 2522–2529.

Sparks, R. S. J., Tait, S. R., & Yanev, Y. (1999). Dense welding caused by volatile resorption. *Journal of the Geological Society*, 156(2), 217–225.

Spriggs, R. M. (1961). Expression for Effect of Porosity on Elastic Modulus of Polycrystalline Refractory Materials, Particularly Aluminum Oxide. *Journal of the American Ceramic Society*, 28(1), 1960–1961.

Stasiuk, M. V., Barclay, J., Carroll, M. R., Jaupart, C., Ratté, J. C., Sparks, R. S. J., & Tait, S. R. (1996). Degassing during magma ascent in the Mule Creek vent (USA). *Bulletin of Volcanology*, 58(2-3), 117–130.

Sulpizio, R. & Dellino, P. (2014). Pyroclastic density currents: State of the art and perspectives. *Journal of Volcanology and Geothermal Research*, 283, 36–65.

Suzuki, Y. J. & Koyaguchi, T. (2010). Numerical determination of the efficiency of entrainment in volcanic eruption columns. *Geophysical Research Letters*, 37(5), L05302.

Swinkels, F. B. & Ashby, M. F. (1981). A second report on sintering diagrams. *Acta Metallurgica*, 29(2), 259–281.

Swinkels, F. B., Wilkinson, D. S., Arzt, E., & Ashby, M. F. (1983). Mechanisms of hot-isostatic pressing. *Acta Metallurgica*, 31(11), 1829–1840.

Tokarev, P. I. (1971). Forecasting volcanic eruptions from seismic data. *Bulletin Volcanologique*, 35(1), 243–250.

Tuffen, H. & Dingwell, D. B. (2005). Fault textures in volcanic conduits: Evidence for seismic trigger mechanisms during silicic eruptions. *Bulletin of Volcanology*, 67(4), 370–387.

Tuffen, H., Dingwell, D. B., & Pinkerton, H. (2003). Repeated fracture and healing of silicic magma generate flow banding and earthquakes? *Geology*, 31(12), 1089–1092.

Tuffen, H., Smith, R., & Sammonds, P. R. (2008). Evidence for seismogenic fracture of silicic magma. *Nature*, 453(7194), 511–514.

Uhlmann, D. R., Klein, L., & Hopper, R. W. (1975). Sintering, crystallization, and breccia formation. *The Moon*, 13(1-3), 277–284.

Utsu, T., Ogata, Y., & Matsu'ura, R. S. (1995). The centenary of the Omori formula for a decay law of aftershock activity. *Journal of Physics of the Earth*, 43(1), 1–33.

Venkatachari, K. R. & Raj, R. (1986). Shear deformation and densification of powder compacts. *Journal of the American Ceramic Society*, 69(6), 499–506.

Voight, B. (1988). A method for prediction of volcanic eruptions. *Nature*, 332(6160), 125–130.

Voight, B. (1989). A relation to describe rate-dependent material failure. *Science*, 243(4888), 200–203.

Wadsworth, F. B., Vasseur, J., von Aulock, F. W., Hess, K.-U., Scheu, B., Lavallée, Y., & Dingwell, D. B. (2014). Nonisothermal viscous sintering of volcanic ash. *Journal of Geophysical Research*, 119(12), 8792–8804.

Wakai, F., Chihara, K., & Yoshida, M. (2007). Anisotropic shrinkage induced by particle rearrangement in sintering. *Acta Materialia*, 55(13), 4553–4566.

Webb, S. L. & Dingwell, D. B. (1990a). Non-Newtonian rheology of igneous melts at high stresses and strain rates: Experimental results for rhyolite, andesite, basalt, and nephelinite. *Journal of Geophysical Research*, 95(B10), 15695–15701.

Webb, S. L. & Dingwell, D. B. (1990b). The onset of non-Newtonian rheology of silicate melts. *Physics and Chemistry of Minerals*, 17(2), 125–132.

Whittington, A. G., Hellwig, B. M., Behrens, H., Joachim, B., Stechern, A., & Vetere, F. (2009). The viscosity of hydrous dacitic liquids: Implications for the rheology of evolving silicic magmas. *Bulletin of Volcanology*, 71(2), 185–199.

Wiederhorn, S. M. (1969). Fracture surface energy of glass. *Journal of the American Ceramic Society*, 52(2), 99–105.

Wiederhorn, S. M. & Bolz, L. H. (1970). Stress corrosion and static fatigue of glass. *Journal of the American Ceramic Society*, 53(10), 543–548.

Wilson, C. J. N. & Hildreth, W. (1997). The Bishop Tuff: New insights from eruptive stratigraphy. *The Journal of Geology*, 105(4), 407–440.

Wilson, C. J. N. & Hildreth, W. (2003). Assembling an ignimbrite: Mechanical and thermal building blocks in the Bishop tuff, California. *The Journal of Geology*, 111(6), 653–670.

Wong, T.-F. & Baud, P. (2012). The brittle-ductile transition in porous rock: A review. *Journal of Structural Geology*, 44, 25–53.

Zhang, H., Thurber, C., & Rowe, C. (2003). Automatic P-wave arrival detection and picking with multiscale wavelet analysis for single-component recordings. *Bulletin of the Seismological Society of America*, 93(5), 1904–1912.

Zhu, W., Baud, P., Vinciguerra, S., & Wong, T.-F. (2011). Micromechanics of brittle faulting and cataclastic flow in Alban Hills tuff. *Journal of Geophysical Research*, 116(B6), B06209.